Mahoney, J.J., Fitton, J.G., Wallace, P.J., et al., 2001
Proceedings of the Ocean Drilling Program, Initial Reports Volume 192

5. Site 1185[1]

Shipboard Scientific Party[2]

BACKGROUND AND OBJECTIVES

Site 1185 (Figs. F1, F2) is on the eastern edge of the main or high Ontong Java Plateau at the northern side of an enormous submarine canyon system (informally termed the Grand Canyon or Kroenke Canyon) that extends from Ontong Java Atoll and the Nukumanu Islands into the Nauru Basin. This part of the plateau is far from sites where basement crust was sampled previously, the closest of which are Ocean Drilling Program (ODP) Site 803 (334 km to the north-northwest) and Deep Sea Drilling Project (DSDP) Site 289 (351 km to the west). We chose this site for two principal reasons. First, the portion of basement volcanic stratigraphy within reach of the drill bit in this part of the plateau is likely to be different from that in more centrally located areas. In particular, only relatively few, far-traveled lava flows may have reached the edge of the plateau, possibly allowing us to sample a deeper level of the volcanic stratigraphy here than atop the plateau. Second, the 26 m of lava flows penetrated at ODP Site 803, the only other basement site on the eastern side of the high plateau, belong to the 90-Ma eruptive event (Mahoney et al., 1993); basement at other sites drilled on the high plateau (Sites 289, 807, 1183) formed ~122 Ma. We thought that 90-Ma basement might also be found at Site 1185, and drilling this site would then give us a clearer picture of the extent of this later event. Indeed, seismic reflection data (see immediately below) reveal intrabasement reflections in this part of the plateau, suggesting that a carapace of 90-Ma lavas might overlie 122-Ma basement rocks. If so, drilling at Site 1185 would provide further insight into the extent, composition, and mantle sources of the 90-Ma event documented previously at Site 803 and far to the south on the islands of Santa Isabel (Tejada et al., 1996; Parkinson et al., 1996) and San Cristobal (Birkhold-VanDyke et al., 1996).

F1. Predicted bathymetry of the Ontong Java Plateau showing site locations, p. 28.

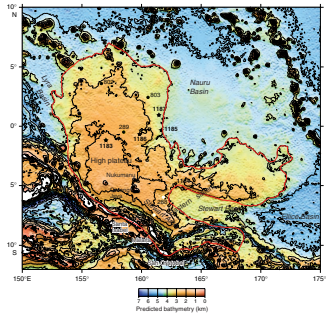

F2. Satellite-derived free-air gravity map of the Ontong Java Plateau region, p. 29.

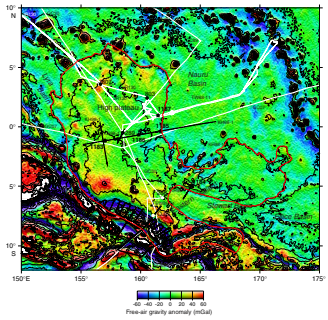

[1] **Examples of how to reference the whole or part of this volume.**
[2] **Shipboard Scientific Party addresses.**

Ms 192IR-105

Geophysical Background

Site 1185 is located at a water depth of ~3899 m (drill pipe measurement) on multichannel seismic reflection Line 401 of Leg 2, cruise KH98-1, of the *Hakuho Maru* (Figs. F3, F4, F5, F6, F7). The bathymetric transition between the plateau and the Nauru Basin lies ~35 km to the east-southeast. The site is midway between two seafloor scarps that may represent the heads of slumps or be related to erosion in the canyon system. The seafloor is rough in places, suggesting a high-energy depositional environment. The sediment section, interpreted to lie between the seafloor (at 5.2 s two-way traveltime [TWT]) and the top of a high-amplitude, moderately continuous reflection at 5.55 s TWT, is characterized by parallel to subparallel reflections of moderate to high continuity. Reflection amplitudes are low to high, and frequency is high. Unconformities and variations in reflection amplitude, continuity, and configuration within the sediment section indicate occasionally vigorous oceanographic and sedimentary conditions in the past. The top of acoustic basement is characterized by a high-amplitude, moderately continuous reflection. Several high-amplitude and relatively continuous intrabasement reflections also are apparent (e.g., at 5.9 s TWT beneath Site 1185; Figs. F6, F7). Preliminary results of a study of crustal structure as determined from Line 401 seismic and sonobuoy data have been presented by Mochizuki et al. (1998).

Summary of Objectives

The main objectives at this site were to determine

1. Compositions of basement rocks for comparison with those of lavas sampled in DSDP Site 289, ODP Sites 803 and 807, the other Leg 192 sites, and the islands of Santa Isabel, Malaita, and San Cristobal;
2. Age of basement rocks to establish whether basement in this region is 90 or 122 Ma;
3. Physical volcanology of basement rocks and the nature of sedimentary interbeds, in order to deduce the eruptive environment (flow types and approximate water depths);
4. Early subsidence history, as recorded in the basement rocks and the overlying sedimentary succession; and
5. Ages of sequence boundaries observed in the seismic record.

OPERATIONS

Transit to Site 1185

During operations at Site 1184, we continued to wait for clearance from the Solomon Islands to drill at proposed Site OJ-7D. Because we had not received clearance by the time operations were terminated, Site OJ-7D was abandoned from further consideration, and we proceeded to proposed Site OJ-11C to drill Site 1185. The 591-km transit to Site 1185 was accomplished in 28.8 hr at an average speed of 11.1 kt. The vessel proceeded directly to the Global Positioning System coordinates of the site, and at 1036 hr on 10 October 2000 we deployed a beacon.

F3. Site 1185 location and site-survey data, p. 30.

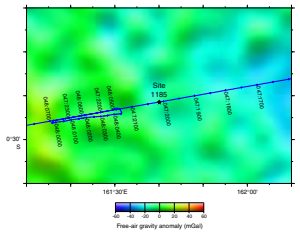

F4. MCS profile, p. 31.

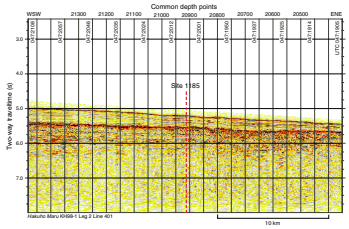

F5. MCS profile, p. 32.

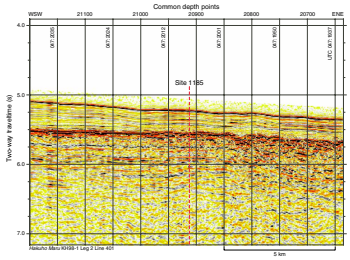

F6. MCS profile, p. 33.

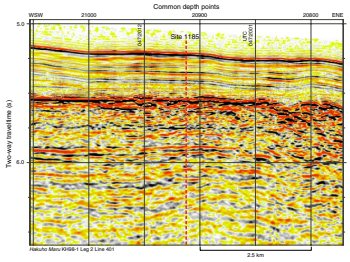

F7. MCS profile, p. 34.

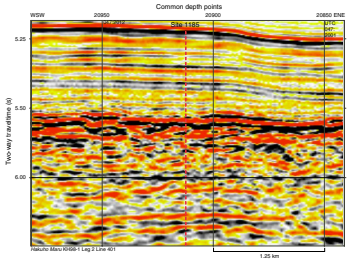

Hole 1185A

The plan at Site 1185 was to drill two holes. The first was to be a pilot hole drilled to basement and the second a reentry hole with a reentry cone and short section of 16-in casing. We spudded Hole 1185A with the rotary core barrel (RCB) at 2100 hr on 10 October and began a jet-in test. The purpose of the jet-in test was to determine the amount of 16-in casing to affix to the reentry cone on the second hole. The crew observed the bit tag the seafloor at a depth of 3898.9 meters below sea level with the vibration-isolated television (VIT) system. The jet-in test was concluded at 2300 hr after the bit had advanced 38 m. The results of the test indicated that a 30-m string of 16-in casing would be sufficient to anchor a reentry cone. Following the jet-in test, we drilled ahead with a wash barrel in place to a depth of 250.6 mbsf, where we initiated coring. The average rate of penetration through the washed interval was 53 m/hr.

We rotary cored the sediment portion of Hole 1185A from 250.6 to 308.5 mbsf (57.9 m interval) with an average recovery of 23.7%. Headspace gas analysis of the sediment cores yielded <2 ppm of methane and no heavier hydrocarbons. We contacted basement at 312.0 mbsf (based on driller's depth; 308.5 mbsf curated depth). Rotary coring continued into basement to a depth of 328.7 meters below seafloor (mbsf). The average recovery for basement was 66.9% (16.7 m), and average penetration rate was 2.3 m/hr. After determining the depth to basaltic basement, we realized the objective of the pilot hole, and we ceased coring in Hole 1185A. We retrieved the drill string, replaced the bit, and the vessel was offset 20 m west of Hole 1185A in preparation for the next hole.

Hole 1185B

The objective of Site 1185 was to penetrate at least 100 m into basaltic basement. Because of the difficulty of locating free-fall funnels that had sunk into the sediment at previous sites, we decided to set a reentry cone with 28 m of 16-in casing in Hole 1185B to ensure that we would be able to make multiple round trips of the drill string in order to change bits.

A reentry cone that was fabricated for Hole 1183A but unused was positioned in the moonpool and centered under the rotary table. After removing and securing the upper guide horn, the 16-in casing hanger was connected to the Dril-Quip cam-actuated-drill-ahead (CADA) tool and secured in the derrick. Two joints of 16-in casing and a shoe joint were then assembled and affixed to the casing hanger. Once the casing was assembled, a stand of 5.5-in drill pipe with the 16-in CADA tool was connected to the casing hanger. The hanger and casing assembly were then lowered through the rotary table just above the throat of the reentry cone. However, the throat of the reentry cone was too narrow and prevented the assembly from landing properly. After the welder increased the internal throat clearance, the hanger and casing were successfully latched into the reentry cone. The CADA running tool was then removed.

The crew assembled a jetting-in bottom-hole assembly (BHA) with a 14.75-in tricone drill bit and a stand of 8.25-in drill collars. This was followed by connecting the CADA tool to a stand of two 8.25-in drill collars and one tapered drill collar. We then lowered the BHA and CADA tool through the rotary table and connected them to the casing

hanger. We lowered the complete assembly to the seafloor and deployed the VIT during the pipe trip. We spudded Hole 1185B at 0930 hr on 13 October. Jetting in the 16-in casing required 2 hr. After successfully uncoupling the CADA tool from the casing hanger, we recovered the drill string and prepared a RCB BHA with a new C-7 bit.

The crew lowered the BHA to the seafloor and deployed the VIT. We positioned the bit over the reentry cone and reentered Hole 1185B at 0833 hr on 14 October after an 8-min search. We deployed the BHA to 31 mbsf and recovered the VIT. At 1000 hr, we began to drill ahead with a wash barrel in place and advanced to 308.0 mbsf. The wash barrel was retrieved and a new core barrel dropped. We began rotary coring at 1900 hr and contacted basaltic basement at 309.5 mbsf.

We continued coring in basement and advanced to a depth of 434.6 mbsf (125.1 m into basement) by the afternoon of 17 October. After we added a new stand of pipe and dropped a new core barrel, the bit nozzles clogged and the pump pressure reached a maximum of 3000 psi, indicating that all circulation was lost. The driller was able to work the drill string and partially clear some of the blockage. Because the bit had accumulated 52 rotating hr, we decided to conduct a round trip of the drill string to replace the bit. Average recovery in the cored basement section was 40.1%, at an average penetration rate of 2.7 m/hr.

After the drill string was recovered, inspection of the bit showed that it was evenly worn, had two plugged nozzles, and had a slightly undergauge body. The drilling jars could not be mechanically operated and were replaced. The crew affixed a new C-7 RCB bit to a mechanical bit release and deployed it. At 1330 hr on 18 October, we successfully reentered the hole after a brief search and resumed rotary coring at 1700 hr. Pump pressure was initially high (1500 psi at 75 strokes/min), indicating that a few of the bit nozzles were clogged. After advancing the bit several meters, the pressure gradually stabilized to a nominal value of 650 psi at 75 strokes/min. After heavy use of mud flushes to clean out the hole, we resumed rotary coring in basement. Coring advanced from 434.6 to 502.1 mbsf with an average rate of penetration of 1.7 m/hr and average recovery of 58.5%.

When Cores 192-1185B-25R and 26R were retrieved with no recovery, we deployed a bit deplugger twice in an attempt to clear a possible obstruction in the throat of the bit. We then cored a 1-m interval but had no recovery, so the deplugger was deployed a third time. After this, we dropped another core barrel, advanced 1 m, and recovered 0.98 m of basalt and a small segment of a bit seal O-ring. The latter suggested that the blockage of the bit was caused by partial disintegration of the bit seal. We dropped a new core barrel (Core 192-1185B-29R), but, after coring 7.6 m, the top-drive motor stalled at 600 A. The torque was slowly released, and the driller observed a loss of 500 psi standpipe pressure. The crew immediately turned off the active heave compensator, so they could use the Martin Decker weight indicator to determine downhole conditions. The driller noted a loss of ~40,000 lb of drill string weight, indicating a failure somewhere in the BHA.

The crew circulated a 50-bbl sepiolite sweep to ensure a clean hole for fishing operations and pumped a 20-bbl slug of heavy mud downhole. They set back the top drive and pulled the drill string out of the hole. After considering the time that would be required to attempt fishing of the BHA vs. the time that would be lost for scientific operations, we decided to abandon the site. Upon recovery of the BHA, we found that the outer body of the drilling jars had broken apart. We inspected the remaining components of the BHA above the jars but found no defects.

During operations at Hole 1185B, we cored 216.6 m of basaltic basement (Tables T1, T2) with 42% average recovery. At 0515 hr on 22 October 2000, the vessel began the transit to Site 1186.

T1. Coring summary, p. 105.

T2. Expanded coring summary, p. 106.

LITHOSTRATIGRAPHY

Overview

Site 1185 is located at a water depth of 3898.9 m at the eastern edge of the Ontong Java Plateau. Drilling was focused on the igneous basement, and only the lower ~60 m of the sedimentary column was cored (Fig. F8). Rocks in this interval are middle to upper Eocene nannofossil chalk with radiolarians to radiolarian nannofossil chalk with rare chert. The chalks are commonly bioturbated, and synsedimentary slump structures are present in the lower portion of the sedimentary succession. Rare limestone layers and fracture fillings are present in the igneous basement, which is composed of basalt flows.

F8. Lithostratigraphic summary, p. 35.

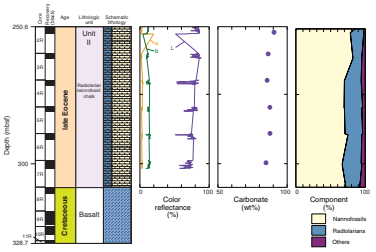

T3. Lithologic units, p. 110.

Unit Descriptions

Two holes were drilled at Site 1185. The sedimentary succession recovered is dominated by chalk and limestone with abundant siliceous microfossils. We recognize a single lithologic unit overlying basement (Table T3).

Although at Site 1185 we did not core the interval from the seafloor to 58 m above basement, we assume that the Tertiary sedimentary history was similar to the history at other sites on the Ontong Java Plateau. To maintain consistency with these other sites, we have designated the recovered interval of sediments as Unit II. The chalk recovered from Site 1185 contains abundant radiolarians and is middle to late Eocene in age. At Site 803, 334 km to the north-northwest, middle to late Eocene nannofossil chalk of Unit II is distinguished from nannofossil chalk of Unit I by its abundant siliceous microfossils. Eocene siliceous chalk is also characteristic of Unit II at DSDP Site 289 (Shipboard Scientific Party, 1975) and ODP Sites 807 (Kroenke, Berger, Janecek, et al., 1991) and 1183 (see "Lithostratigraphy," p. 4, in the "Site 1183" chapter). Unit II at Site 1185 sits on basalt. Rare interflow limestone beds and sediment-filled fissures are found within the underlying basaltic lava flows.

Unit II

Intervals: 192-1185A-2R-1, 0 cm, through 8R-1, 14 cm, and 192-1185B-2R-1, 0 cm, through 2R-1, 151 cm
Depth: 250.60–308.54 mbsf (Hole 1185A) and 308.00–309.51 mbsf (Hole 1185B)
Age: middle to late Eocene
Lithology: nannofossil chalk with radiolarians to radiolarian nannofossil chalk

The cored interval of Unit II in Hole 1185A is 58 m thick and contains middle to late Eocene microfossils (see "Biostratigraphy," p. 7). The top of the unit was not cored. The base of the unit is the top of basaltic basement (Section 192-1185A-8R-1, 14 cm; 308.54 mbsf; Section 1185B-2R-2, 0 cm; 309.51 mbsf). The sediment/basalt contact was not recovered.

Unit II consists dominantly of nannofossil chalk with radiolarians to radiolarian nannofossil chalk (Figs. F9, F10). Chert fragments are a minor lithology in Sections 192-1185A-6R-CC through 8R-1 (291.06–308.54 mbsf). The carbonate content ranges from 84.6 to 90.4 wt% (Table T4). The volume proportion of radiolarians estimated from observation of thin sections and smear slides shows a slight increase downhole and is 25%–30% in Cores 192-1185A-5R through 8R (Fig. F8). The chalk is white to very pale brown (10YR 8/2) to light gray (10YR 7/2) and darkens downhole. Bioturbation is common, although the poor recovery, drilling disturbance, and homogeneous nature of the sediments make characterization of the biogenic fabric difficult. Small (<1 mm) black particles (pyrite or Mn oxide) are scattered throughout. Some burrows are surrounded by black particles (Fig. F11). Physical sedimentary structures are rare. Slump folding is observed in the lowest portion of this unit (interval 192-1185A-7R-1, 130 cm, to 7R-CC, 50 cm) (Fig. F12). The upper 20 cm of the slumped material was burrowed after deformation, and the burrows are filled with material similar to the immediately overlying chalk (Fig. F12).

Sediment Interbeds in Basement

Intervals: 192-1185A-8R-1, 14 cm, through 11R-1, 92 cm, and 192-1185B-2R-2, 0 cm, to 28R-1, 104 cm
Depth: 308.54–328.7 mbsf (Hole 1185A); 309.51–526.1 mbsf (Hole 1185B)
Age: Cretaceous
Lithology: basalt flows with rare interbeds of limestone

The basement in both holes drilled at Site 1185 consists of basalt flows with rare, intercalated, thin limestone beds. Poorly preserved planktonic foraminifers and nannofossils of Cretaceous age are present in the limestone (see "Biostratigraphy," p. 7). The basalt is described in detail in "Igneous Petrology," p. 11, "Alteration," p. 15, and "Structural Geology," p. 17. The contact between chalk of Unit II and basalt basement was not recovered.

Limestone is present in the basalt sequence as rare interbeds, between pillows (Fig. F13), as the matrix of hyaloclastite breccia, and rarely in sediment-filled fissures (Fig. F14). The limestone is composed of micritic calcite with very poorly preserved foraminifers and radiolarians (Fig. F15). Brown semiopaque particles and recrystallized calcite veins are common. Sedimentary structures are difficult to distinguish.

Sedimentation History of Site 1185

Nannofossil chalk is typical of pelagic sediment on the Ontong Java Plateau. Planktonic foraminifers are very rare in the Eocene chalk of Site 1185, whereas calcareous nannofossils, benthic foraminifers, and calcified radiolarians are abundant. These observations suggest that Site 1185 was at or below the foraminifer lysocline but above the calcite compensation depth (CCD) during deposition of Unit II. No current-generated sedimentary structures were observed.

The folding in the lowest portion of Unit II (interval 192-1185A-7R-1, 130 cm, through 7R-CC, 50 cm) was syndepositional. The elongation of trace fossils within the slump block and the continuous folding imply that there was only a minor amount of soft-sediment deformation. There is no evidence of hardground formation or a major difference in

F9. Typical chalk facies, p. 36.

F10. Radiolarian nannofossil chalk, p. 37.

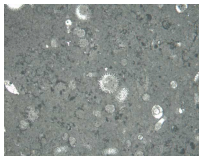

T4. Components in Unit II sediments, p. 111.

F11. *Planolites*-type burrows in whitish band, p. 38.

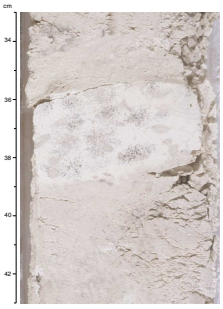

F12. Contorted bedding caused by slumping, p. 39.

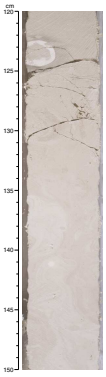

composition across the top of the slump. The uppermost 20 cm of the bed is burrowed, demonstrating that slumping was synsedimentary and that contemporary benthos reworked bottom sediments to at least 20 cm below the sediment/water interface.

Limestone in the underlying basalt is Cretaceous in age, but age resolution in Unit III is poor (see "Biostratigraphy," p. 7). The Paleocene–lower Eocene and probably much of the Upper Cretaceous are missing between the youngest limestone and the oldest chalk (see "Biostratigraphy," p. 7). The deposition of Unit II near the foraminifer lysocline and a comparison with the stratigraphy of shallower sites (see "Lithostratigraphy," p. 4, in the "Site 1183" chapter) suggests that the preservation of Eocene chalk began when the regional CCD sank below the depth of Site 1185.

BIOSTRATIGRAPHY

Overview

Middle to upper Eocene calcareous ooze and limestone are present immediately above basement at Site 1185. Extremely rare calcareous nannofossils recovered from limestone interbeds within the upper 15 m of basaltic basement in both holes indicate an Albian to Cenomanian age. Recrystallized planktonic foraminifers found within thermally metamorphosed limestone 126 m below the sediment/basement contact in Hole 1185B tentatively indicate a late Aptian age.

The calcareous microfossil biozonations used here are discussed in "Biostratigraphy," p. 10, in the "Explanatory Notes" chapter. A summary of the main biostratigraphic events identified in the sediments recovered from Site 1185 is presented in Table T5.

Hole 1185A

Fifty-eight meters of middle to upper Eocene calcareous ooze and limestone (Cores 192-1185A-2R to 8R) were cored from Hole 1185A. Planktonic foraminifers indicate a possible hiatus spanning the middle to upper Eocene boundary (encompassing Zone P15; Berggren et al., 1995) between Sections 192-1185A-5R-CC and 6R-CC. Calcareous nannofossils recovered from limestone interbeds in the uppermost basalts (Sections 192-1185A-9R-4 and 10R-1) indicate an Albian to early Turonian age but may be no older than late Albian.

Calcareous Nannofossils

Calcareous nannofossils are abundant and moderately to well preserved in Cores 192-1185A-2R through 7R; the few middle Eocene nannofossils recovered from the uppermost portion of Core 8R (5–14 cm) are poorly preserved. The presence of *Cribrocentrum reticulatum* and *Chiasmolithus solitus* in these samples from Core 8R, which are immediately above basement, indicate Zone NP16 of Martini (1971) and an age no older than 42 Ma (see Berggren et al., 1995). Above this level, the sedimentary sequence is well dated by a succession of nannofossil events (see Table T5), although the zonal markers for the bases of Zones NP18 and NP19 were not recognized in recovered assemblages. The presence of *Chiasmolithus consuetus* in the topmost sample examined (Sample 192-1185A-2R-1, 0–1 cm) indicates Zone NP19 (see Perch-

F13. Boundary between Unit 2 and Subunit 3A, p. 40.

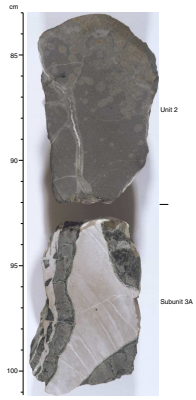

F14. Fine-grained limestone adjacent to fine-grained basalt, p. 41.

F15. Altered radiolarians or foraminifers in micritic calcite matrix, p. 42.

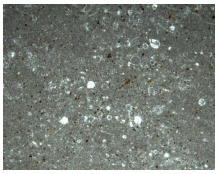

T5. Planktonic foraminifer and calcareous nannofossil occurrences, p. 112.

Nielsen, 1985) and that we did not recover rocks of terminal Eocene age.

Within basement, extremely rare and poorly preserved calcareous nannofossils were recovered from five samples taken from limestone interbeds in Sections 192-1185A-9R-4 and 10R-1. Section 9R-4, 17 cm, contains *Rhagodiscus asper,* which indicates an age no younger than early Turonian. *Tranolithus exiguus* (two specimens) and *Microstaurus chiastius* (one specimen) were recovered from Section 192-1185A-10R-1, 49 cm; their co-occurrence indicates an early Albian to latest Cenomanian age (see Table **T5**). A questionable specimen of *Eiffellithus turriseiffelii* observed in Section 192-1185A-9R-4, 17 cm, may indicate an age no older than late Albian for this sample.

Planktonic Foraminifers

Planktonic foraminifers are common and moderately well preserved in Cores 192-1185A-2R through 3R but are nearly absent in Cores 192-1185A-4R and 5R. They become common again in Cores 192-1185A-6R through 8R but indicate a dissolution-affected assemblage. Cores 192-1185A-2R and 3R contain large globigerinids and subbotinids with first stratigraphic appearances in late Eocene Zone P16 (Tourmakine and Luterbacher, 1985). The most common taxa include *Globigerina euapertura, G. venezuelana, G. pseudovenezuelana,* and *Subbotina gortanii*. The interval is restricted to the latest Eocene by the co-occurrence of *Tuborotalia cerroazulensis,* which has a last stratigraphic occurrence within Zone P17 (Berggren et al., 1995). The interval from Cores 192-1185A-4R through 5R is nearly barren of planktonic foraminifers, indicating deposition below the foraminifer lysocline. Only two corroded specimens of large, thick-walled species from the late Eocene assemblage were recovered (e.g., *G. euapertura*). Cores 192-1185A-6R to 8R, however, are marked by a moderate increase in planktonic foraminifer recovery, but the assemblage is strongly dominated by robust, very thick walled species of *Globigerinatheka,* especially *G. senni* and *G. subconglobata*. An assemblage affected by dissolution is indicated, with deposition near the foraminifer lysocline but under less corrosive conditions than indicated by the interval represented by Cores 192-1185A-4R and 5R. With a middle Eocene last stratigraphic occurrence (Zone P14; Tourmarkine and Luterbacher, 1985), *G. senni* indicates a stratigraphic hiatus spanning the middle to upper Eocene boundary (Table **T5**). However, given that the planktonic assemblage is depleted because of dissolution, the duration of the hiatus cannot be defined precisely. In Cores 192-1185A-7R and 8R, the co-occurrence of *Tuborotalia cerroazulensis* and *Globigerinatheka index,* species with middle Eocene first stratigraphic appearances, and *Globigerinatheka micra,* with a middle Eocene last stratigraphic occurrence, indicates Zone P12 (Toumarkine and Luterbacher, 1985). In addition, the first appearance of *G. index* has been calibrated by Berggren et al. (1995) at 42.9 Ma (Table **T5**).

Thin section study of limestone recovered from the upper basalt section (Core 192-1185A-10R) reveals common radiolarians and rare, very small (<80 µm) planktonic foraminifers. Preservation is very poor: the radiolarians are calcified to coarsely crystalline spar, and the foraminifers are recrystallized. The limestone is baked by basalt and shows concentric zones of lessening thermal alteration away from the limestone/basalt contact. From their gross morphology, the planktonic foraminifers appear to be species of either the genus *Hedbergella*

or *Blefuscuiana*. Very similar biofacies composed of large radiolarians and small planktonic foraminifers are present in two discrete intervals from Hole 1183A: the upper Albian limestone (Samples 192-1183A-51R-3, 13–15 cm, to 52R-1, 139–141 cm) and the middle Aptian limestone immediately overlying basaltic basement (Samples 192-1183A-54R-3, 59–61 cm, to 54R-3, 96–99 cm). However, poor preservation prevents any definite biostratigraphic determination from Hole 1185A.

Paleoenvironment

Benthic foraminifers are common and well preserved in all samples examined from the Eocene section of Hole 1185A (Cores 192-1185A-2R to 8R) but are absent from limestone interbeds of Core 10R. The benthic foraminifers, including most of the agglutinated taxa present, are composed almost entirely of calcareous specimens. However, two upper Eocene samples (Samples 192-1185A-3R-CC, 13–15 cm, and 6R-1, 51–53 cm) contain rare, noncalcareous agglutinated species composed of silt-size, yellow quartz grains with rare black (heavy?) mineral grains and very rare volcanic glass shards. Some agglutinated species are restricted to these samples (e.g., *Rhabdammina abyssorum* and *Hormosinella ovicula*), whereas other taxa, noncalcareous in these samples, are also present in other parts of the upper Eocene section, where they are composed of nannofossil ooze, a consequence of a lack of volcaniclastic grains (e.g., *Adercotryma glomeratum*). These agglutinated species are useful in marking the presence of very rare volcaniclastic material that otherwise might escape detection in macroscopic core or sedimentologic analysis.

The Eocene assemblage shows a relatively high species diversity and indicates a uniform, deep abyssal paleobathymetry >3000 m (Table T6) (van Morkhoven et al., 1986). However, there is a distinct faunal turnover between the middle and upper Eocene assemblages, first described from the abyssal Eocene of the Atlantic Ocean (Tjalsma and Lohmann, 1983). The abyssal benthic foraminifer assemblage of the early Eocene, dominated by *Nuttallides truempyi* and associated taxa, is gradually replaced in the middle Eocene by an assemblage that dominates upper Eocene and Oligocene abyssal facies. Below the upper Eocene, *N. truempyi* is a dominant component of abyssal and bathyal benthic foraminifer assemblages but in the upper Eocene is restricted to abyssal paleodepths before becoming extinct near the end of the Eocene (Tjalsma and Lohmann, 1983). Although termed the "late Eocene" assemblage, this group of benthic foraminifer species is actually well established in middle Eocene limestone from Hole 1185A (Table T6). The assemblage is composed of *Oridosalis umbonatus, Stilostomella* species, *Cibicidoides praemundulus* (= *C. ungerianus* of Tjalsma and Lohmann, 1983), and planoconvex taxa of *Cibicidoides* such as *C. grimsdalei* and *C. eocaenus*. The turnover in Hole 1185A is illustrated in Table T6. Components of the "late Eocene" benthic assemblage are already well established by the middle Eocene, but the overall assemblage is still dominated by *Nuttallides truempyi* and associated species. The lowest stratigraphic level marked by a decline in *N. truempyi* occurs immediately above the middle to upper Eocene unconformity between Samples 192-1185A-6R-1, 108–110 cm, and 6R-2, 6–8 cm. The lower portion of the upper Eocene section (Samples 192-1185A-4R-CC, 17–19 cm, to 6R-1, 6–8 cm) marks a transitional interval in which components of both assemblages are rare. However, by the time of deposition of the overlying upper Eocene section in Cores 192-1185A-2R and 3R, the "late Eocene" abys-

T6. Turnover in abyssal benthic foraminifer assemblages, p. 113.

sal assemblage is firmly established and components of the *Nuttalides truemypi* assemblage are rare, including the nominate taxon. The cause of this benthic foraminifer turnover has not been generally determined but, in Hole 1185A, is clearly associated with a rise in the foraminifer lysocline and, hence, presumably the CCD as well. The middle to upper Eocene hiatus may indicate a rise in the CCD above Site 1185, and the overlying transition zone in the lower part of the upper Eocene (Samples 192-1185A-4R-CC, 17–19 cm, to 6R-1, 6–8 cm) was deposited below the foraminifer lysocline. By the time deposition resumed above the lysocline (Cores 192-1185A-2R through 3R), the turnover in abyssal benthic foraminifer assemblages was complete.

Hole 1185B

One full core section (Section 192-1185B-2R-1) of middle Eocene limestone was recovered above basalt basement (encountered in Section 2R-2) from Hole 1185B; this section is correlative with the basal limestone interval from Hole 1185A (Core 8R). Calcareous nannofossils recovered from limestone interbeds in the uppermost basalts (Core 192-1185B-4R) indicate an age of Albian to Cenomanian but may be late Albian. Recrystallized planktonic foraminifers recovered from thermally metamorphosed limestone much deeper in the basalt sequence (Core 192-1185B-17R) tentatively indicate a late Aptian age.

Calcareous Nannofossils

Middle Eocene nannofossil assemblages recovered from six samples taken in Section 192-1185B-2R-1 are all poorly preserved and have a low to moderate abundance. The presence of *Cribrocentrum reticulatum* and *Chiasmolithus solitus* in these samples immediately above basement indicates Zone NP16 of Martini (1971) and an age no older than 42 Ma (see Berggren et al., 1995).

Within basement, extremely rare and poorly preserved calcareous nannofossils were recovered from five samples taken in limestone interbeds in Sections 192-1185B-4R-2 through 6R-1. Section 192-1185B-4R-2, 42 cm, contains *Microstaurus chiastius,* which indicates an age no younger than the end of the Cenomanian; the presence of *Prediscosphaera columnata* (one specimen) in the subjacent Section 192-1185B-4R-3, 58 cm, indicates an age no older than earliest Albian (see Table **T5**). A questionable specimen of *Eiffellithus monechiae* found in Section 192-1185B-4R-4, 43 cm, may indicate a late Albian age for this sample. The ages of calcareous nannofossils recovered from two samples in Section 192-1185B-6R-1 are indeterminate.

Planktonic Foraminifers

The middle Eocene section in Hole 1185B, as in Hole 1185A, was deposited below the foraminifer lysocline. Sample 192-1185B-2R-1, 35–37 cm, is nearly barren of planktonic species, containing only two poorly preserved specimens of the dissolution-resistant middle Eocene species, *Globigerinatheka senni*. Sample 192-1185B-2R-1, 146–148 cm, contains more common and diverse planktonic foraminifers and common volcaniclastic grains and displays wispy laminae and diffuse grading of bioclasts. The sample represents an allochthonous deposit, transitional between a mudflow and turbidite, in which rapid burial of planktonic species transported from above the lysocline prevented

extensive dissolution. The co-occurrence of the planktonic foraminifer species *Globigerinatheka micra* and *Tuborotalia cerroazulensis* in this sample indicates an upper P12 zonal assignment, as in Core 8R from Hole 1185A.

Thin section examination of limestone interbeds in the basalt of Core 192-1185B-4R reveals a recrystallized carbonate with common radiolarians and very small planktonic foraminifers (<60 µm), a biofacies very similar to that noted from Core 192-1185A-10R. However, preservation is slightly better in Core 192-1185B-4R, allowing identification of one species, *Guembelitriella graysonensis*. A long-ranging species, *G. graysonensis,* has been documented previously from the upper Aptian to lower Cenomanian (Leckie, 1984). The only other limestone in the basalt section to contain foraminifers was sampled in Sample 192-1185B-17R-1, 80–82 cm. It is thermally altered limestone composed of spar and iron oxides. Common, recrystallized planktonic foraminifers varying widely in size are evident; radiolarians are very rare, indicating a biofacies quite different from that of the limestones in the upper basalt section from Holes 1185A and 1185B (Cores 192-1185A-10R and 192-1185B-4R). A large species of *Globigerinelloides* is present, which closely resembles the upper Aptian index *G. ferreolensis* (i.e., it is suboval in spiral view, with eight to nine chambers in the final whorl, increasing in size at a moderate rate). The poor preservation, however, prevents a definite identification.

Paleoenvironment

The benthic foraminifer assemblage of the Eocene limestone in Core 192-1185B-2R is very similar to the deep abyssal assemblage recovered from limestone immediately overlying the basalt in Core 192-1185A-8R. The assemblage is diverse and dominated by *Nuttallides truempyi, Cibicidoides grimsdalei,* and *Alabamina dissonata*. No benthic foraminifers are present in the limestone interbeds analyzed in Cores 192-1185B-4R and 17R.

IGNEOUS PETROLOGY

Introduction

We reached basaltic basement in Holes 1185A and 1185B at 308.5 and 309.5 mbsf, respectively. The age of the radiolarian nannofossil chalk directly above basement is middle Eocene, but fragments of limestone interbeds recovered within the basement section gave a tentative age of latest Cenomanian to Albian for the upper 15 m of basalt and possibly Aptian for interbeds 126 m below the top of basement in Hole 1185B (see **"Biostratigraphy,"** p. 7). We cored 16.7 m of basaltic basement in Hole 1185A (Cores 192-1185A-8R through 11R; 67% recovery) and divided it into five units. The units range in thickness from 0.2 to 9.9 m (Table **T7;** Fig. **F16**) and consist of pillow lava sequences separated by limestone and hyaloclastite interbeds (Fig. **F17**). In Hole 1185B, we cored 216.6 m of basaltic basement (Cores 192-1185B-2R through 28R had 42% recovery; Core 29R had 0% recovery) and divided it into twelve units ranging in thickness from 1 to 65.2 m (Table **T7;** Fig. **F16**). Units 1, 3, 4, and 6–9 are composed of pillow lava (Figs. **F17, F18**), whereas Units 2, 5, and 10–12 are massive lava flows (Fig. **F14**) with minor pillow lavas at their tops and/or bases. We defined

T7. Unit boundary thicknesses and characteristics, p. 114.

F16. Basement cores, recovery, rock types, and units, p. 43.

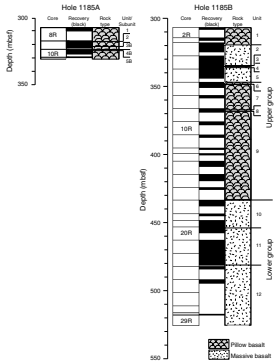

F17. Curved glassy rim of pillow basalt with spherulites in pillow interior, p. 44.

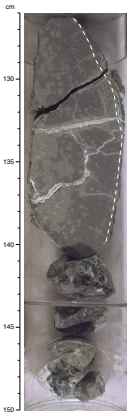

F18. Transition from massive basalt (Unit 2) to pillowed top of Unit 3, p. 45.

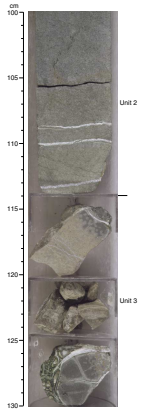

these units using a combination of criteria (Table T7), including the presence of limestone, breccia or hyaloclastite interbeds, changes in degree and type of alteration, downward changes from massive to pillowed flow type, and, in one instance, a marked change in drilling rate (see "Igneous Petrology," p. 12, in the "Explanatory Notes" chapter). In Section 192-1185B-22R-7, we recovered the only intact contact between two units, represented by the chilled base of Unit 11 in direct contact with the fine-grained blocky top of Unit 12 (Fig. F19).

Macroscopic Description

Holes 1185A and 1185B are only 20 m apart, and the petrologic characteristics of basalts from Hole 1185A are similar to those of the pillowed units at the top of the basement section in Hole 1185B. Thus, we present a single description for all the Site 1185 basement rocks.

The pillows generally have glassy margins typical of submarine lava flows (e.g., Kirkpatrick, 1978). Inside the glassy margins are aphanitic zones containing spherulites (Figs. F17, F20), some apparently nucleated on olivine phenocrysts. Some of the isolated spherulites are highlighted by alteration to smectite and Fe oxyhydroxide, giving them an orange-brown color (Figs. F21, F22; see "Alteration," p. 15). Pillow interiors are fine grained with variolitic texture imparted by elongate, radiating plagioclase laths with interstitial clinopyroxene and titanomagnetite. Recovery of pillowed units (Fig. F16) was generally poor (average = 10%), in contrast to the high (average = 74%) recovery of massive units (Sections 192-1185B-4R-1 through 5R-6; Cores 192-1185B-6R and 192-1185A-17R through 22R).

We observed systematic grain-size variations from the margins to the interiors of the massive units. The interiors of the massive flows (Fig. F23) are generally coarser grained than the interiors of the pillowed units. The massive flows typically contain alternating aphanitic and fine-grained layers. This grain-size banding is particularly well developed in the lower part of Unit 11 in Section 192-1185B-22R-1 (~473.2 mbsf), where several subparallel centimeter-wide bands alternating from very fine grained to aphanitic are present in the normally fine grained variolitic interior. The aphanitic layers become wider (tens of centimeters) downcore and have subhorizontal, diffuse contacts with the fine-grained layers (Section 192-1185B-22R-5). Section 192-1185B-22R-6 is dominated by aphanitic layers, which additionally contain rare subround, elongate or irregular patches of more coarsely crystalline material as much as a few centimeters in size (Fig. F24). We interpret the grain-size banding as a product of repeated inflation of the Unit 11 lava flow, with the aphanitic layers representing more rapidly crystallized regions of the flow. The more coarsely crystalline patches within the aphanitic layers may represent earlier, more slowly cooled, nearly crystallized parts of the same flow.

One characteristic feature of samples from Hole 1185A and from Units 1–9 of Hole 1185B is their relatively high (as much as 10%; e.g., Section 192-1185B-3R-1) olivine phenocryst content (Fig. F25). This petrologic feature is accompanied by a high MgO content (9–10 wt%; see "Geochemistry," p. 14). The olivine is generally replaced by green or black clay, Fe oxyhydroxide, or calcite, except for a few places where it is unaltered (e.g., Sample 192-1185A-8R-1, 15–18 cm). Olivine is the only phenocryst phase in the glassy rims and aphanitic margins and commonly forms glomerocrysts. The olivine phenocrysts are generally euhedral and equant, although some have elongate extensions. Most of

F19. Unit 11 in contact with Unit 12, p. 46.

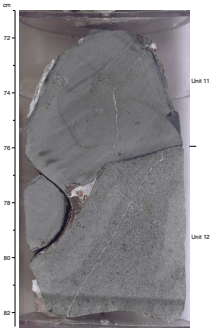

F20. Spherulites in aphanitic basalt, p. 47.

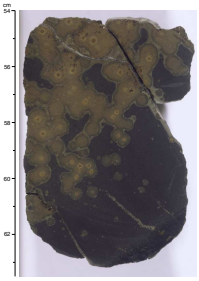

F21. Pervasively altered spherulitic basalt near pillow margin, p. 48.

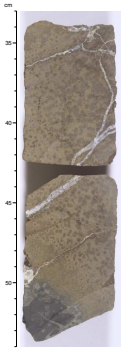

F22. Boundary between Units 3 and 4, p. 49.

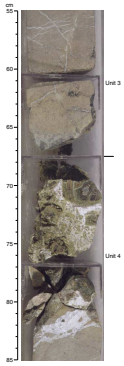

the euhedral to subhedral, equant olivine crystals in the fine-grained interiors of pillows and massive flows are approximately the same size as the groundmass plagioclase and clinopyroxene crystals. This characteristic made determination of olivine phenocryst content in the fine-grained interiors difficult in hand specimen.

Units 10–12 have a generally lower abundance of olivine phenocrysts than do Units 1–9. Plagioclase-rich xenoliths and solitary plagioclase xenocrysts (Fig. F25), similar to those observed from Hole 1183A (see "Igneous Petrology," p. 25, in the "Site 1183" chapter), are present in Units 10–12 of Hole 1185B. The xenoliths are generally small (<6 mm), irregular to subround and equant, and contain colorless, translucent plagioclase. Rare, small (<2 mm), angular and equant miarolitic cavities are present throughout Unit 9; some are interconnected. Miarolitic cavities are also present but rare in Units 10–12 (also see "Alteration," p. 15).

Petrography

Thin section examination confirmed our macroscopic observation that a traverse from pillow margin to flow interior shows the following sequence of textures: glassy pillow rim (e.g., Fig. F26); partly glassy to cryptocrystalline and dendritic margin near the glassy rim; and fine-grained, holocrystalline interior (e.g., Fig. F27). The degree of alteration depends highly on proximity to veins but is generally slight to moderate (see "Alteration," p. 15). All the basalts are essentially nonvesicular. For complete thin section descriptions, see the "Core Descriptions" contents list.

The basalts are generally sparsely to moderately olivine phyric or sparsely to moderately olivine-plagioclase phyric with clinopyroxene as a minor phenocryst phase. The basement sequence can be divided broadly into upper and lower groups on the basis of different olivine phenocryst abundances (2%–7% and 1%–3%, respectively), combined with the appearance in Units 10–12 of plagioclase and rare clinopyroxene phenocrysts and plagioclase-rich xenoliths (Fig. F25). The upper group consists of all the units in Hole 1185A and Units 1–9 in Hole 1185B, whereas the lower group consists of Units 10–12 in Hole 1185B (Fig. F16). The patches of more coarsely crystalline basalt in the fine-grained portions of Units 10–12 in Hole 1185B consist of olivine, plagioclase, clinopyroxene, and titanomagnetite. Some of the clinopyroxene and plagioclase phenocrysts in the finer grained portions of Units 10–12 may have been disaggregated from the more coarsely crystalline patches or may be xenocrysts similar to those found at Site 1183 (see "Igneous Petrology," p. 25, in the "Site 1183" chapter). Some of the plagioclase phenocrysts exhibit oscillatory zonation (Fig. F28).

Olivine phenocrysts (0.1–0.6 mm) are euhedral to subhedral in basalts from both holes. Olivine phenocrysts in the pillow margins are generally unaltered (Fig. F29), whereas those in the fine-grained interiors of pillows and massive flows are usually replaced completely by smectite, celadonite, and calcite (Fig. F30; see "Alteration," p. 15). However, a few olivine phenocrysts in fine-grained areas are unaltered (Fig. F31). Unaltered olivine phenocrysts contain rare, minute (<0.01 mm) glass inclusions. Chrome spinel (<0.01–0.02 mm) is commonly present in the upper group of lava flows but is rare to absent in the lower group. It is euhedral to subhedral and is usually present either as inclusions in olivine phenocrysts (Fig. F32) or as discrete crystals (Figs. F33, F34).

F23. Typical fine-grained basalt texture, p. 50.

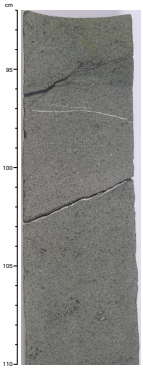

F24. Coarser grained patch in aphanitic basalt, p. 51.

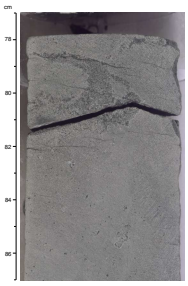

F25. Phenocrysts, fresh glass, and xenoliths, p. 52.

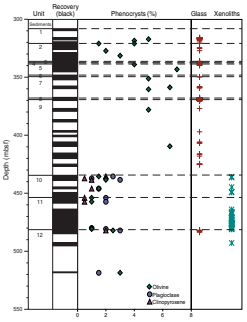

F26. Elongate vesicle trains and pillow-rim glass with phenocrysts, p. 53.

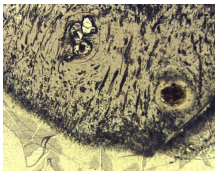

Plagioclase phenocrysts (0.1–0.6 mm wide) in the lower basalt group of Hole 1185B are typically subhedral to euhedral and tabular (Figs. F28, F30, F35). Clinopyroxene phenocrysts (0.15–0.2 mm) are anhedral to euhedral (Figs. F30, F35); some exhibit simple twinning and oscillatory and sector zoning. In Unit 12, clinopyroxene can form radiating needles, elongate crystals, and phenocrysts, all in the same sample (Fig. F30). Equant clinopyroxene phenocrysts are commonly observed in the cryptocrystalline to microcrystalline groundmass of Units 10–12. More coarsely crystalline patches are also present in these units, suggesting that the clinopyroxene crystals could simply be remnants of disaggregated patches (e.g., Samples 192-1185B-17R-1 [Piece 4E, 80–82 cm] and 22R-7 [Piece 2, 42–43 cm]).

We examined thin sections of two unaltered, glassy pillow rinds from Holes 1185A and 1185B, respectively. These rinds contain small olivine phenocrysts and elongate vesicles (Figs. F26, F36). Adjacent to the glassy rinds are aphanitic zones containing spherulites. The spherulites consist of skeletal to euhedral olivine surrounded by radiating clusters of acicular plagioclase and elongate olivine crystals (Fig. F37). Both dendritic olivine and small, euhedral olivine crystals with elongate extensions parallel to the *c* crystallographic axis (Fig. F38) are present in the groundmass.

The groundmass of pillow interiors exhibits variolitic, intergranular, and subophitic textures (Figs. F30, F31). The groundmass consists of plagioclase and clinopyroxene, with minor titanomagnetite, chrome spinel, and sulfide. Titanomagnetite (0.01–0.1 mm) can be euhedral to subhedral but is mainly skeletal (Fig. F39); it can be unaltered or partly to completely replaced by maghemite. Chrome spinel (<0.01–0.02 mm) is commonly mantled by titanomagnetite if the olivine host crystal is altered (Fig. F40). Sulfide (<0.01 mm) is present as subround to elongate blebs in the groundmass and as inclusions in the silicate minerals.

Units 10–12 contain more coarsely crystalline patches with intergranular, subophitic, or variolitic textures (Fig. F41). The size of the more coarsely crystalline patches is typically a few millimeters, but some are as large as 3 cm across (e.g., Sample 192-1185B-22R-6 [Piece 6A, 51–54 cm]; Fig. F42). As mentioned above, we interpret these patches as portions of slowly cooled crystal mush that were entrained in a later and more rapidly cooled pulse of magma within the same flow unit.

Geochemistry

We analyzed 16 basalt samples by inductively coupled plasma–atomic emission spectrometry (ICP-AES) to determine whole-rock composition. All are tholeiites (Fig. F43; Table T8). In terms of their silica and alkali contents, the Site 1185 basalts are indistinguishable from those at all previous DSDP and ODP sites, as well as the other Leg 192 sites. However, all samples from Hole 1185A and Units 1–9 of Hole 1185B are olivine normative, whereas those from Units 10–12 of Hole 1185B are generally quartz normative (Table T8). All data for Hole 1185A basalts plot with the data for Units 1–9 of Hole 1185B in elemental variation diagrams. Incompatible minor and trace element data confirm the distinction between the upper and lower groups of basalts at Site 1185 (Fig. F44). All samples from Hole 1185A and Units 1–9 of Hole 1185B have lower TiO_2, Zr, Sc, Y, V, and Sr abundances than do Units 10–12 of Hole 1185B. The lower units of Hole 1185B are compositionally similar to basalts from Sites 1183, 1186, and 807 (Units C–

F27. Texture typical of pillow interiors, p. 54.

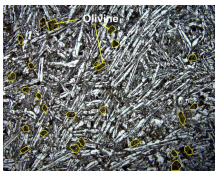

F28. Plagioclase phenocryst with oscillatory zonation, p. 55.

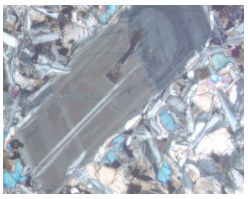

F29. Olivine phenocrysts, p. 56.

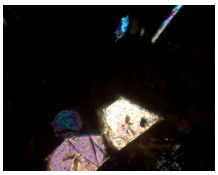

F30. Olivine, plagioclase, and clinopyroxene phenocrysts, p. 57.

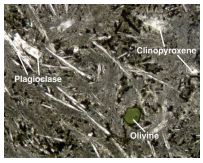

F31. Unaltered interiors of olivine phenocrysts, p. 58.

F32. Olivine phenocrysts and chrome spinel crystals, p. 59.

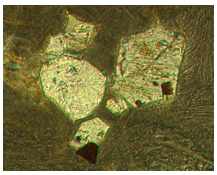

G), and the Kwaimbaita Formation on Malaita. The presence of chrome spinel in Units 1–9 is consistent with the elevated Cr contents (Fig. F45); in addition, these basalts have relatively high Ni and MgO contents (Table T8). The variation in Mg# within each of the two groups of basalts at Site 1185 is not accompanied by a corresponding variation in TiO_2; each group has a restricted range in TiO_2 content (Fig. F46). The range in Mg#, however, may have been exaggerated by mobility of MgO during alteration. Thus, the downhole chemical variation at Site 1185 shows that a more primitive basalt sequence (all units of Hole 1185A and Units 1–9 of Hole 1185B) overlies a more evolved series of flows (Units 10–12 of Hole 1185B; Fig. F47).

Comparison to Other Ontong Java Plateau Basalts

Units 10–12 in Hole 1185B are petrographically and geochemically similar to the basalt sequences recovered from Sites 1183, 1186, and 807 (Units C–G) but are mainly massive rather than pillowed flows. Basalts from Site 803 and Units C–G at Site 807 were described as fine grained and sparsely phyric with plagioclase, clinopyroxene, and olivine phenocrysts (Kroenke, Berger, Janecek, et al., 1991); the basalts from Site 1183 are mostly sparsely olivine (± plagioclase) phyric (see "Igneous Petrology," p. 25, in the "Site 1183" chapter). In Units 10–12 of Hole 1185B, olivine and plagioclase are the dominant phenocryst phases. Basalts from Sites 1183 and 1186 and Units 10–12 in Hole 1185B contain plagioclase-rich xenoliths. Such xenoliths are also present in basalts of the Kwaimbaita Formation on the island of Malaita, Solomon Islands, and in Units C–G at Site 807. Tejada et al. (in press) noted the geochemical similarities between basalts from Units C–G at Site 807 and the Kwaimbaita Formation on Malaita. Shipboard ICP-AES analyses show that Units 10–12 from Hole 1185B are compositionally similar to basalts from Sites 1183 and 1186 and to those of the Kwaimbaita Formation. Basalt from Hole 1185A and Units 1–9 of Hole 1185B is petrographically and geochemically similar to that from Site 1187.

In summary, basalt flows in all units of Hole 1185A and in Units 1–9 of Hole 1185B have the lowest concentrations of incompatible elements yet measured in basalts from the Ontong Java Plateau. They are also the most primitive (Mg-, Ni-, and Cr-rich and with high Mg#) basalts so far recovered from the plateau. These primitive basalt units overlie an older sequence of more evolved basalts that closely resembles those of the Kwaimbaita Formation on Malaita.

ALTERATION

Introduction

The entire sequence of basaltic basement cored from Site 1185 has undergone pervasive low-temperature interactions with seawater-derived fluids. We divide the basement section into two superposed zones that display the effects of low-temperature submarine alteration under different conditions and correspond to a difference in primary permeability of the basalt. The upper alteration zone consists of all units in Hole 1185A and Units 1–9 of Hole 1185B, all of which are dominated by pillow-lava flows. The lower alteration zone comprises Units 10–12 of Hole 1185B, which are massive lava flows.

F33. Euhedral chrome spinel crystal in groundmass of dendritic crystals and devitrified glass, p. 60.

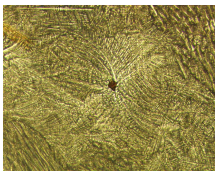

F34. Euhedral chrome spinel crystal in dendritic groundmass, p. 61.

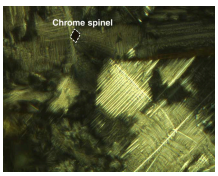

F35. Plagioclase and clinopyroxene phenocrysts, p. 62.

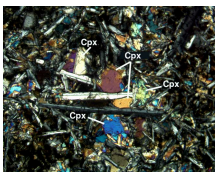

F36. Olivine phenocrysts and chrome spinel crystals, p. 63.

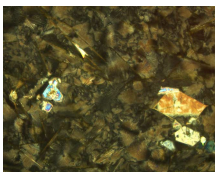

F37. Unaltered olivine phenocrysts and altered spherulite, p. 64.

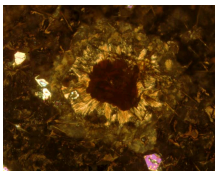

F38. Completely altered area, p. 65.

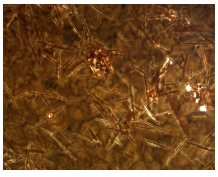

Upper Alteration Zone

Alteration in all the basalt cored in Hole 1185A and in the upper part (Units 1–9) of Hole 1185B occurred under highly oxidizing conditions and with high water-rock ratios. These characteristics differ significantly from those at Site 1183. The oxidative alteration led to the development of light and dark yellow-brown colors through the complete replacement of olivine and the pervasive alteration of groundmass near the outer zones of cooling units (e.g., pillow margins; Fig. F48). Away from pillow margins, the color grades into dark brown and dark gray in the coarser grained pillow interiors (Fig. F49). However, the aphanitic basalt adjacent to glassy pillow rims is generally almost black, with the exception of brown spherulites (Fig. F20). The spherulites range in diameter from 3 to 6 mm. They formed around olivine phenocrysts as the result of rapid cooling of the basaltic magma near pillow margins. Replacement of olivine by smectite and Fe oxyhydroxide enhances the fibroradial textures by staining the acicular plagioclase and clinopyroxene crystals radiating from the olivine nuclei (Fig. F50). Where abundant, spherulites give the basalt a striking mottled appearance, which is characteristic of Cores 192-1185B-3R (Unit 1), 4R (Unit 2), 9R (Units 7–9), and 10R (Unit 9) from the upper part of Hole 1185B (Fig. F21). Spherulites were not observed in the massive lava flows from the lower part of Hole 1185B (below Core 192-1185B-16R). In the upper alteration zone, basalts commonly have partially altered glassy pillow margins that grade into black aphanitic pillow interiors. A few spectacularly colorful hyaloclastites cemented by calcite are also present in this zone (Fig. F51).

Secondary minerals are predominantly smectite (saponite and nontronite) and Fe oxyhydroxide. The same secondary minerals fill miarolitic cavities and have partly to completely replaced glassy mesostasis. Olivine phenocrysts are commonly completely replaced by smectite, Fe oxyhydroxide, and, more rarely, calcite (Figs. F52, F53). Unaltered olivine is seen only in aphanitic dark gray to black areas close to pillow rims. Rare replacement of the wall rock proximal to veins by zeolite is observed in thin section (Fig. F54).

Lower Alteration Zone

Basalts below Core 192-1185B-16R show a dramatic change in alteration character to a type similar to that observed at Site 1183. The top of Core 192-1185B-17R (Unit 10) contains breccia made up of angular basalt fragments cemented by sediment; these fragments are the most pervasively altered basaltic material observed during Leg 192 (Fig. F55). Such severe alteration is probably the result of exposure of a highly permeable basaltic seafloor to bottom seawater over an extended period, possibly several million years. This means that Units 9 and 10 probably belong to totally separate episodes of plateau construction. For the basement to remain exposed to seawater during a long period, the sedimentation rate had to be small and/or the basement cropped out along fault scarps.

The groundmass in Core 192-1185B-17R and Sections 192-1185B-20R-1 and 21R-1 is characterized by a dusky green color caused by pervasive replacement by celadonite. Olivine phenocrysts in these basalts are also replaced by celadonite (Fig. F56). Dark yellowish brown to olive and gray are the most common colors, respectively, in halos and in pillow interiors. The least altered basalt below Core 192-1185B-16R is dark

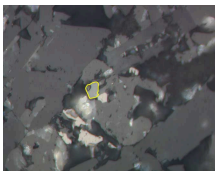

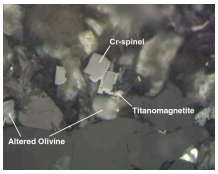

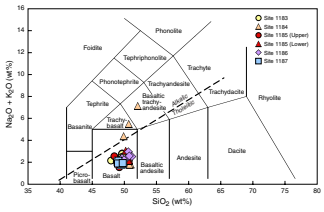

gray (Fig. F57). Secondary minerals replacing groundmass and olivine phenocrysts in the dark yellowish brown areas are predominantly smectite with Fe oxyhydroxide (Fig. F58). The gray basalts do not contain Fe oxyhydroxide and have celadonite as a minor component. Calcite is present as a minor phase filling miarolitic cavities and vesicles, together with smectite and celadonite in gray and dusky green basalt and together with smectite and Fe oxyhydroxide in dark yellowish brown basalts (Figs. F59, F60). Unaltered glass is much rarer below the top of Core 192-1185B-17R, largely as a result of the abundance of thicker, massive igneous units (and a scarcity of pillow rims) in the lower part of the hole rather than because of a higher degree of glass alteration.

Veins

Veins throughout Holes 1185A and 1185B predominantly contain calcite, zeolites (common phillipsite and rare gmelinite/chabazite), smectite, Fe oxyhydroxide, and rare celadonite and pyrite (Figs. F61, F62, F63, F64, F65). Some veins are filled with micritic pink carbonate that contains Fe oxyhydroxide pellets and foraminifer ghosts, indicating that the veins are sediment-filled open fissures (Fig. F66). These veins range in width from a few centimeters to <1 mm and are located both near the upper boundaries of units and within units, raising the question of the mechanism by which sediments can migrate down into basaltic crust.

Broad (centimeter scale), dusky green halos are developed near veins of Sections 192-1185B-17R-4, 20R-3, and 21R-1 through 21R-3. Reduction fronts that extend a few millimeters to centimeters beyond these halos and consist of scattered pyrite grains are common in the groundmass of the dark gray rock interiors. The dusky green halos may be equivalent to the black halos we described from Site 1183; the greenish shade results from the higher abundance of celadonite. Smaller (millimeter scale) brown halos are developed close to veins and occur both as discrete features and in association with dusky green halos. Where dusky green halos are associated with brown halos, the latter are commonly located proximal to the vein and the former extend toward the dark gray basalt interiors (Fig. F67).

We noticed a clear relationship between vein density and host-rock alteration color. The lighter yellow-brown colors in the basalts are generally associated with portions of cores displaying more horizontal and subhorizontal veins; that is, from 3 to 6 veins per 10 cm of core length (Fig. F49). The degree of alteration is highest in the rocks with the highest permeability (e.g., fractured pillow lavas, hyaloclastites, and breccias) in which the rock color is also the lightest. The reason why horizontal and subhorizontal open fractures are most abundant in some upper portions of cooling units remains to be explained.

STRUCTURAL GEOLOGY

Apart from abundant veins, rocks obtained from Holes 1185A and 1185B exhibit relatively few structural features. The sediments that overlie the basaltic basement are characterized by horizontal bedding planes and appear to be unaffected by either tilting or faulting (see "Lithostratigraphy," p. 5). No ductile or cataclastic fault zones or tectonic breccias were encountered in the cores.

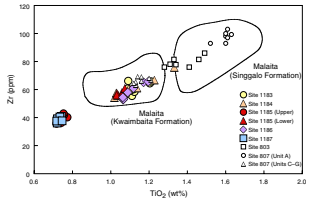

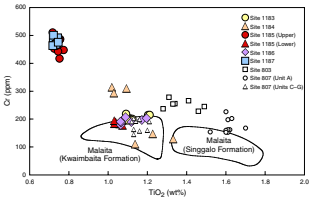

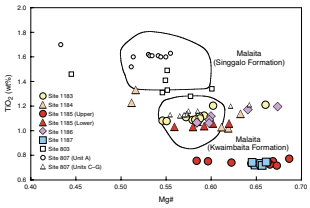

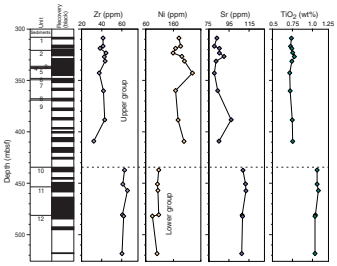

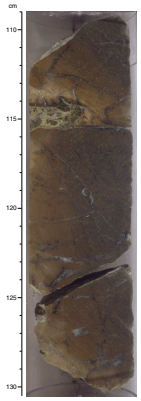

Location, vein width, and mineral filling have been documented for 2350 veins in the vein-structure log for this site. True dip was measured for 110 veins. For an additional 890 veins, we calculated true dip from measurements of apparent dip. The graphic presentation of fracture density, vein abundance, and true dip in Figures F68 and F69 provides some information about the relationship between vein characteristics and basement depth. The fracture density has been calculated per meter of core section. A vein thickness of 0.25 mm has been assumed to be a representative average for veins described as hairline veins in calculating vein abundance.

Basement penetration in Hole 1185A was 20.2 m. The data presented in Figure F68 are characterized by a random distribution and indicate significantly higher fracture and vein densities than those recorded for Hole 1183A (Fig. F68).

Hole 1185B yielded a 216.6-m-thick sequence of alternating pillow basalts and massive basalt flows subdivided into 12 basement units (see "Igneous Petrology," p. 11). The outer parts of pillows have much higher fracture densities than the inner parts or than the massive flows. The pillows are characterized by two types of vein orientations: concentric veins, which are located toward pillow margins, and radial veins, which extend from the center toward the pillow margin. Massive lava flows and the inner parts of large pillows are characterized by low fracture density, with veins oriented between 0° and 30°.

The relationship between depth in basement and dip inclination is random (Fig. F69). However, fracture density and vein abundance show some variation with depth, unlike those observed in Hole 1183A. These parameters reflect the presence of either pillow or massive flow sequences and show a general correlation with the 12 basement units (see "Igneous Petrology," p. 11). Massive flows typically have a fracture density of 20 veins/m and a vein abundance of 20 mm/m. Pillow lavas have fracture densities between 30 and 65 veins/m and vein abundances of 60–100 mm/m.

The absence of downhole logging information and structural marker planes (e.g., sedimentary or basaltic layering) precludes reorientation of the measured veins and the calculation of dip azimuths. Paleomagnetic results may enable reorientation of some of the veins on larger pieces during shore-based analysis of the data (see "Paleomagnetism," p. 18) and allow the calculation of dip azimuths.

PALEOMAGNETISM

Introduction

Pass-through magnetometer measurements were taken on all split-core archive sections. Sediment cores were measured at 5-cm intervals. Coherent basalt pieces that could be oriented unambiguously with respect to the top were measured at 1-cm intervals. Pass-through magnetic susceptibility measurements were taken on all unsplit core sections at 4-cm intervals.

In order to isolate the characteristic remanent magnetization (ChRM), cores were subjected to alternating-field (AF) cleaning. The number of AF demagnetization steps and peak-field intensity varied depending on lithology, the natural remanent magnetization (NRM) intensity, and the amount of time available. On average, sediment half-cores were demagnetized using three AF steps in addition to the

F49. Color gradations in pervasively altered basalt, p. 76.

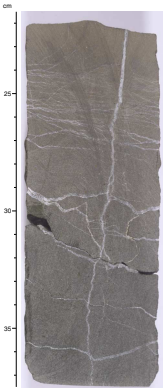

F50. Spherulite in yellow-brown halo, p. 77.

F51. Altered hyaloclastite, p. 78.

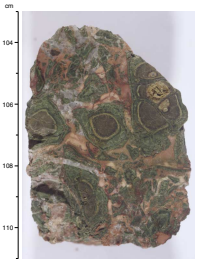

F52. Altered basalt from yellow-brown halo, p. 79.

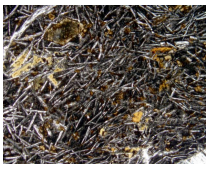

F53. Altered basalt from near calcite veins, p. 80.

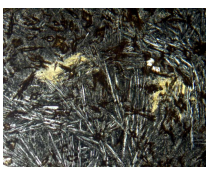

measurement of NRM. The basalt half-cores were demagnetized using a minimum of six AF steps. The maximum applied field ranged between 25 and 80 mT. We analyzed the results in Zijderveld and stereoplot diagrams; where possible, we calculated the ChRM direction using principal component analysis (Kirschvink, 1980). Examples of the AF demagnetization of sediment and basalt samples are shown in Figure F70.

Results from Sedimentary Units

Magnetostratigraphy

We were able to reliably identify the magnetic polarity of sediment Cores 192-1185A-2R through 6R and Core 192-1185B-2R. We used the sequence of polarities together with the available biostratigraphic information (see "Biostratigraphy," p. 7) to develop a correlation with the geomagnetic polarity timescale (GPTS) of Berggren et al. (1995) (Fig. F71). Some of our correlations are tightly constrained, whereas others are more tentative. For example, the reverse polarity of Core 192-1185A-4R can be correlated reliably with Chron C16r as this interval of reverse polarity is the only such interval within nannoplankton Zone NP18. The normal polarity of Core 192-1185A-5R correlates well with the normal polarity interval (C17n.1n) that is older than C16r but which is still identified within NP18.

Both Cores 192-1185A-2R and 3R are dated within foraminifer Zones P16 and P17 and nannoplankton Zone NP 19/20. Core 2R is entirely reversely magnetized, and we observe a transition downward within Core 3R from normal to reverse polarity. Only one normal-to-reverse transition took place during the time period represented by both NP19/20 and P16; consequently, the transition in Core 3R is C15n–C15r (Fig. F71). Because only one reverse polarity interval younger than Chron C15r is present within P16, the reverse polarity of Core 2R is Chron C13r.

Biostratigraphic information suggests a possible hiatus spanning a portion of Zone P15 near the middle to upper Eocene boundary (see "Biostratigraphy," p. 7), but all or part of nannoplankton Zones NP 19/20, 18, and 17 are present. If an appreciable hiatus exists, then we cannot uniquely correlate the normal polarity of Core 192-1185A-6R with the GPTS. We have chosen to use the age controls provided by the nannoplankton zones and have therefore correlated this normal polarity zone with Chron C17n.1n and view it as a continuation from Core 5R. Nannoplankton Zone NP 17 corresponds to a time during which there were several normal polarity intervals. Therefore, the normal polarity may correspond to another normal polarity interval between C17n.1n and Chron C18n.2n. Samples from the topmost portion of Core 192-1185A-8R indicate nannoplankton Zone NP16 and an age no older than 42 Ma (see "Biostratigraphy," p. 7). Unfortunately, the top of Core 8R was unsuitable for pass-through magnetometer measurements, and the magnetic polarity of these sediments could not be determined. Based on the evidence provided by Cores 192-1185A-6R and 8R, we have tentatively correlated the mixed polarities observed within Core 192-1185A-7R with the multiple polarity transitions associated with Chrons C17n.2n and C17n.3n. This correlation is consistent with available biostratigraphic information (which indicates that Zone NP17 nannofossils are present in Core 192-1185A-7R-CC) but is not required

F54. Replacement of basalt, p. 81.

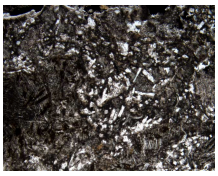

F55. Pervasively altered angular basalt fragments in breccia, p. 82.

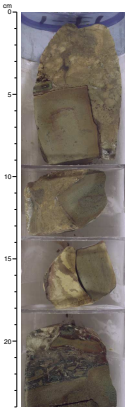

F56. Olivine phenocrysts totally replaced by celadonite, p. 83.

F57. Olive halos and dusky green basalt near calcite-smectite vein, p. 84.

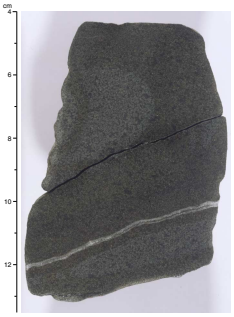

F58. Typical gray, fine-grained basalt, p. 85.

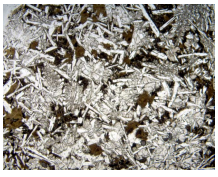

by it, and the mixed polarity zone could correspond to other parts of the reversal scale between Chrons C17n.2n and C18r.

Core 192-1185B-2R is entirely reversely magnetized and lies within nannoplankton Zone NP16 and within foraminifer Zone P12. These zones overlap considerably and therefore provide little additional time resolution. Two periods of reverse polarities, C18r and C19r, are spanned by NP16 and P12; the correlation of Core 192-1185B-2R to the GPTS is therefore ambiguous (Fig. F71).

Paleolatitude

The results of AF demagnetization of sediments recovered from Hole 1185A did not allow a definition of the ChRM direction precise enough for paleolatitude studies. However, the AF demagnetization results for Core 192-1185B-2R (Fig. F70A) allowed principal component analysis, and we were able to determine a paleolatitude for this core. A mean inclination of –24.4° ± 2.2° was obtained, which is equivalent to a paleolatitude of 12.8° ± 1.3°S. Correlation of the reversed polarity observed in Core 2R with Chron C18r or C19r indicates an age in the 40.1- to 42.5-Ma interval (Fig. F71). This age control is sufficiently accurate to allow us to compare the paleolatitudinal position of Site 1185 with that obtained for material of similar age from Site 1183. The paleolatitude, 12.8°S, at Site 1185 agrees remarkably well with that at Site 1183 (12.5°S).

Results from Basaltic Units

The basalt cores showed a variable degree of overprinting with a near-vertical secondary magnetization most likely induced by drilling. Although the amount of overprinting varied, in almost all cases we were able to remove it with 10- to 20-mT AF demagnetization and to isolate the ChRM direction using higher fields (e.g., Fig. F70B). In Table T9 we list the ChRM direction, NRM intensity, magnetic susceptibility, Koenigsberger ratio, and median destructive field (MDF) for all coherent basalt pieces longer than 15 cm for which a reliable ChRM direction could be defined. For coherent pieces longer than 50 cm we list data for roughly every 25 cm. The ChRM inclinations obtained from different parts of long, coherent pieces generally agree within a few degrees.

Rock Magnetic Properties

Although Holes 1185A and 1185B are only 20 m apart, we were unable to uniquely correlate the magnetic properties (Fig. F72) or the ChRM directions (Fig. F73), probably indicating that different cooling units (pillow lavas) were recovered in the two holes. In Figure F72, the downhole variation in the rock-magnetic parameters of both Holes 1185A and 1185B is plotted on a common depth scale. We observe a distinct difference between the pillow lavas, with relatively low magnetic susceptibility and high MDF, and the more massive lava flows, with high susceptibility and low MDF. This difference can be explained by either the finer grain size of the pillow lavas or their higher degree of low-temperature alteration (see "Alteration," p. 15), or a combination of these factors. Shore-based rock magnetic studies on discrete samples will investigate the cause of the downhole variation in rock-magnetic properties.

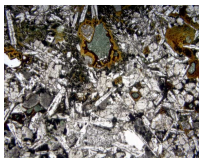

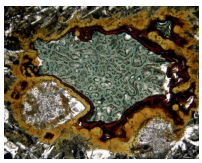

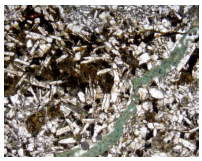

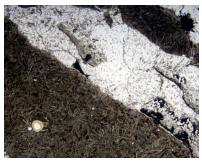

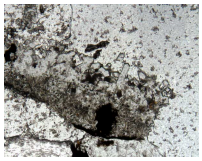

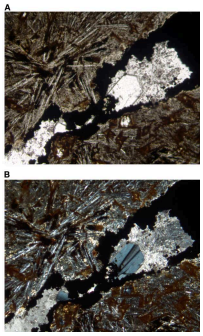

Magnetostratigraphy and Definition of Paleomagnetic Units

The magnetic inclination is negative for all 162 ChRM determinations (Table T9), indicating normal polarity for all basalt cores recovered. The normal-polarity magnetization is consistent with biostratigraphic analyses of limestone interbeds that indicate a late Aptian to earliest Turonian or latest Cenomanian age (see "Biostratigraphy," p. 7) and, hence, basalt emplacement during the Cretaceous Normal Superchron. In order to define the downhole variation in the paleomagnetic inclination data, we combined the individual ChRM data into distinct paleomagnetic units, each paleomagnetic unit being associated with a single cooling unit. Following the method of Kono (1980a), we calculated the statistic Z:

$$Z = \frac{Inc_1 - Inc_2}{\sqrt{\frac{\sigma_1^2}{n_1} - \frac{\sigma_2^2}{n_2}}},$$

where Inc_1 and Inc_2 are the means of two adjacent inclination groups, σ_1 and σ_2 are their standard deviations, and n_1 and n_2 are the number of inclination values in each group. The data are divided so that the inclination groups differ at the 95% confidence level ($Z > 1.96$). Using this criterion, the basement section in Hole 1185A can be divided into four paleomagnetic units and that in Hole 1185B into 18 paleomagnetic units (Table T10). Note, however, that this statistical test could not be used on those paleomagnetic units that are based on only one ChRM determination.

In most cases the paleomagnetic unit boundaries conform with basement unit boundaries. In some cases, however, we observe more than one paleomagnetic unit within a single basement unit. This apparent discrepancy is not surprising because individual basement units often contain several chilled margins (see "Igneous Petrology," p. 11). The only notable example of a paleomagnetic unit that includes more than one basement unit is paleomagnetic Unit B14 (see Fig. F73), which includes the lower 17 m of basement Unit 9 as well as the upper 1 m of Unit 10. The boundary between Units 9 and 10 marks a distinct change in chemical composition (see "Igneous Petrology," p. 11) and possibly a major hiatus in volcanic activity (in accordance with the high degree of low-temperature alteration at the top of Unit 10; see "Alteration," p. 15). We speculate that the upper part of Unit 10 was remagnetized when the lower part of Unit 9 was emplaced, either directly by heating from the overlying flow or by accompanying chemical alteration. We note that the rock-magnetic properties in the uppermost meter of Unit 10 are slightly different from those in the lower part of the unit (see Fig. F72).

Paleolatitude

Using the statistics of Kono (1980b), we have calculated the mean inclination for all 22 paleomagnetic units (Table T11). As previously mentioned, a major hiatus in volcanic activity may be present between basement Units 9 and 10 in Hole 1185B. We have therefore also calculated the mean inclination for the paleomagnetic units above and below this suspected volcanic hiatus (Table T11). The upper group, comprising paleomagnetic Units A1–A4 and B1–B14, have a

F65. Botryoidal aggregate in calcite vein, p. 92.

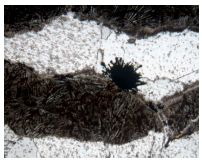

F66. Micritic sediment and sparry calcite vein, p. 93.

F67. Complex halos near smectite veins, p. 94.

F68. Basement recovery, fracture density, vein abundance, and true dip, Hole 1185A, p. 95.

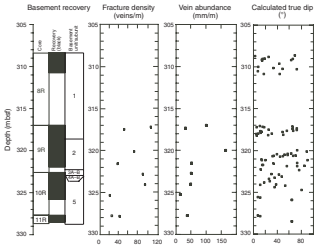

F69. Basement recovery, fracture density, vein abundance, and true dip, Hole 1185B, p. 96.

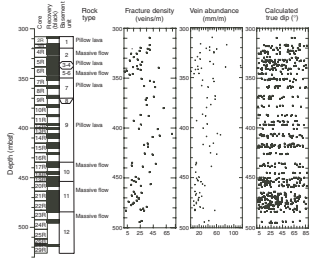

somewhat shallower inclination and correspondingly less southerly paleolatitude than the lower group, comprising Units B15–B18. Although this result supports a possible time gap between the two groups, the lower group comprises only four paleomagnetic units and therefore does not provide a statistically adequate sample to give confidence to this distinction. Shore-based studies of discrete samples are necessary in order to better define the paleomagnetic units and possibly identify new units not detected in our pass-through measurements.

A basic assumption when converting the inclination of the paleomagnetic field to paleolatitude is that secular variation has been averaged. The angular standard deviation (ASD) listed in Table T11 gives a direct measure of the paleosecular variation at the time and paleolatitude where the lavas were emplaced. The ASD values observed at Site 1185 agree well with the expected ASD value of 12° obtained from McFadden et al.'s (1991) global compilation of paleosecular variation from lavas. We therefore feel confident that the mean inclinations for the first two groups (i.e., all paleomagnetic units and Units A1–A4 and B1–B14) in Table T11 represent a time-averaged geocentric dipole field and that the paleolatitude calculation is valid. Finally, we note that the sediment-basement seismic reflection is horizontal and there is no evidence for local tectonic rotation of the basalts at Site 1185 (see "Background and Objectives," p. 1).

A comparison between Site 1185 and previously obtained paleolatitudes is difficult because of the poor age control of the Site 1185 basalts. We note, however, that, if the younger limit of the age estimate for the upper basalt sequence (latest Cenomanian) is correct, the Site 1185 paleolatitude would be in good agreement with the paleolatitude obtained from slightly younger sediments from Site 1183 (see "Paleomagnetism," p. 32, in the "Site 1183" chapter).

PHYSICAL PROPERTIES

Introduction

Index properties, including wet bulk density, grain density, dry bulk density, water content, void ratio, and porosity, were measured on discrete samples taken from most of the cores recovered from Site 1185. Whole sections of these cores were also run through the multisensor track (MST) to measure magnetic susceptibility, gamma ray attenuation (GRA) bulk density, and natural gamma radiation (NGR). We measured sonic compressional (*P*-wave) velocities on cut samples and, where possible, in more than one direction on oriented cubes to investigate velocity anisotropy. Thermal conductivity was measured on split rock samples from most of the cores.

Index Properties

We measured the wet mass, dry mass, and dry volume of each sample taken from the cores from Holes 1185A and 1185B and calculated wet and dry bulk density, water content, grain density, and porosity (Table T12; Figs. F74 and F75). In the sediments of Unit II from Hole 1185A, between 250.9 and 300.2 mbsf, grain densities generally are between 2.1 and 2.6 g/cm³, with a mean of 2.3 g/cm³; porosity averages 58.8%, and the mean bulk density is 1.6 g/cm³ (Fig. F74). The sediments from Unit II in Hole 1185B are represented by a single core section (see

F70. Zijderveld diagrams for archive-half core measurements, p. 97.

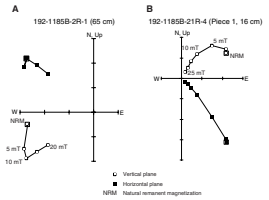

F71. NP zonation, magnetic polarity data, and correlation with GPTS, p. 98.

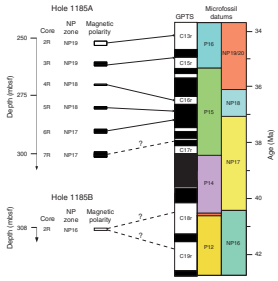

T9. ChRM direction, NRM intensity, MDF, magnetic susceptibility, and Q-ratio, p. 116.

F72. Variations in NRM, magnetic susceptibility, Q-ratio, and MDF, p. 99.

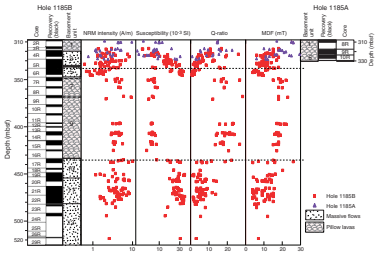

F73. Mean ChRM inclination variation for paleomagnetic units, p. 100.

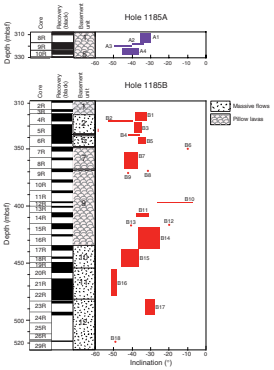

"Lithostratigraphy," p. 5); index properties data in this section are similar to those of Hole 1185A: grain density is 2.6 g/cm³, porosity is 47.1%, and bulk density is 1.9 g/cm³ (Fig. F75). The only sample of basement measured from Hole 1185A, a basalt from Unit 5, has much higher grain and bulk densities and a much lower porosity than the overlying sediments (Fig. F74). In the basalts from Hole 1185B, bulk densities are higher (>2.6 cm³) within basement Units 2, 5, 10, and 11 and lower (<2.6 cm³) in Units 3 and 6–9. In general, both grain and bulk densities decrease downhole in Units 4–9, corresponding to a lithologic change from dense basalt to heavily veined basalt. Below Unit 9, an increase in bulk density correlates with a lithologic change from veined basalt back to dense basalt in Units 10–12.

Multisensor Track Measurements

Magnetic Susceptibility

We determined magnetic susceptibility with the Bartington meter at 4-cm intervals along whole core sections from Holes 1185A and 1185B. The results, shown in Figures F76 and F77, are discussed in detail in "Paleomagnetism," p. 18. The peaks in magnetic susceptibility correlate well with the locations of dense basalt in each hole. For example, the magnetic susceptibility profile of basement units in Hole 1185A has three large spikes (>2000 × 10^{-5} SI units), one each in Sections 192-1185A-9R-1, 8–12 cm; 10R-3, 8–52 cm; and 11R-1, 40–52 cm (Fig. F76); these spikes correspond to intervals of dense basalt without veins. Similar features are seen in the magnetic susceptibility profile for Hole 1185B. As shown in Figure F77, heavily veined basalt in basement Units 6–9 exhibits much lower magnetic susceptibility values than the dense basalt both above and below these units.

Gamma Ray Attenuation Bulk Density

We estimated bulk densities from whole-core GRA measurements of the sections recovered from Holes 1185A and 1185B (Figs. F76 and F77). Because maximum GRA densities give the best approximation for the true bulk densities of sediment (Blum, 1997), the following description focuses on the maximum estimated values. In the chalk of Unit II in Hole 1185A, sampled between 250.7 and 308.6 mbsf, the average estimated maximum density is 1.6 g/cm³, the same as that determined from index samples from this hole. In Unit II of Hole 1185B, between 308.1 and 309.6 mbsf, the estimated maximum densities range from 1.5 to 2.3 g/cm³, with a mean value of 1.7 g/cm³ (Fig. F77). Below 308.6 mbsf in Hole 1185A, the estimated maximum bulk density increases to an average of 2.2 g/cm³ in basement Units 1–5 (Fig. F76). In the basalt from basement Units 2, 5, 10, and 11 from Hole 1185B, the estimated maximum densities have higher mean values (>2.4 cm³), whereas bulk densities for Units 1, 3, 4, 6–9, and 12 have lower values (<2.3 cm³). Comparison of the GRA downhole maximum bulk density profile for the basement (Fig. F77) with bulk density data obtained from discrete samples (Fig. F75) demonstrates that the two sets of measurements generally correlate, despite the consistently lower values of the GRA density data.

T10. Paleomagnetic Units A1–A4 and B1–B18, p. 119.

T11. Mean inclination, 95% confidence angle, precision parameter, ASD, and paleolatitude, p. 120.

T12. Index properties data, p. 121.

F74. Index properties and thermal conductivity vs. depth, Hole 1185A, p. 101.

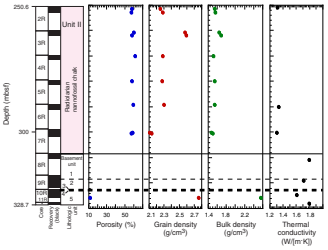

F75. Index properties and thermal conductivity vs. depth, Hole 1185B, p. 102.

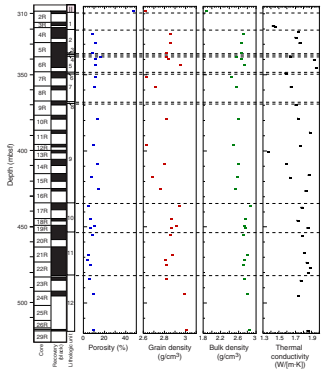

F76. Velocity and whole-core measurements vs. depth, Hole 1185A, p. 103.

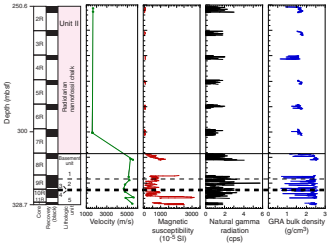

Natural Gamma Radiation

Although NGR measurements on unsplit sections of cores from both Holes 1185A and 1185B mostly show only minor fluctuations downhole (very low numbers of counts), there are a few peaks in the NGR profile of Hole 1185B (Fig. F77). For example, in basement Units 1, 4, 7, and 8, peaks of >6 cps are centered at ~317, ~338, ~350, and ~370 mbsf (Fig. F77). These peaks appear to correspond to downhole changes in other physical properties, such as velocity and magnetic susceptibility, most clearly seen across the Units 4–5 boundary at 338 mbsf (Fig. F77).

P-Wave Velocity

We calculated *P*-wave velocity from discrete measurements on both split-core sections and cut samples from Holes 1185A and 1185B (Table T13; Figs. F76 and F77). *P*-wave velocities in the chalk of Unit II from Hole 1185A, although based on only a few data points, average 1610 m/s. Only one velocity determination was made for Unit II from Hole 1185B, yielding a velocity of 1841.4 m/s. A sharp velocity increase occurs in the basaltic basement of Hole 1185A (Fig. F76). Between 310.5 and 328.2 mbsf in basement Units 1–5, *P*-wave velocities range from 4641.1 m/s to 5612.1 m/s, with a mean of 5121.9 m/s. In the basement units of Hole 1185B, *P*-wave velocities are lower (generally <5000 m/s) in Units 1, 4, 6, and 9, whereas velocities are typically >5000 m/s in Units 2, 3, and 10–12 (Fig. F77). The high *P*-wave velocities (> 5000 m/s) in these relatively unveined basalts are associated with high bulk and grain densities and low porosity values (Fig. F74).

Thermal Conductivity

We determined thermal conductivity in unsplit soft-sediment cores and on selected samples of lithified sediments and basaltic rocks from Holes 1185A and 1185B (Table T14; Figs. F74, F75). In Unit II from Hole 1185A, thermal conductivity generally is <1.3 W/(m·K). In basalt from the basement units, thermal conductivity, although variable, generally increases with depth, exhibiting a local maximum value of 1.8 W/(m·K) in the bottom of Unit 5 (Fig. F74). The average thermal conductivity for the basement units is 1.7 W/(m·K). Thermal conductivity in basement Unit 1 from Hole 1185B is relatively low, with a mean value of 1.4 W/(m·K). For the other basement units, thermal conductivity is generally >1.5 W/(m·K). The maximum and minimum values (at ~340 and ~400 mbsf, respectively, see Fig. F75) correspond to dense, massive, gray basalt in Section 192-1185B-6R-5 and yellowish brown basalt in Section 192-1185B-13R-1, respectively (see "Alteration," p. 15).

Concluding Remarks

Apart from slight differences in the depths of the lithostratigraphic units in Holes 1185A and 1185B (see "Lithostratigraphy," p. 5), cores from both holes exhibit similar physical properties. Changes in the physical properties of the sediments and basaltic rocks recovered from both holes correlate with changes in lithology. In both holes, index properties change abruptly at the sediment/basement interface. Several large magnetic susceptibility spikes that correlate well with the presence of dense basalt also were observed in both holes. For the most part, vari-

F77. Velocity and whole-core measurements vs. depth, Hole 1185B, p. 104.

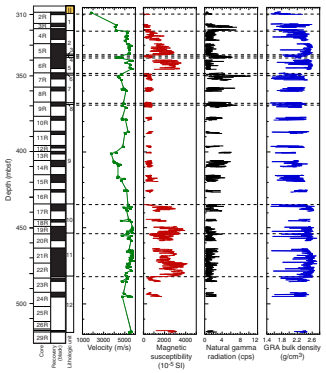

T13. *P*-wave velocity, p. 122.

T14. Thermal conductivity values, p. 124.

ations in physical properties within the basement units at Site 1185 appear to reflect the amount of alteration and veining in the basalts.

REFERENCES

Berggren, W.A., Kent, D.V., Swisher, C.C., III, and Aubry, M.P., 1995. A revised Cenozoic geochronology and chronostratigraphy. *In* Berggren, W.A., Kent, D.V., Aubry, M.-P., and Hardenbol, J. (Eds.), *Geochronology, Time Scales and Global Stratigraphic Correlation*. Spec. Publ.-–Soc. Econ. Paleontol. Mineral. (Soc. Sediment. Geol.), 54:129–212.

Birkhold-VanDyke, A.L., Neal, C.R., Jain, J.C., Mahoney, J.J., and Duncan, R.A., 1996. Multi-stage growth of the Ontong Java Plateau (OJP)? A progress report from San Cristobal (Makira), Solomon Islands. *Eos,* 77F:714.

Blum, P., 1997. Physical properties handbook: a guide to the shipboard measurement of physical properties of deep-sea cores. *ODP Tech. Note,* 26 [Online]. Available from World Wide Web: <http://www-odp.tamu.edu/publications/tnotes/tn26/INDEX.HTM>. [Cited 2000-09-08]

International Hydrographic Organization/Intergovernmental Oceanographic Commission (IHO/IOC), 1997. *General Bathymetric Chart of the Ocean (GEBCO) Digital Atlas:* London (British Oceanographic Data Centre).

Kirkpatrick, J.R., 1978. Processes of crystallization in pillow basalts, Hole 396B, DSDP Leg 46. *In* Dmitriev, L., Heirtzler, et al., 1978. *Init. Repts. DSDP,* 46: Washington (U.S. Govt. Printing Office), 271–282.

Kirschvink, J.L., 1980. The least-squares line and plane and the analysis of palaeomagnetic data. *Geophys. J. R. Astron. Soc.,* 62:699–718.

Kono, M., 1980a. Paleomagnetism of DSDP Leg 55 basalts and implications for the tectonics of the Pacific plate. *In* Jackson, E.D., Koizumi, I., et al., *Init. Repts. DSDP,* 55: Washington (U.S. Govt. Printing Office), 737–752.

————, 1980b. Statistics of paleomagnetic inclination data. *J. Geophys. Res.,* 85:3878–3882.

Kroenke, L.W., Berger, W.H., Janecek, T.R., et al., 1991. *Proc. ODP, Init. Repts.,* 130: College Station, TX (Ocean Drilling Program).

Le Bas, M.J., Le Maitre, R.W., Streckeisen, A., and Zanettin, B., 1986. A chemical classification of volcanic rocks based on the total alkali-silica diagram. *J. Petrol.,* 27:745–750.

Leckie, R.M., 1984. Mid-Cretaceous planktonic foraminiferal biostratigraphy off Central Morocco, Deep Sea Drilling Project Leg 79, Sites 545 and 547. *In* Hinz, K., Winterer, E.L., et al., *Init. Repts. DSDP,* 79: Washington (U.S. Govt. Printing Office), 579–620.

Macdonald, G.A., and Katsura, T., 1964. Chemical composition of Hawaiian lavas. *J. Petrol.,* 5:82–133.

Mahoney, J.J., Storey, M., Duncan, R.A., Spencer, K.J., and Pringle, M.S., 1993. Geochemistry and age of the Ontong Java Plateau. *In* Pringle, M.S., Sager, W.W., Sliter, W.V., and Stein, S. (Eds.), *The Mesozoic Pacific: Geology, Tectonics, and Volcanism*. Geophys. Monogr., Am. Geophys. Union, 77:233–262.

Martini, E., 1971. Standard Tertiary and Quaternary calcareous nannoplankton zonation. *In* Farinacci, A. (Ed.), *Proc. 2nd Int. Conf. Planktonic Microfossils Roma:* Rome (Ed. Tecnosci.), 2:739–785.

McFadden, P.L., Merrill, R.T., McElhinny, M.W., and Lee, S., 1991. Reversals of the Earth's magnetic field and temporal variations of the dynamo families. *J. Geophys. Res.,* 96:3923–3933.

Mochizuki, K., Coffin, M., and Eldholm, O., 1998. Upper crustal structure along an E-W transect from the Nauru Basin to the north-central Ontong Java Plateau. *Eos,* 79:F869.

Parkinson, I.J., Arculus, R.J., and Duncan, R.A., 1996. Geochemistry of Ontong Java Plateau basalt and gabbro sequences, Santa Isabel, Solomon Islands. *Eos,* 77F:715.

Perch-Nielsen, K., 1985. Mesozoic calcareous nannofossils. *In* Bolli, H.M., Saunders, J.B., and Perch-Nielsen, K. (Eds.), *Plankton Stratigraphy:* Cambridge (Cambridge Univ. Press), 329–426.

Sandwell, D.T., and Smith, W.H.F., 1997. Marine gravity anomaly from Geosat and ERS-1 satellite altimetry. *J. Geophys. Res.,* 102:10039–10054.

Shipboard Scientific Party, 1975. Site 289. *In* Andrews, J.E., Packham, G., et al., *Init. Repts. DSDP,* 30: Washington (U.S. Govt. Printing Office), 231–398.

Smith, W.H.F., and Sandwell, D.T., 1997. Global seafloor topography from satellite altimetry and ship depth soundings. *Science,* 277:1956–1962.

Tejada, M.L.G., Mahoney, J.J., Duncan, R.A., and Hawkins, M., 1996. Age and geochemistry of basement rocks and alkalic lavas of Malaita and Santa Isabel, Solomon Islands, southern margin of Ontong Java Plateau, *J. Petrol.,* 37:361–394.

Tejada, M.L.J., Mahoney, J.J., Neal, C.R., Duncan, R.A., and Petterson, M.G., in press. Basement geochemistry and geochronology of central Malaita, Solomon Islands, with implications for the origin and evolution of the Ontong Java Plateau. *J. Petrol.*

Tjalsma, R.C., and Lohmann, G.P., 1983. Paleocene-Eocene bathyal and abyssal benthic foraminifera from the Atlantic Ocean. *Micropaleontol. Spec. Publ.,* 4.

Toumarkine, M., and Luterbacher, H., 1985. Paleocene and Eocene planktic foraminifera. *In* Bolli, H.M., Saunders, J.B., and Perch-Nielsen, K. (Eds.), *Plankton Stratigraphy:* Cambridge (Cambridge Univ. Press), 87–154.

van Morkhoven, F.P.C.M., Berggren, W.A., and Edwards, A.S., 1986. Cenozoic cosmopolitan deep-water benthic foraminifera. *Bull. Cent. Rech. Explor.—Prod. Elf-Aquitaine,* 11.

Figure F1. Predicted bathymetry (after Smith and Sandwell, 1997) of the Ontong Java Plateau showing the locations of Site 1185 and other sites drilled during Leg 192 (stars). The plateau is outlined. Black dots = previous ODP and DSDP drill sites that reached basement; white dots = Site 288, which did not reach basement but bottomed in Aptian limestone, and Site OJ-7, which was proposed for Leg 192 but not drilled. The bathymetric contour interval is 1000 m (IHO/IOC, 1997).

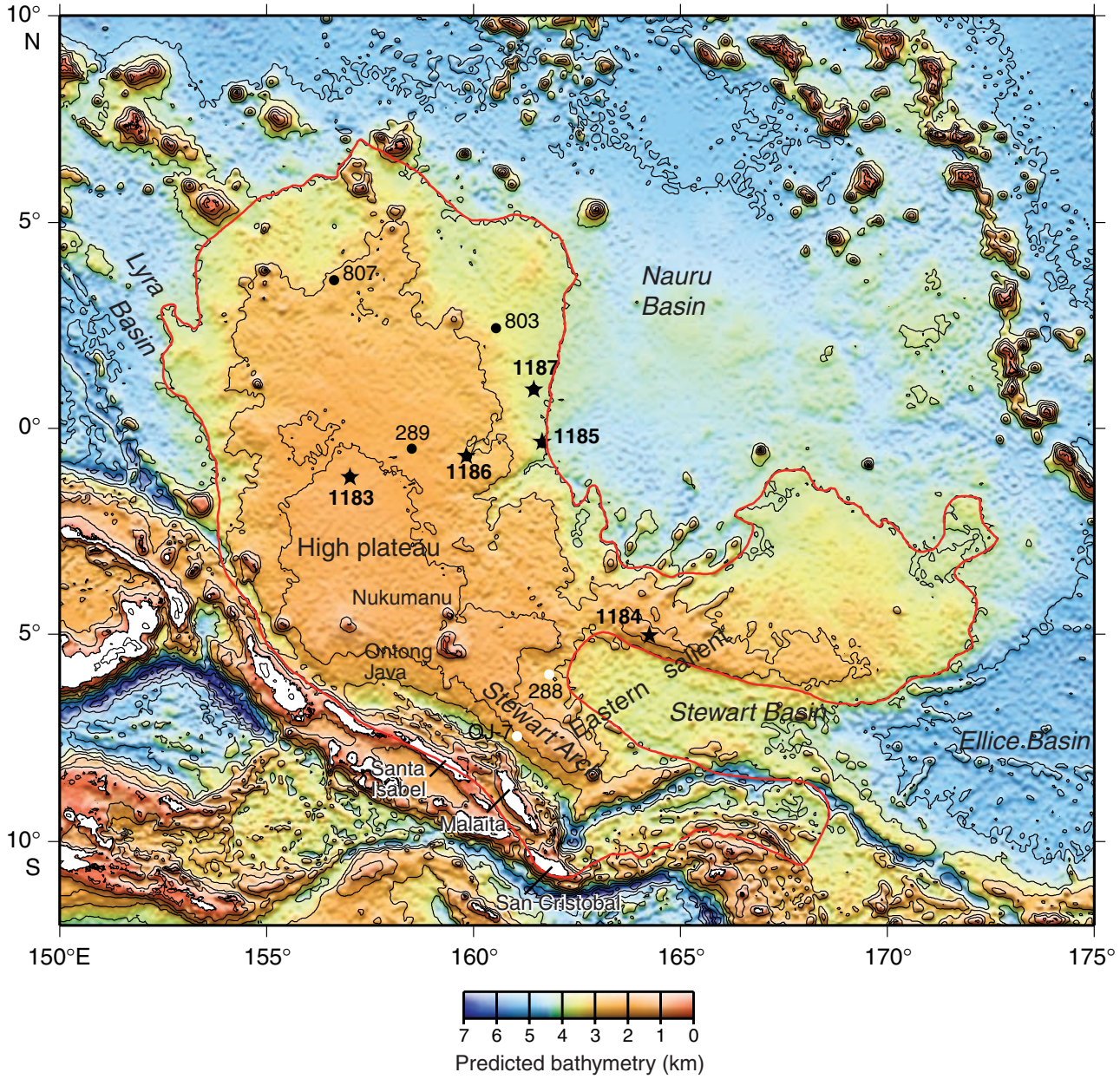

Figure F2. Satellite-derived free-air gravity map of the Ontong Java Plateau region (after Sandwell and Smith, 1997). Stars = locations of basement sites drilled during Leg 192. Black dots = previous ODP and DSDP drill sites that reached basement; white dots = Site 288, which did not reach basement but bottomed in Aptian limestone, and Site OJ-7, which was proposed for Leg 192 but not drilled. Black lines = surveys providing multichannel seismic control: *Hakuho Maru* KH98-1 Leg 2 (1998) and *Maurice Ewing* EW95-11 (1995). White lines = surveys providing single-channel seismic control: *Glomar Challenger* Leg 7 GC07 (1969), *Glomar Challenger* Leg 30 GC30 (1973), *Glomar Challenger* Leg 89 GC89 (1982), *Thomas Washington* TW-11 (1988), and *JOIDES Resolution* Leg 130 JR130 (1990). The bathymetric contour interval is 1000 m (IHO/IOC, 1997).

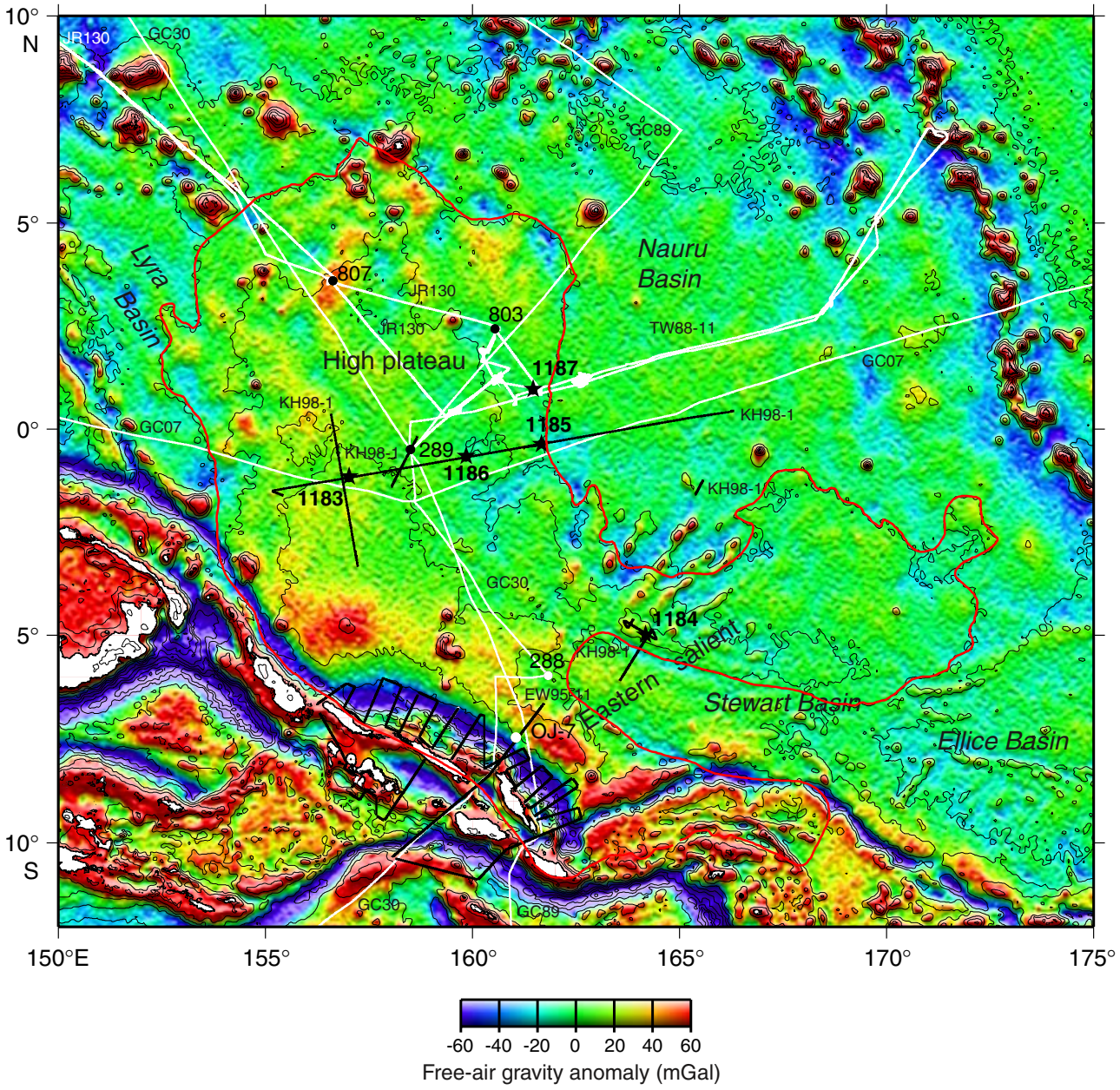

Figure F3. Location of Site 1185 and site-survey data on satellite-derived free-air gravity map (after Sandwell and Smith, 1997). Navigation for *Hakuho Maru* KH98-1 Leg 2 survey, Line 401, is shown in Julian-day time. Water depths in the survey area are between 3000 and 4500 m (IHO/IOC, 1997).

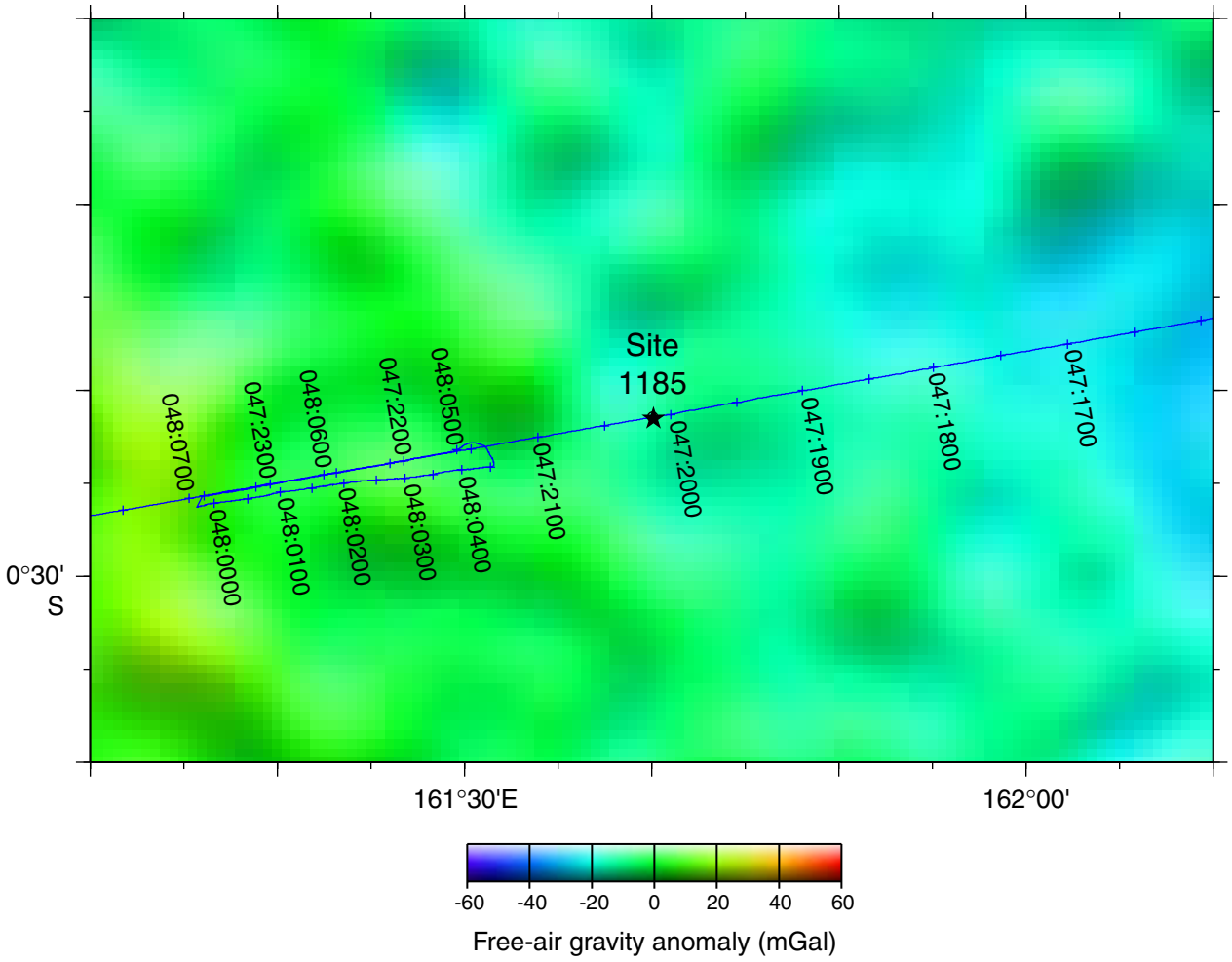

Figure F4. Multichannel seismic-reflection profile across Site 1185 (see Fig. F3, p. 30, for location). Vertical exaggeration is ~4.2 at seafloor. UTC = Universal Time Coordinated.

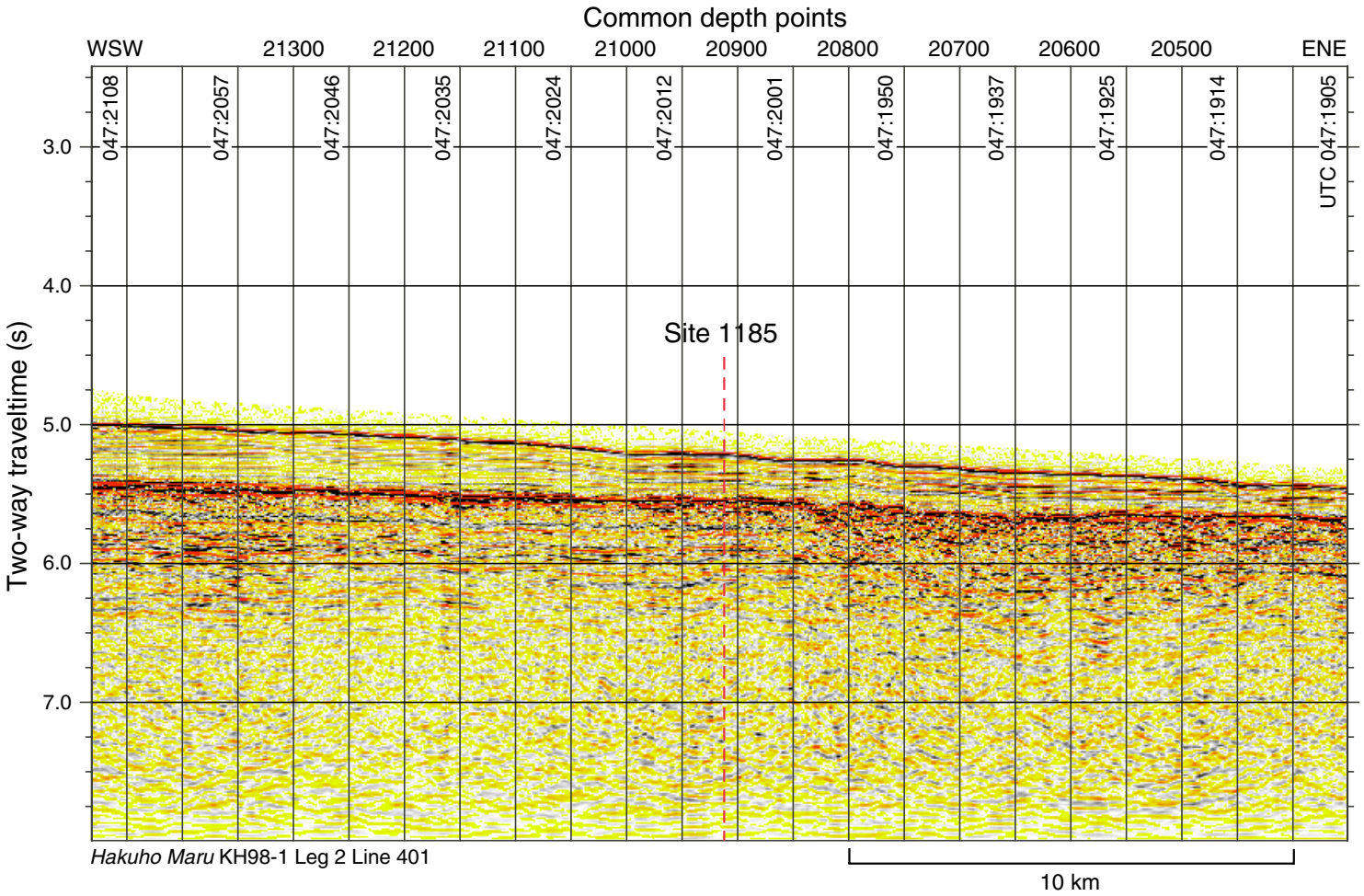

Figure F5. Multichannel seismic-reflection profile across Site 1185 (see Fig. F3, p. 30, for location). Vertical exaggeration is ~4.2 at seafloor. UTC = Universal Time Coordinated.

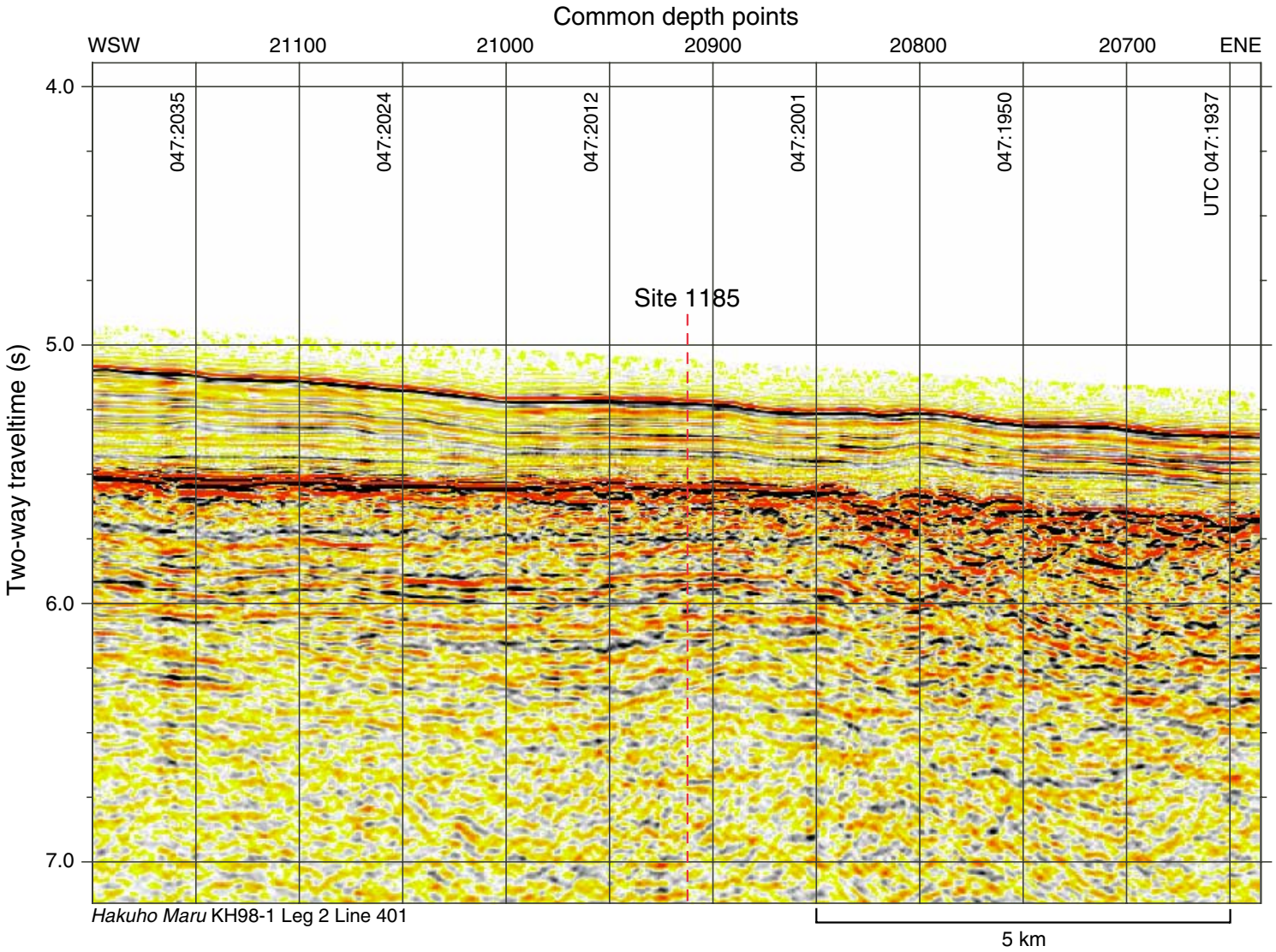

Figure F6. Multichannel seismic-reflection profile across Site 1185 (see Fig. F3, p. 30, for location). Vertical exaggeration is ~4.2 at seafloor. UTC = Universal Time Coordinated.

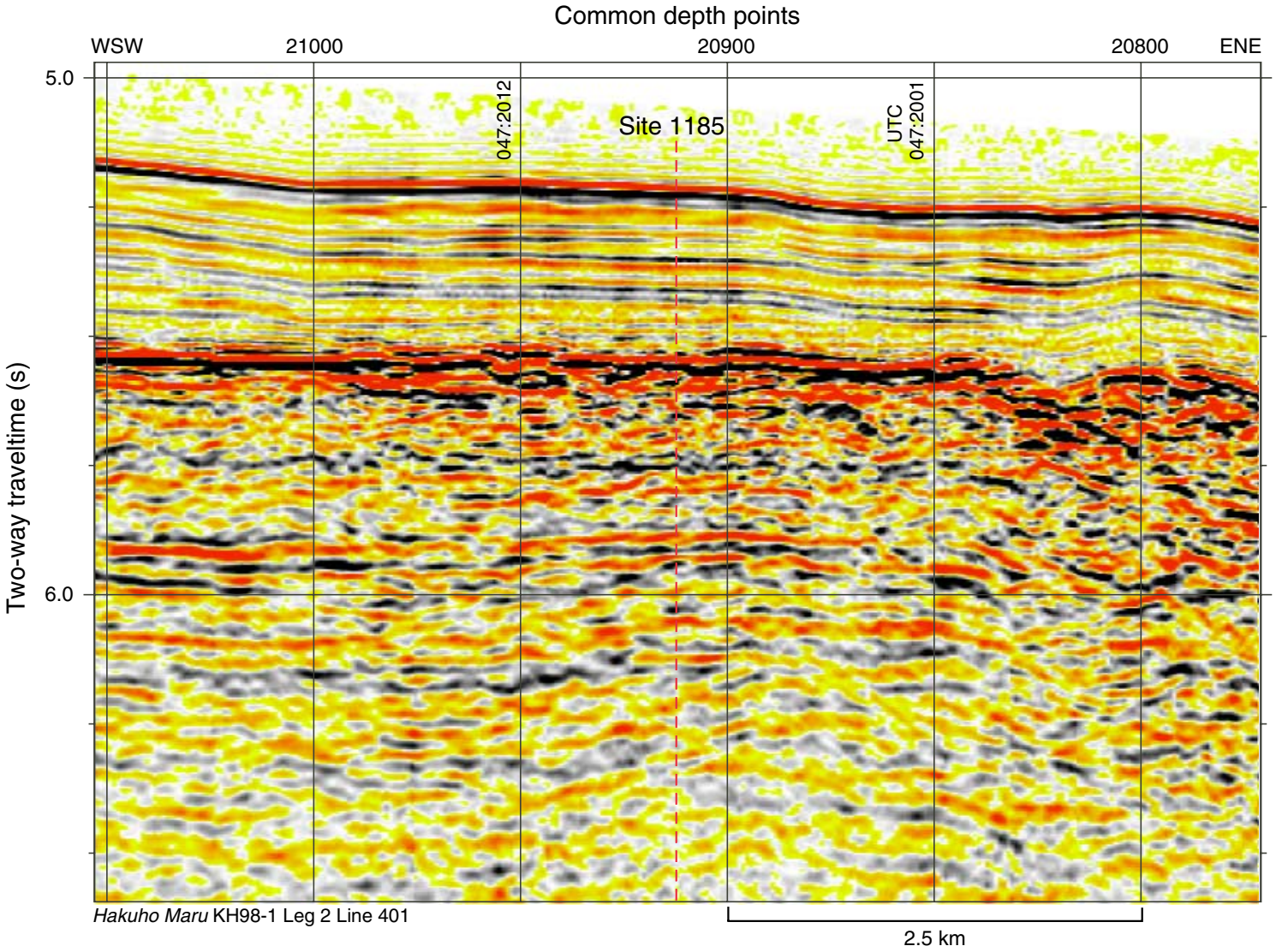

Figure F7. Multichannel seismic-reflection profile across Site 1185 (see Fig. F3, p. 30, for location). Vertical exaggeration is ~4.2 at seafloor. UTC = Universal Time Coordinated.

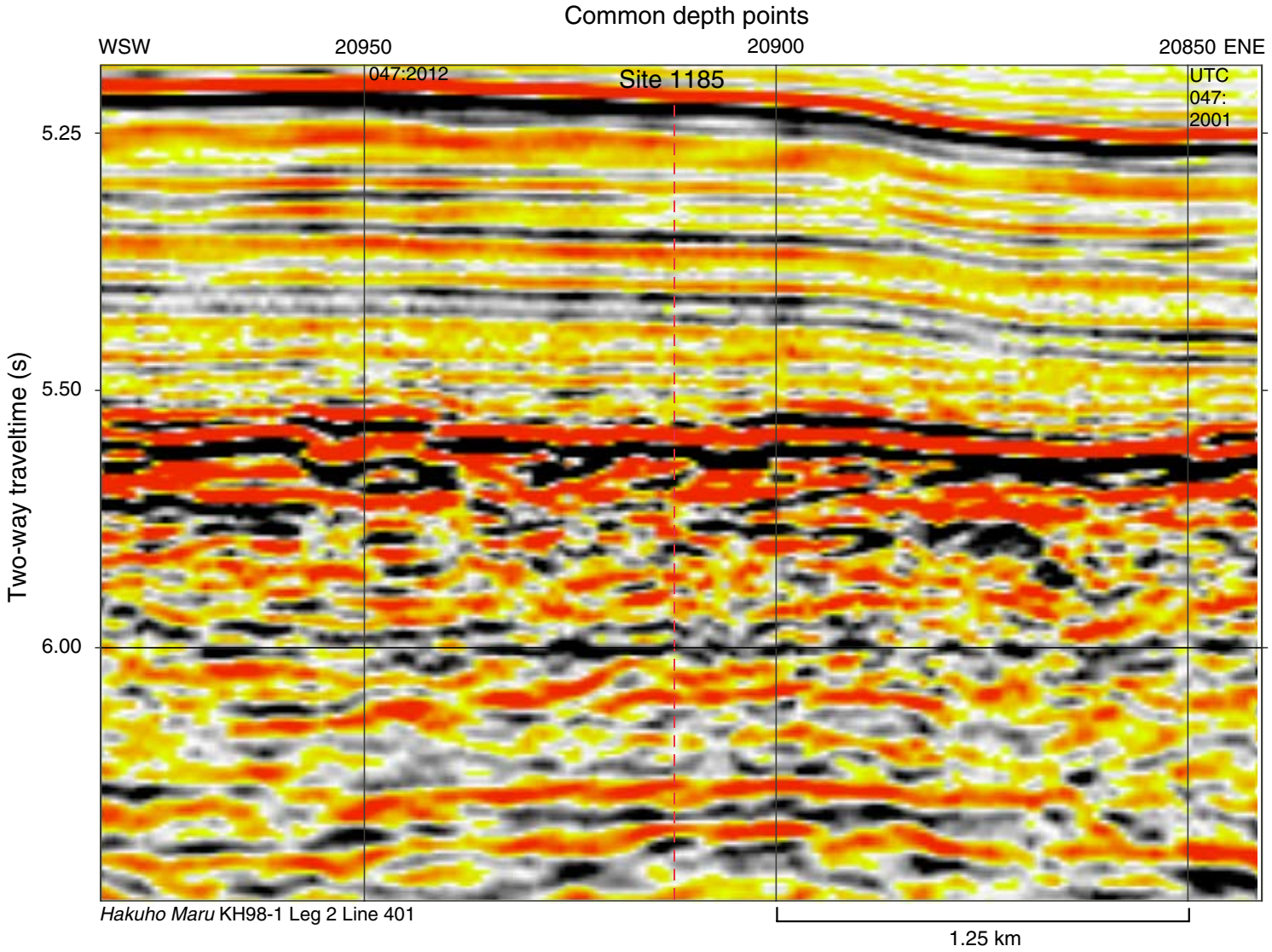

Figure F8. Core recovery (in black), lithologic divisions, schematic lithology, color, carbonate percentage, and components of sediments, Hole 1185A. L = total reflectance and indicates lighter shades to the right; "a" and "b" quantify the hue as chromaticity, where the a-axis shows variation between green (low values) and red (high values) and the b-axis shows variation between blue (low values) and yellow (high values) (Blum, 1997). Component percentages are from observation of smear slides and thin sections.

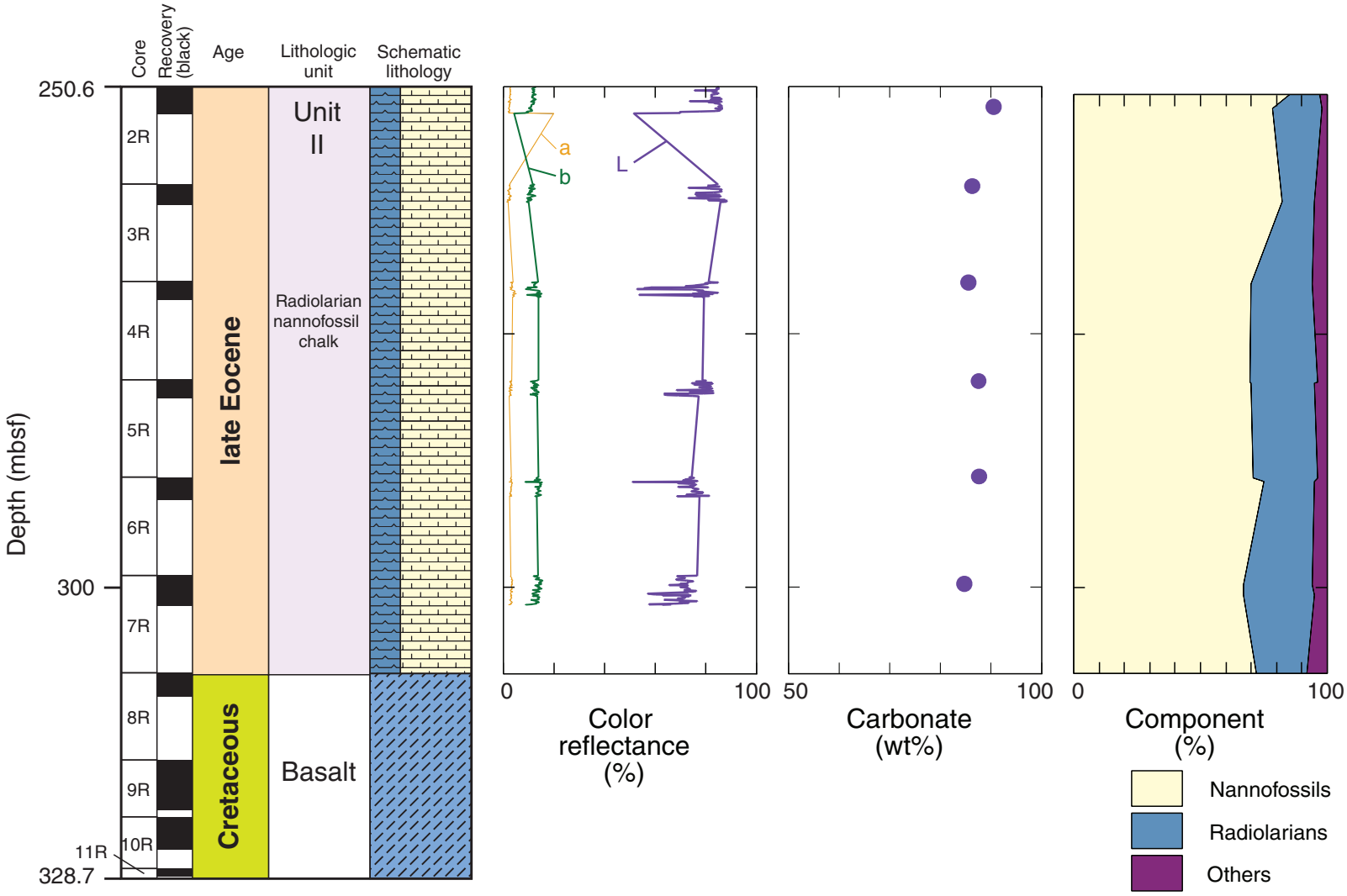

Figure F9. Typical light gray bioturbated chalk facies of Unit II (Eocene) from interval 192-1185A-6R-1, 120–140 cm.

Figure F10. Radiolarian nannofossil chalk in Sample 192-1185A-2R-2, 62–65 cm, Unit II, Eocene (field of view = 1.4 mm; plane-polarized light; photomicrograph ID# 1185AS_13). A few radiolarians are altered to calcite.

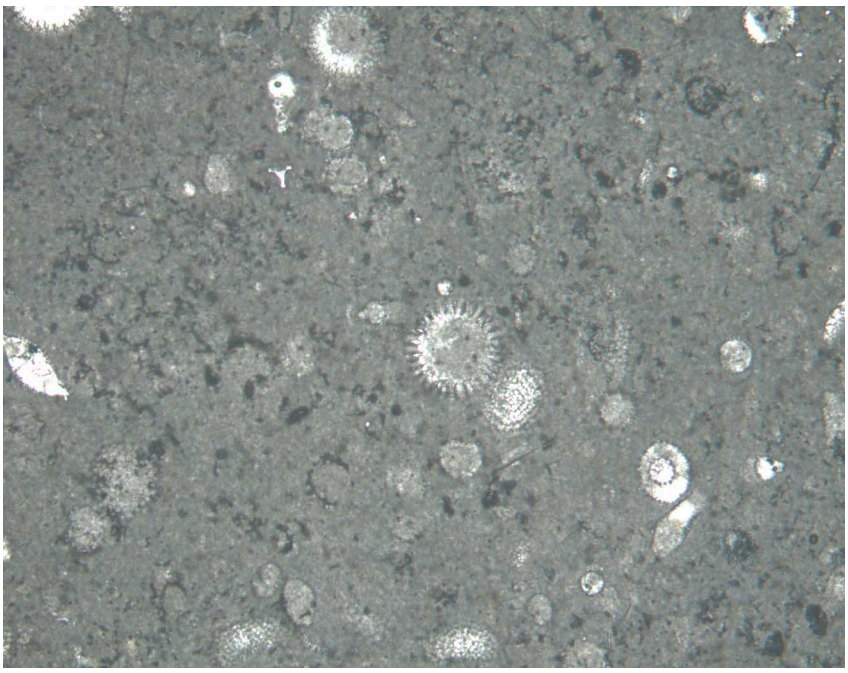

Figure F11. Abundant *Planolites*-type burrows in a whitish color band (interval 192-1185A-6R-2, 33–43 cm; Unit II; Eocene). Most burrows are surrounded by black particles, which may be pyrite grains.

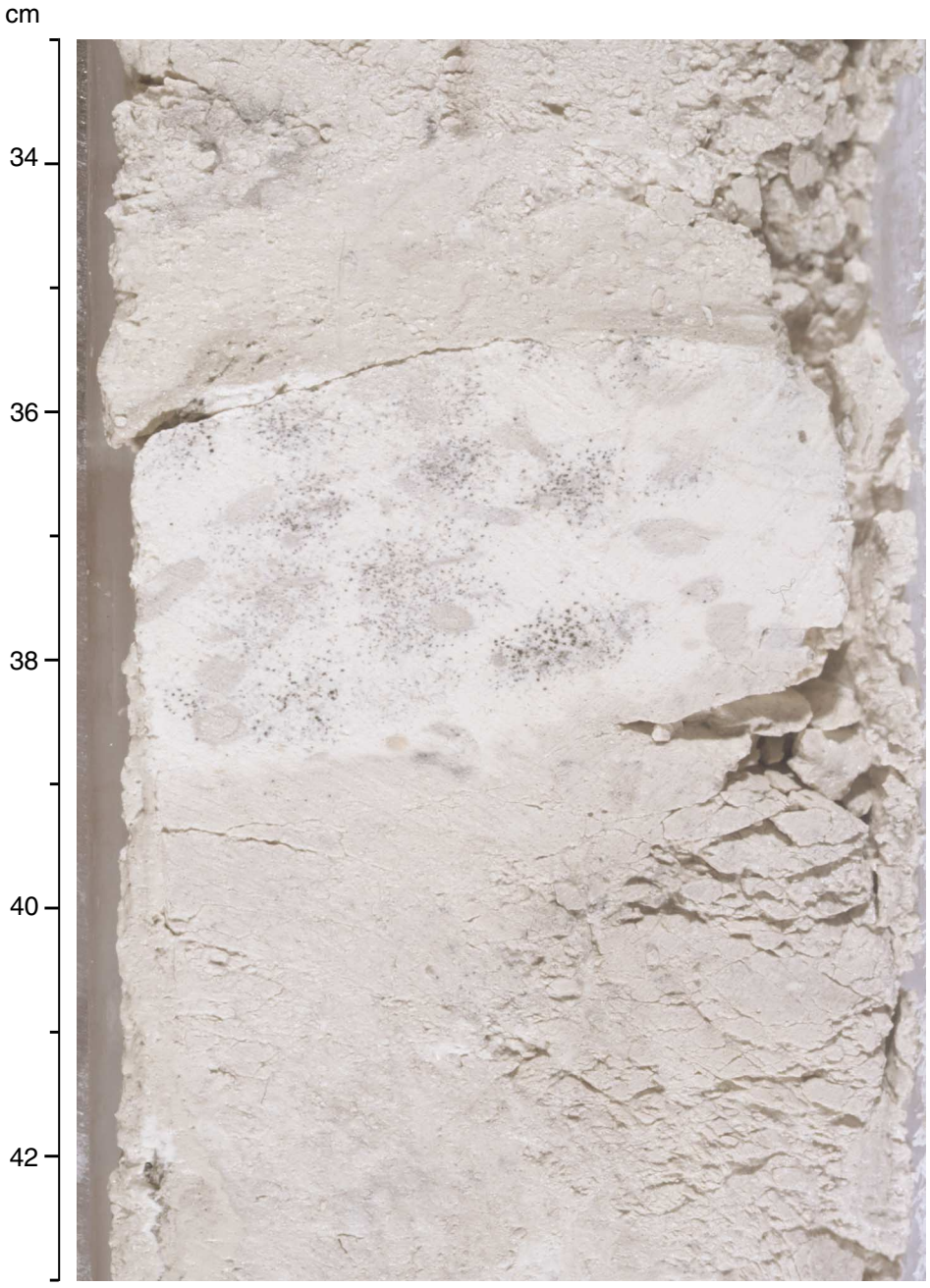

Figure F12. Contorted bedding caused by slumping (interval 192-1185A-7R-1, 120–150 cm; Unit II; Eocene). The slumped material is burrowed by *Planolites* at 138 cm, 141 cm, and 146.5 cm. Burrows are filled with material similar to the immediately overlying chalk.

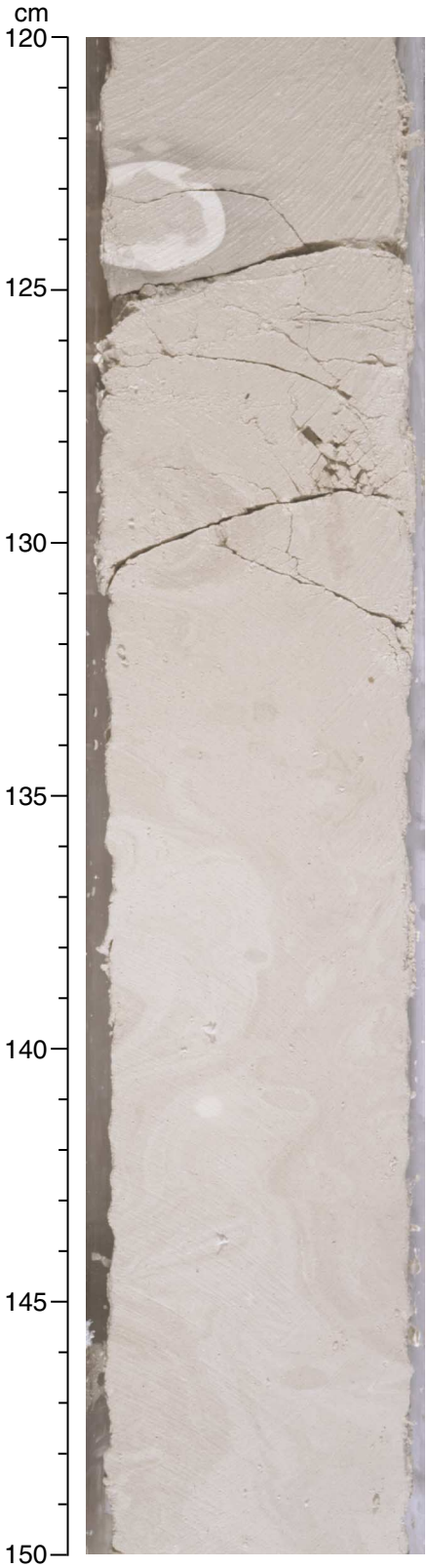

Figure F13. Interval 192-1185A-9R-4, 83–101 cm, showing the boundary between Unit 2 and Subunit 3A at 92 cm. Unit 2 is a dark gray basalt with spherulites. Subunit 3A is composed of limestone (Cretaceous) with fragments of slightly altered to unaltered glassy basalt.

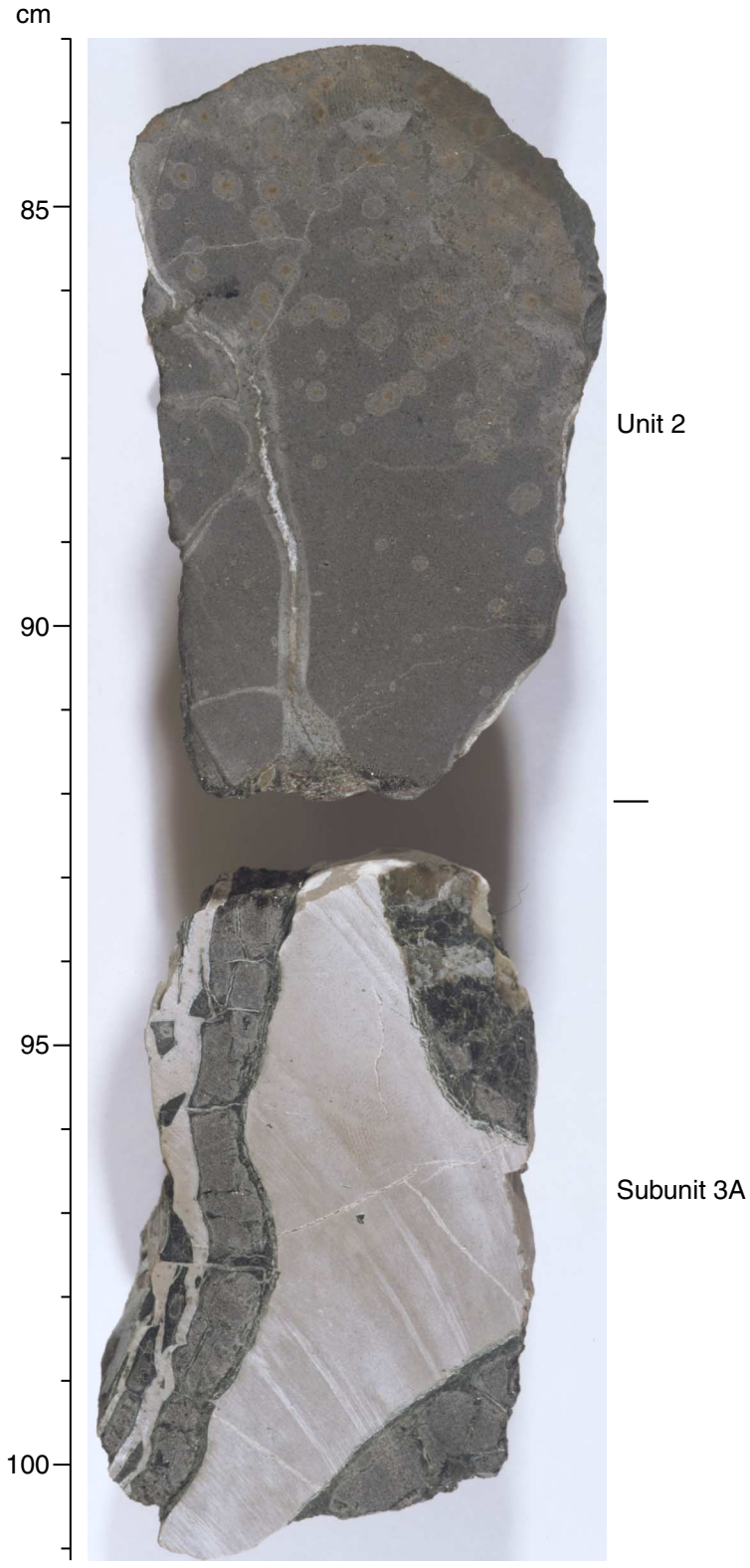

Figure F14. Interval 192-1185B-17R-1, 65–84 cm, showing pink, fine-grained limestone adjacent to fine-grained basalt. The limestone is interpreted as filling a fissure within the upper part of the massive flow of Unit 10.

Figure F15. Altered radiolarians or foraminifers in a matrix of micritic calcite in Sample **192-1185A-10R-1, 38–40 cm** (Cretaceous limestone between basaltic pillows) (field of view = 2.8 mm; plane-polarized light; photomicrograph ID# 1185AS_25). Brownish semiopaque material is common.

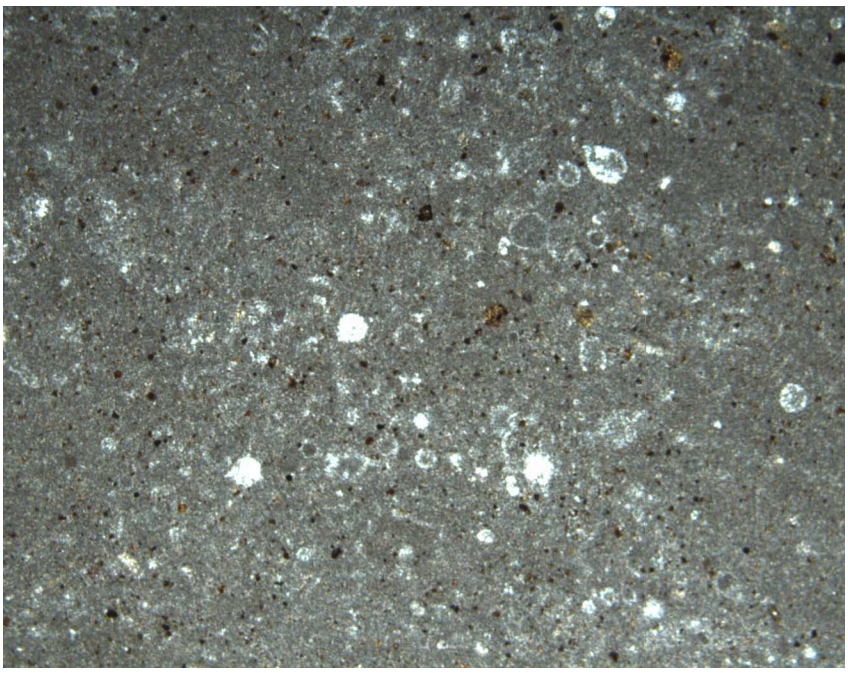

Figure F16. Log of basement cores, recovery, rock types, and lithologic units at Site 1185.

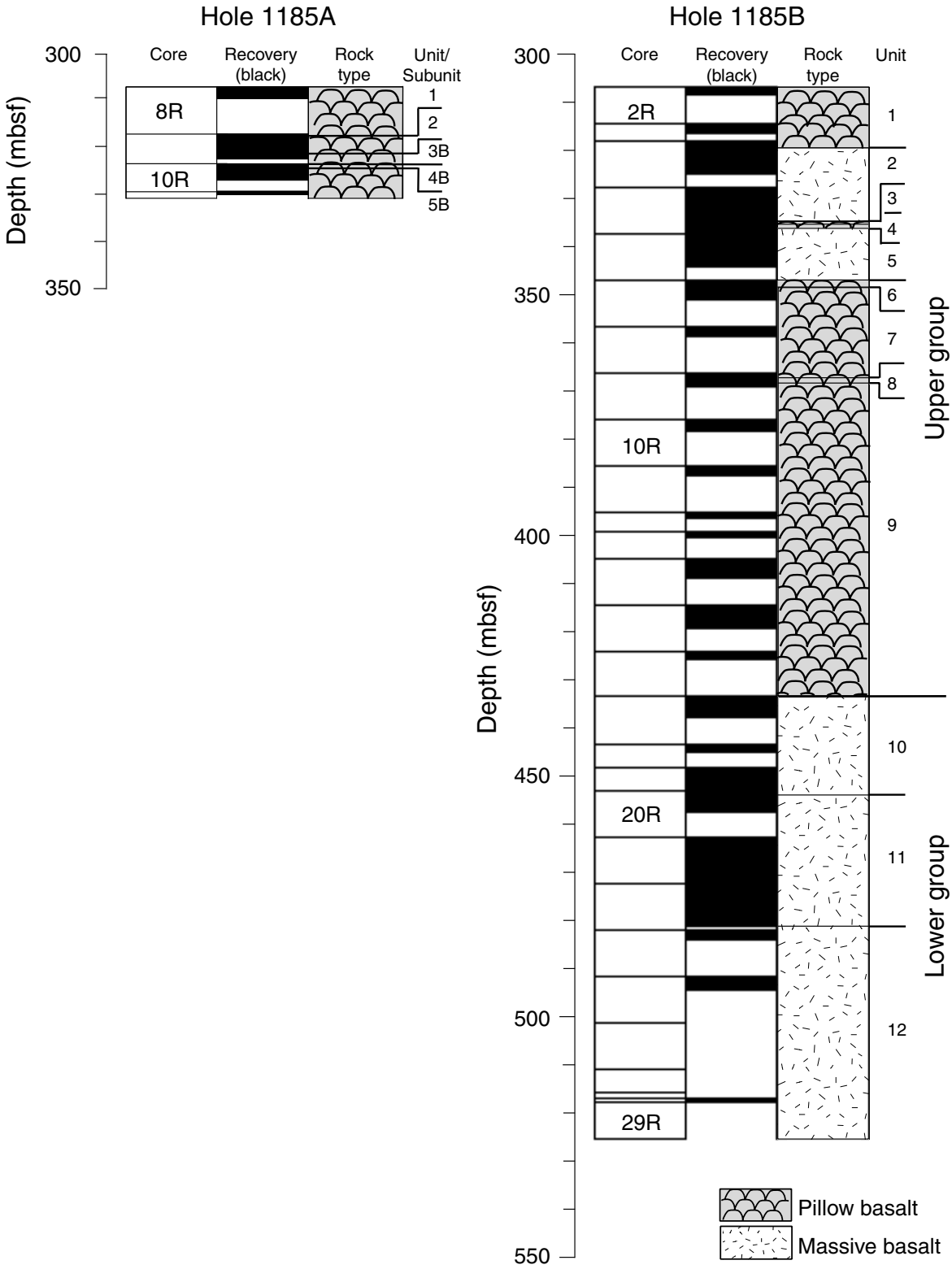

Figure F17. Interval 192-1185A-9R-1, 126–150 cm, showing curved glassy margin (dashed line) of pillow basalt with spherulites in the pillow interior. Beneath this, calcite-cemented hyaloclastite forms the uppermost part of Unit 2.

Figure F18. Interval 192-1185B-5R-6, 100–130 cm, showing the transition from the massive basalt of Unit 2 to the pillowed top of Unit 3 at 114 cm; Unit 3 pillows have altered glassy rims and spherulitic interiors.

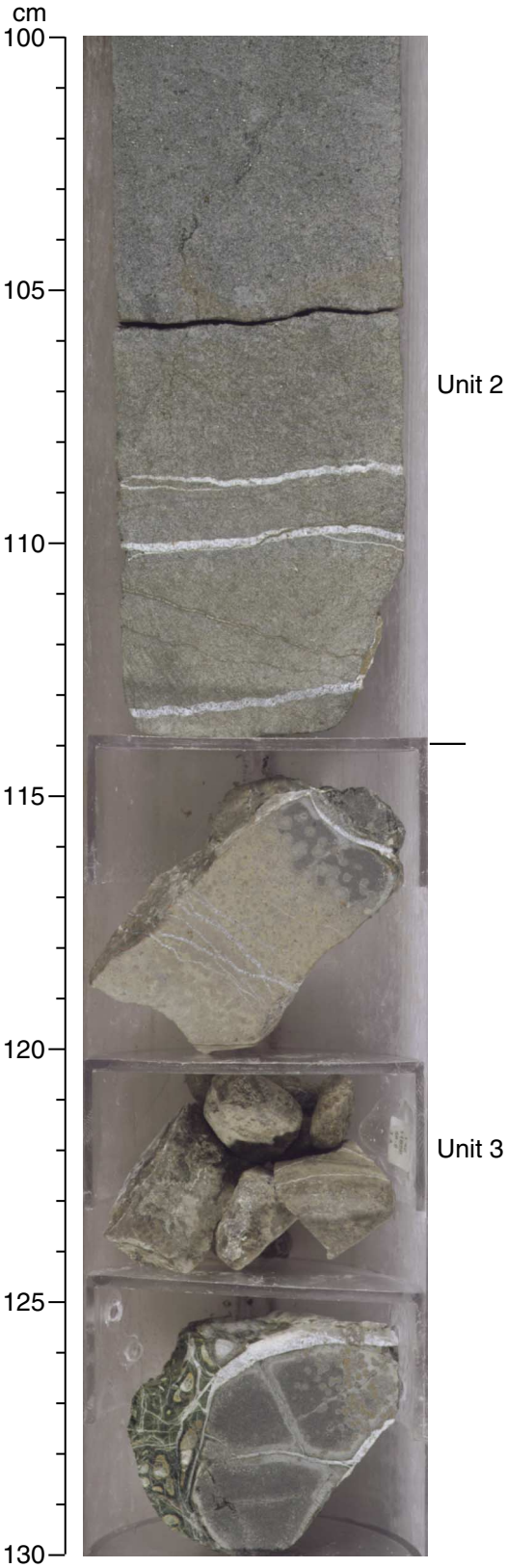

Figure F19. Interval 192-1185B-22R-7, 71–82 cm, showing Unit 11 in contact with Unit 12. A chilled margin is visible along the edges of the aphanitic Unit 11 basalt. The contact is subvertical, suggesting that the base of Unit 11 is filling a fissure in the surface of Unit 12.

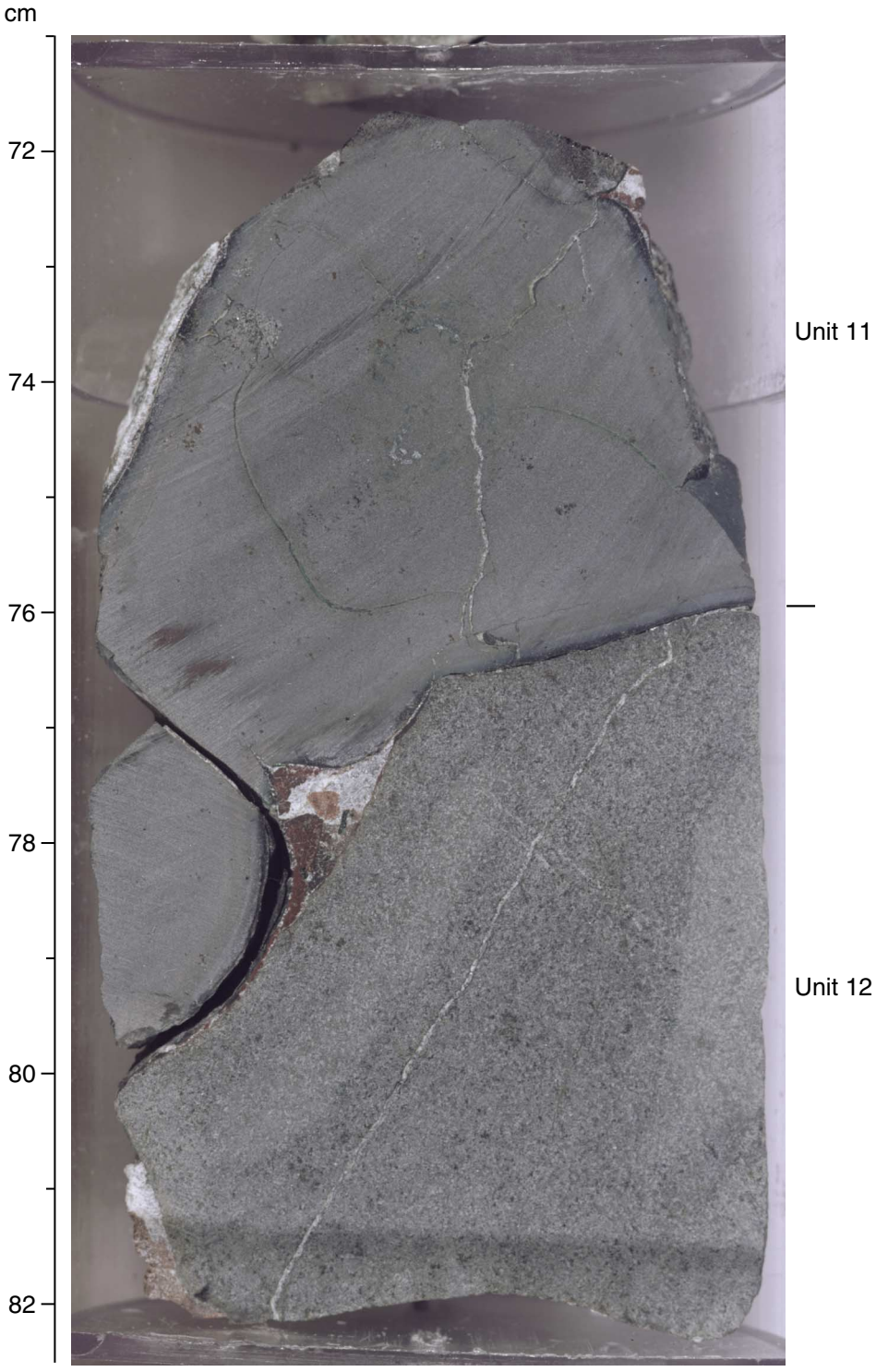

Figure F20. Interval 192-1185B-3R-1, 54–63 cm, showing spherulites (highlighted by Fe oxyhydroxide alteration) in aphanitic, dark gray basalt pillow margin in Unit 1. Completely altered olivine phenocrysts are visible at the centers of the spherulites. Black glass is present (lower right).

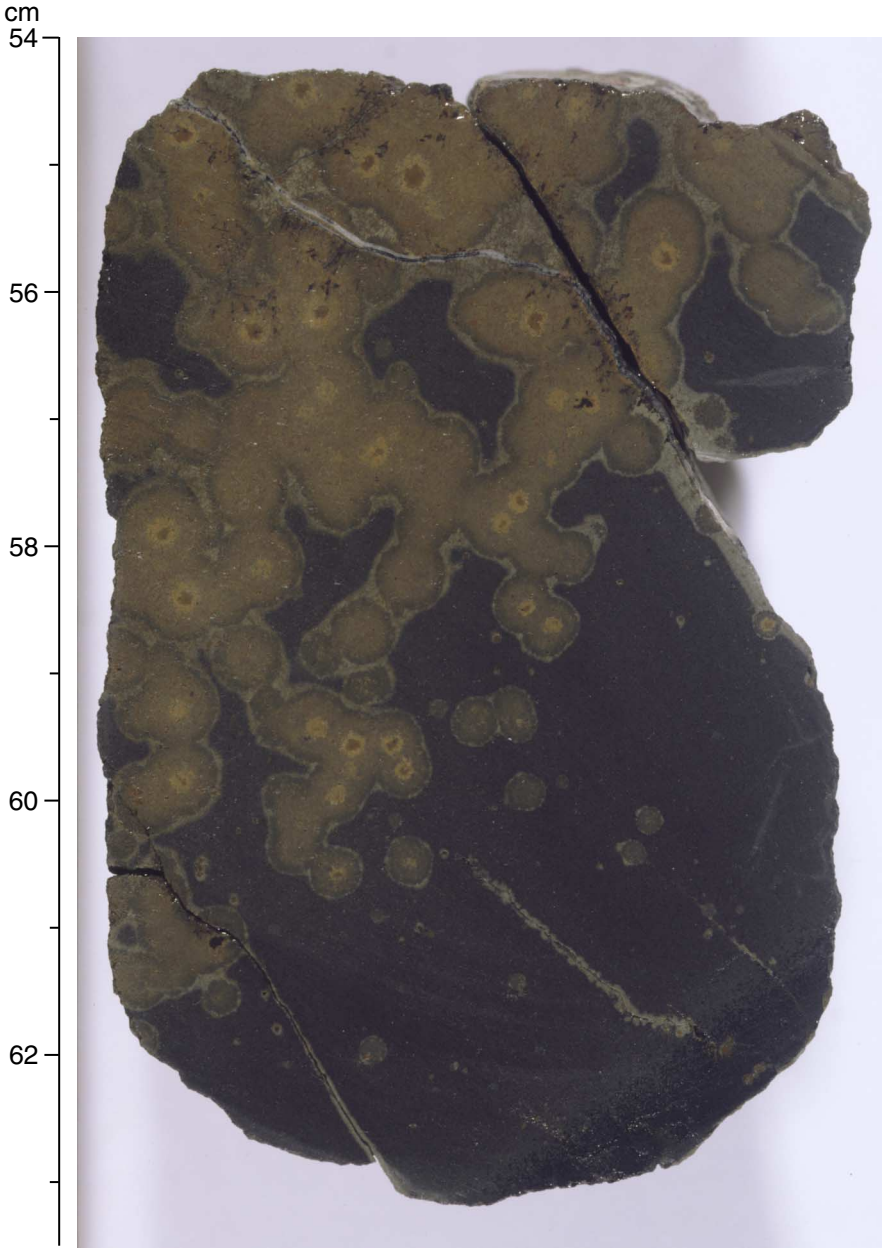

Figure F21. Interval 192-1185B-3R-2, 33–54 cm, showing pervasively altered spherulitic basalt near a pillow margin with light and dark yellow-brown colors. Completely altered olivine phenocrysts are visible at the centers of most of the spherulites. Spherulites are highlighted by Fe oxyhydroxide alteration; the extent of alteration increases away from the pillow margin. The black aphanitic margin of the pillow is visible (bottom left).

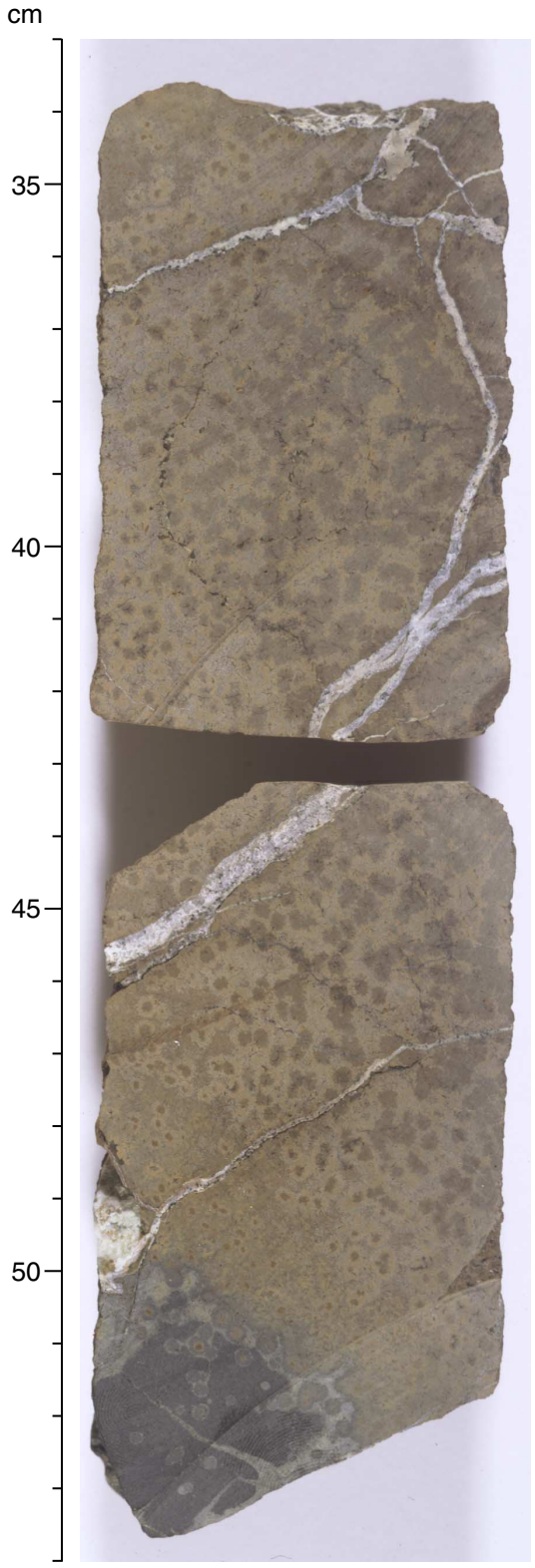

Figure F22. Interval 192-1185B-5R-7, 55–85 cm, showing the boundary between Units 3 and 4 at 67.5 cm, defined by the presence of altered hyaloclastite. Both units consist of altered basalt with abundant yellowish brown spherulites.

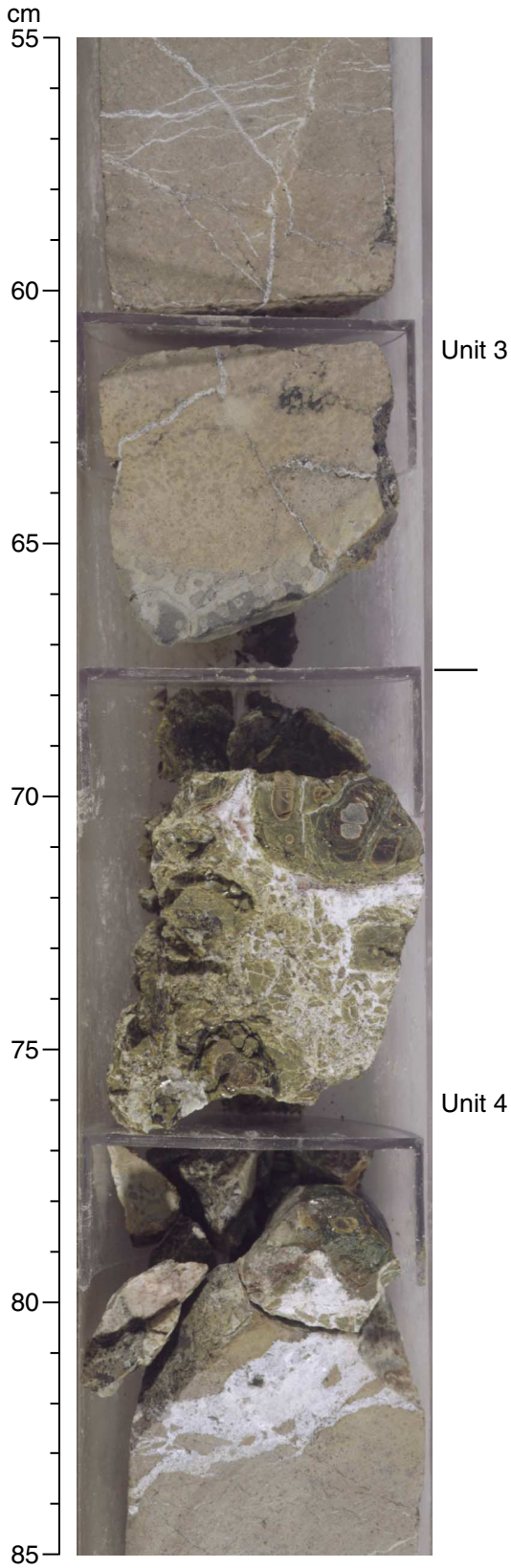

Figure F23. Interval 192-1185B-20R-1, 92–110 cm, showing the typical fine-grained basalt texture in Unit 11.

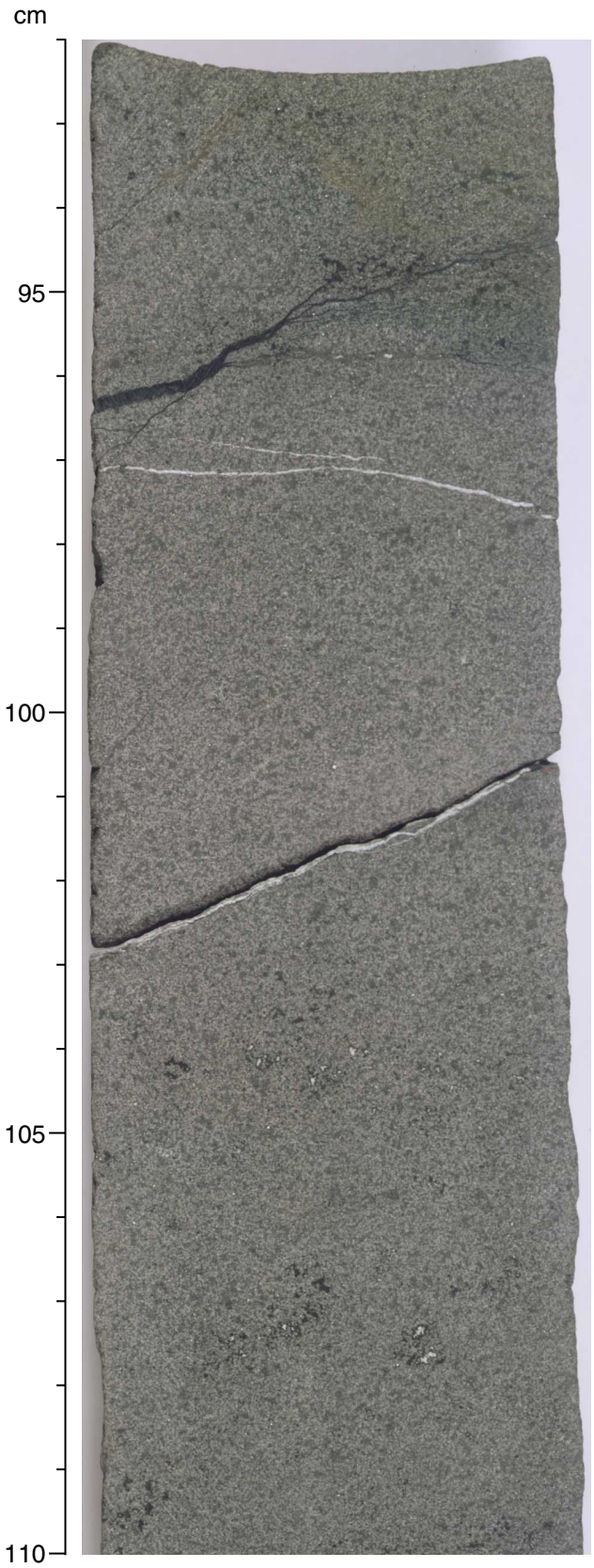

Figure F24. Interval 192-1185B-22R-6, 77–87 cm, showing an irregularly shaped, coarser grained patch in an otherwise aphanitic to fine-grained basalt (Unit 11).

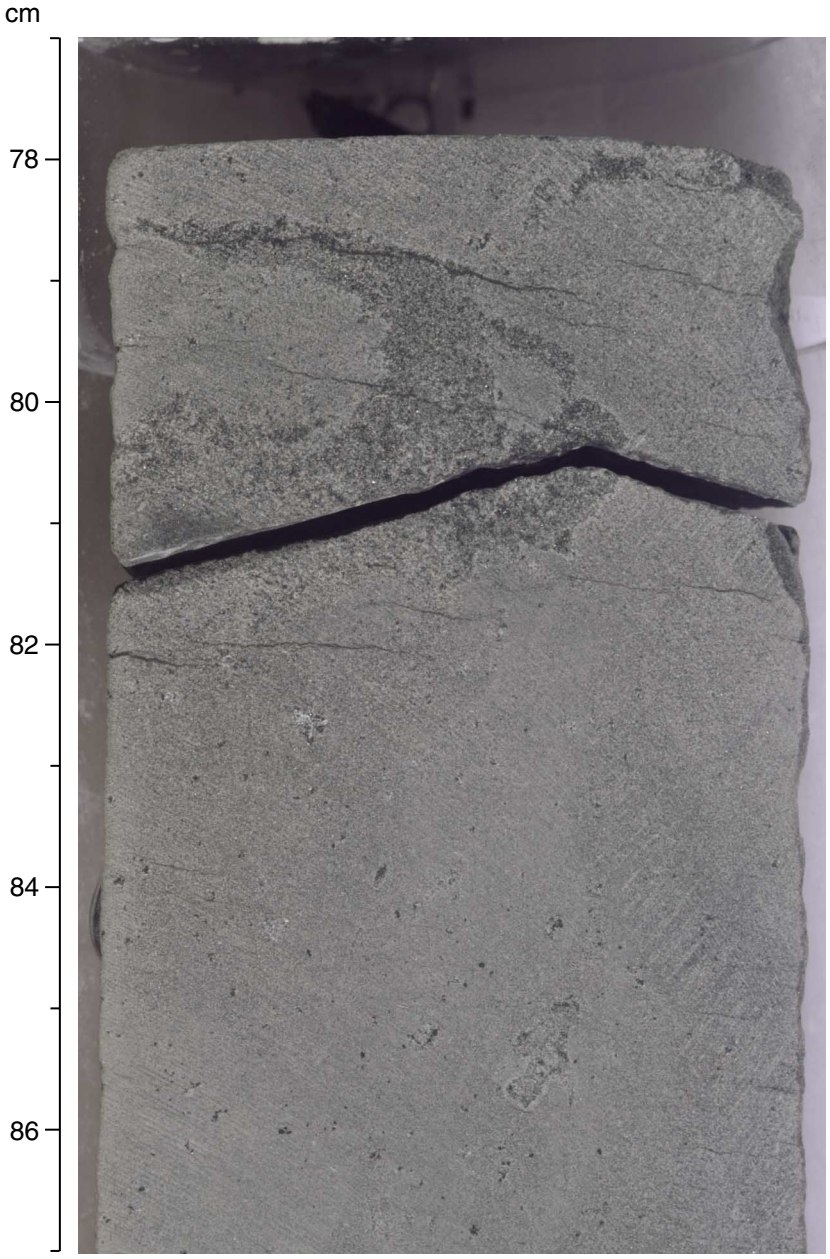

Figure F25. Downhole variation in Hole 1185B in the amounts of phenocrysts, unaltered glass, and xenoliths (including plagioclase xenocrysts and xenoliths consisting mainly of aggregates of plagioclase crystals). The increase of plagioclase and presence of clinopyroxene phenocrysts in Units 10–12 coincide with the occurrence of variolitic to subophitic patches that are coarser grained than the aphanitic to fine-grained groundmass. Thus, some of the clinopyroxene and plagioclase "phenocrysts" may simply be crystals disaggregated from these patches.

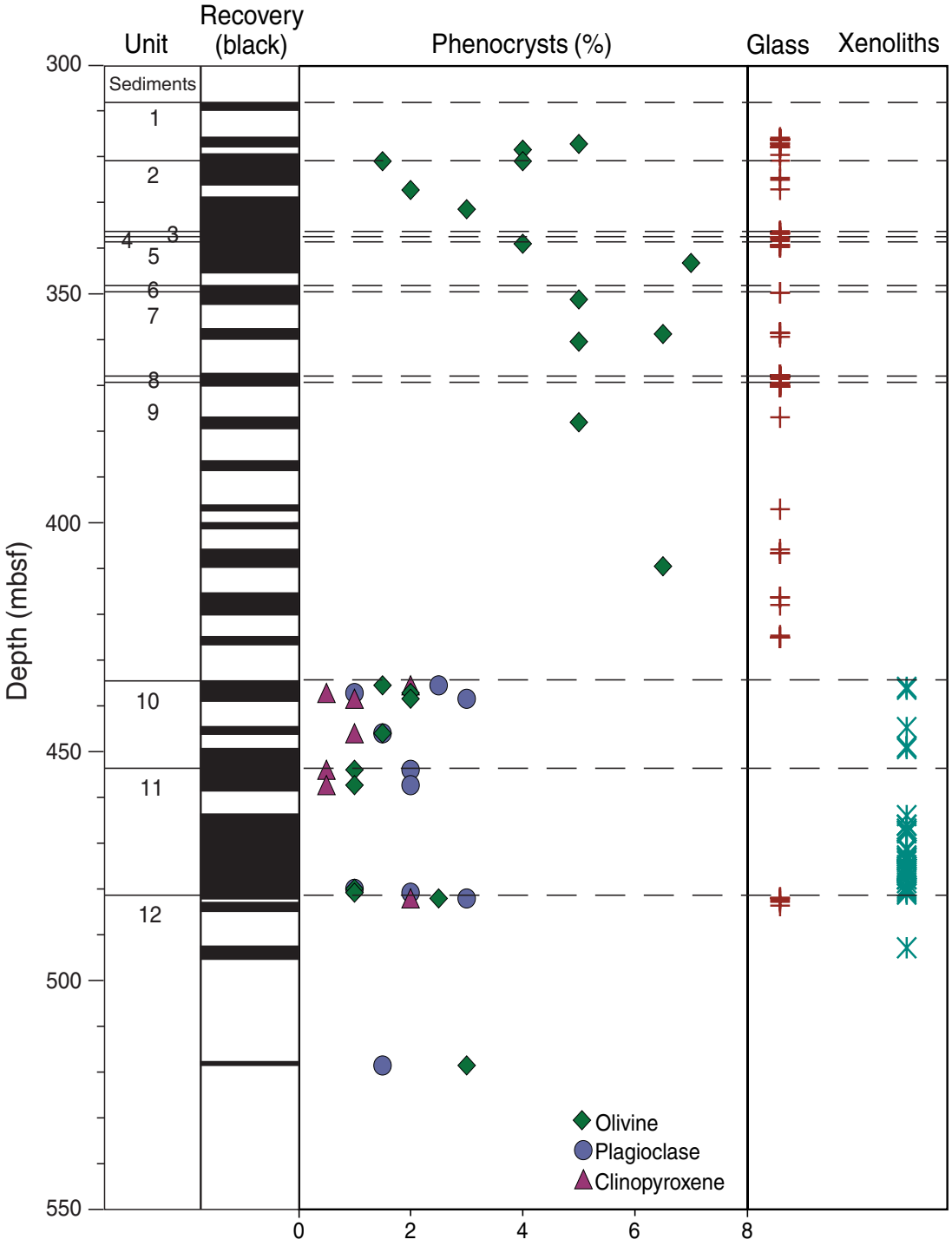

Figure F26. Elongate vesicle trains and unaltered pillow-rim glass with altered (right center) and unaltered (upper left) olivine phenocrysts in Sample **192-1185A-10R-1 (Piece 6, 38–40 cm),** Unit 5A. Chrome spinel crystals are present as inclusions in the olivine phenocrysts (field of view = 1.4 mm; plane-polarized light; photomicrograph ID# 1185A_137).

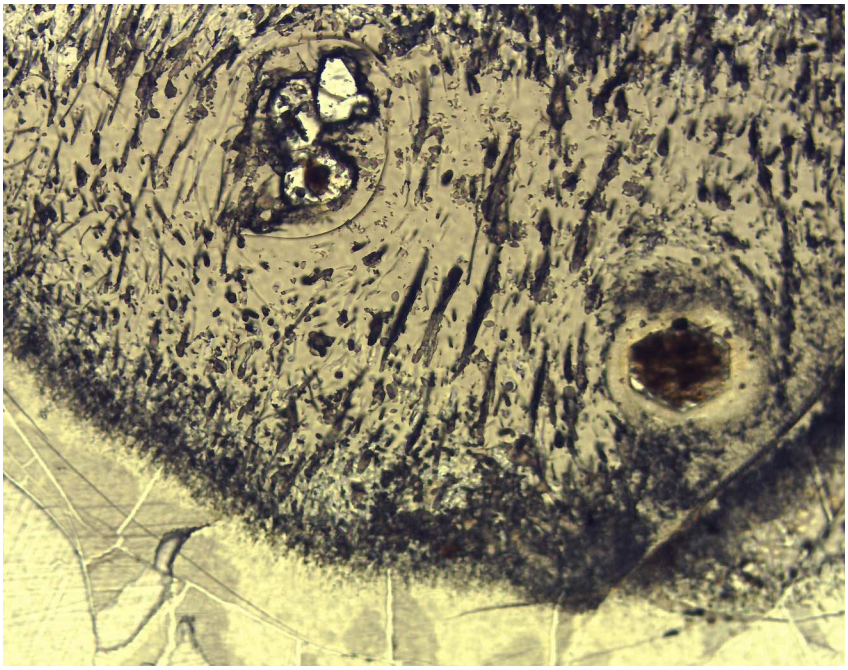

Figure F27. Texture typical of the pillow interiors in Sample 192-1185A-10R-3 (Piece 1B, 51–54 cm), Unit 5B. Olivine phenocrysts (highlighted) are altered to greenish brown clay (field of view = 5.5 mm; plane-polarized light; photomicrograph ID# 1185A_132).

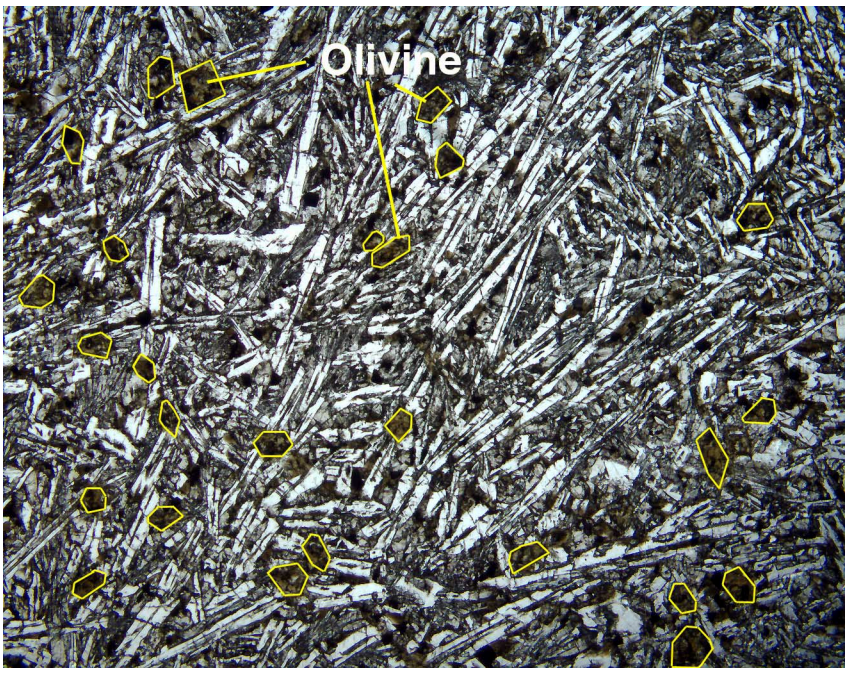

Figure F28. A plagioclase phenocryst exhibiting oscillatory zoning in **Sample 192-1185B-20R-3 (Piece 3B, 66–68 cm),** Unit 11 (field of view = 0.7 mm; crossed polars; photomicrograph ID# 1185B_170).

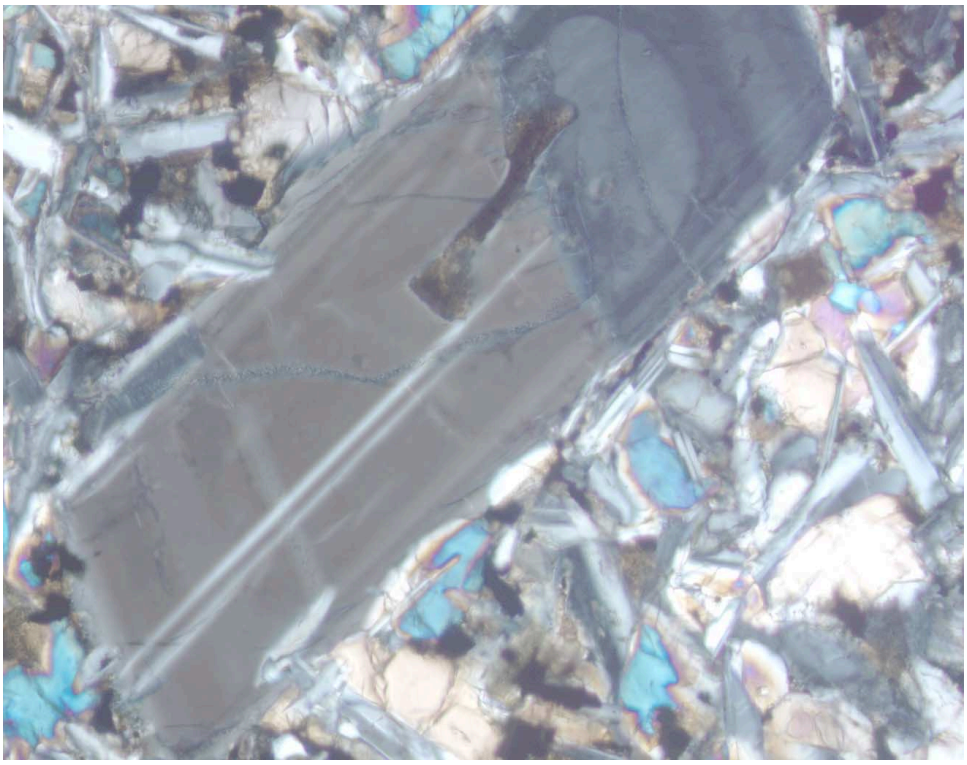

Figure F29. Olivine phenocrysts in glass in Sample **192-1185B-3R-1 (Piece 16, 94–97 cm)**, Unit 1. Two phenocrysts have inclusions of chrome spinel (field of view = 0.7 mm; crossed polars; photomicrograph ID# 1185B_176).

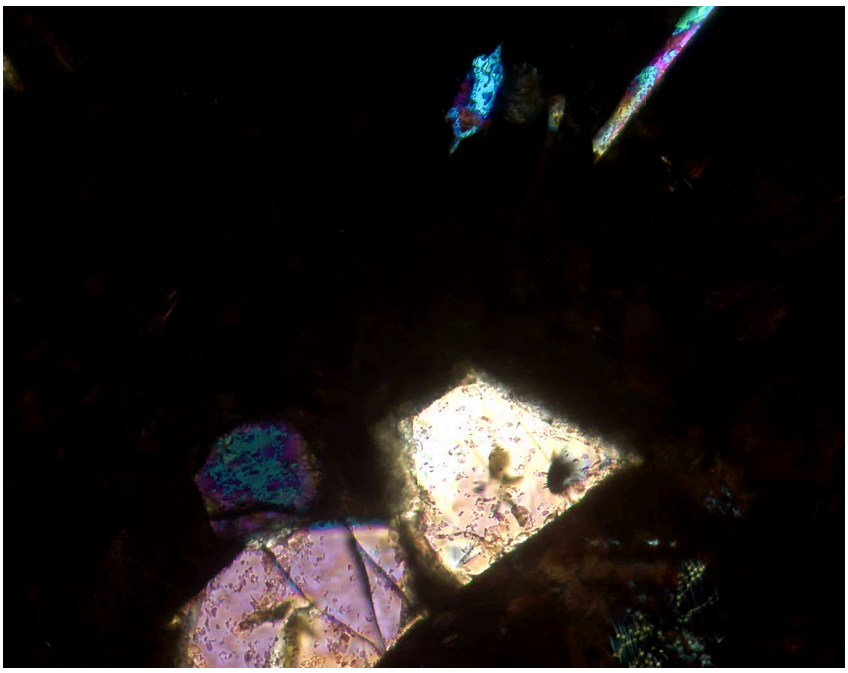

Figure F30. Olivine, plagioclase, and clinopyroxene phenocrysts in Sample 192-1185B-22R-7 (Piece 2, 42–43 cm), Unit 12. Olivine phenocrysts are completely replaced by green smectite. Clinopyroxene phenocrysts are surrounded by radiating fibers of elongate clinopyroxene (field of view = 1.4 mm; plane-polarized light; photomicrograph ID# 1185B_185).

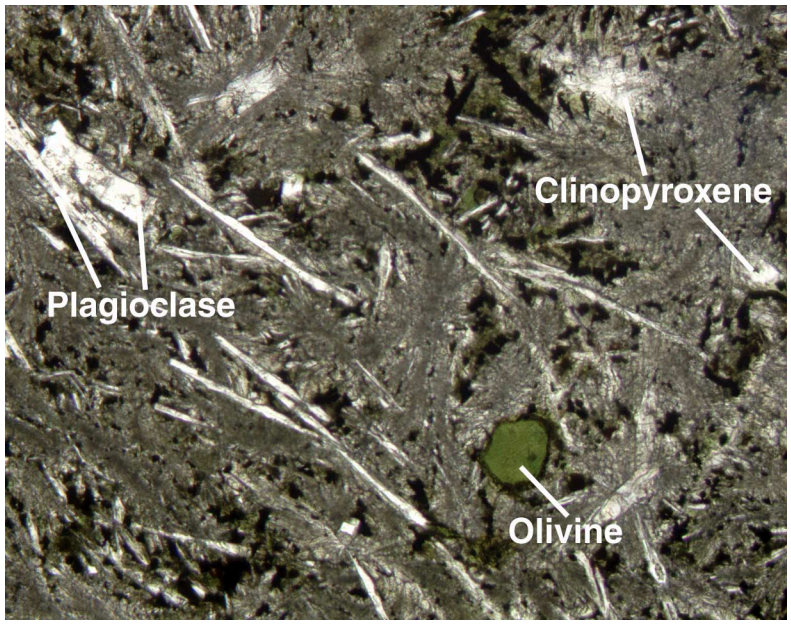

Figure F31. Unaltered interiors of olivine phenocrysts (small equant crystals [center]) at the center of a variole defined by radiating, skeletal plagioclase laths in Sample **192-1185A-11R-1 (Piece 4B, 83–86 cm),** Unit 5B (field of view = 2.8 mm; plane-polarized light; photomicrograph ID# 1185A_141).

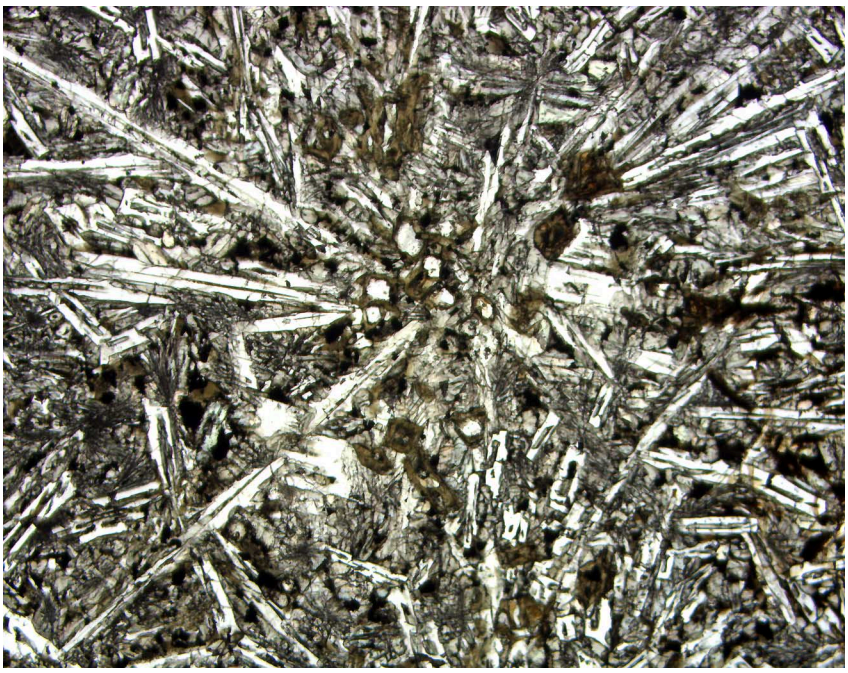

Figure F32. Chrome spinel crystals attached to (bottom center) and included in (right center) euhedral olivine phenocrysts in Sample **192-1185A-8R-1 (Piece 2, 15–18 cm),** Unit 1 (field of view = 0.28 mm; plane-polarized light; photomicrograph ID# 1185A_118).

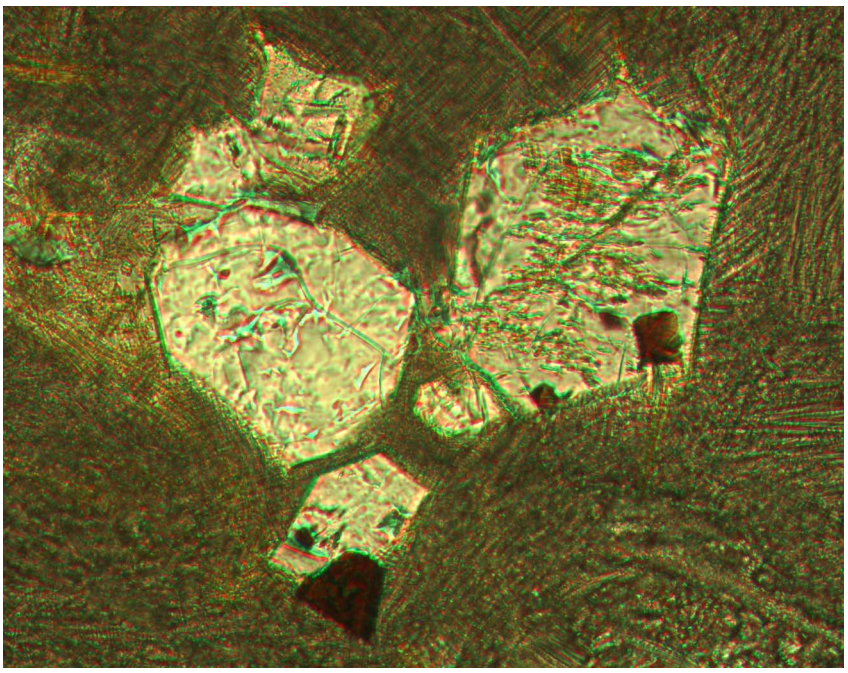

Figure F33. A euhedral chrome spinel crystal in a groundmass of dendritic crystals and devitrified glass in Sample **192-1185A-8R-1 (Piece 2, 15–18 cm)**, Unit 1 (field of view = 0.28 mm; plane-polarized light; photomicrograph ID# 1185A_119).

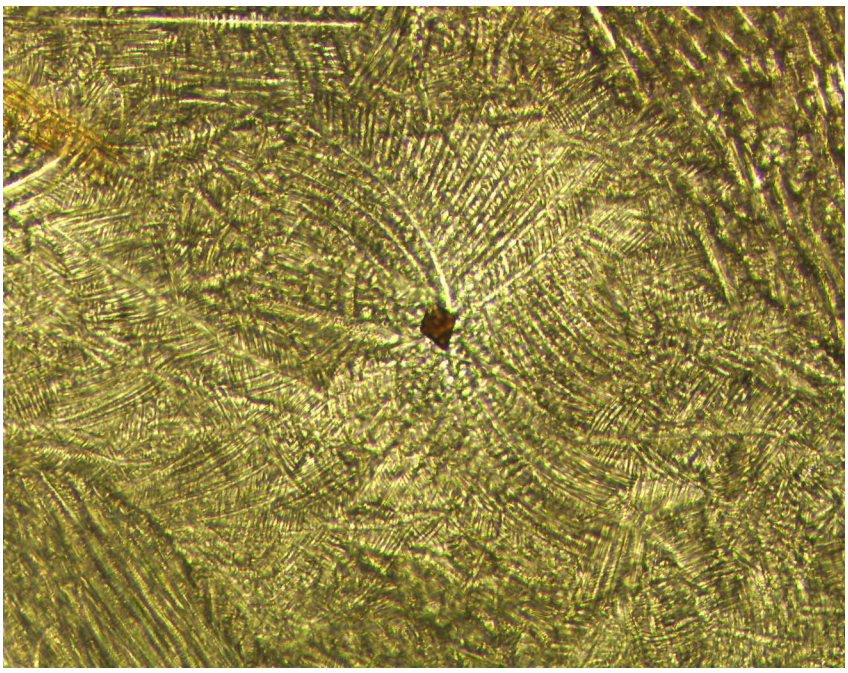

Figure F34. A single, euhedral chrome spinel crystal (highlighted) in a dendritic groundmass in Sample 192-1185A-8R-1 (Piece 2, 15–18 cm), Unit 1 (field of view = 0.28 mm; crossed polars; photomicrograph ID# 1185A_123B).

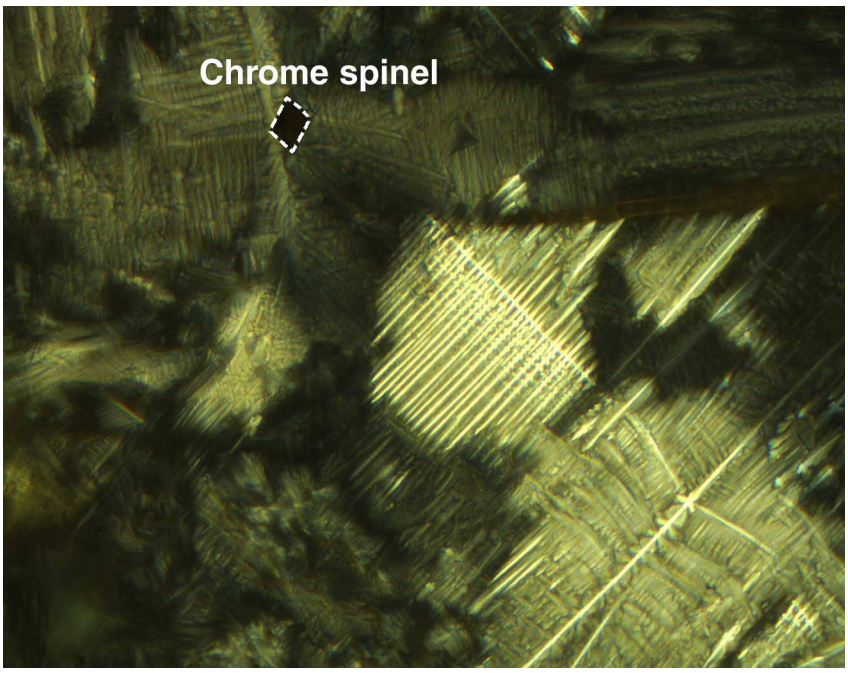

Figure F35. Plagioclase and clinopyroxene phenocrysts in Sample 192-1185B-20R-3 (Piece 3B, 66–68 cm), Unit 11 (field of view = 1.4 mm; crossed polars; photomicrograph ID# 1185B_160).

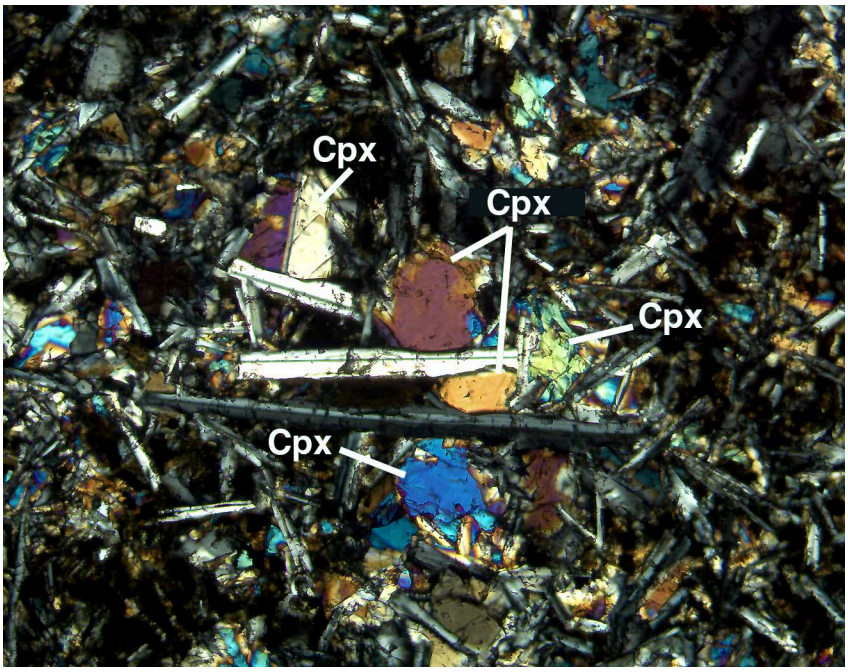

Figure F36. Euhedral olivine phenocrysts and small, euhedral chrome spinel crystals with skeletal groundmass olivine (elongate brown crystals) in Sample **192-1185A-8R-1 (Piece 2, 15–18 cm),** Unit 1. One of the olivine crystals is unaltered (middle left). The remaining groundmass is cryptocrystalline but contains smaller, skeletal olivine crystals just visible in this view (field of view = 1.4 mm; crossed polars; photomicrograph ID# 1185A_121).

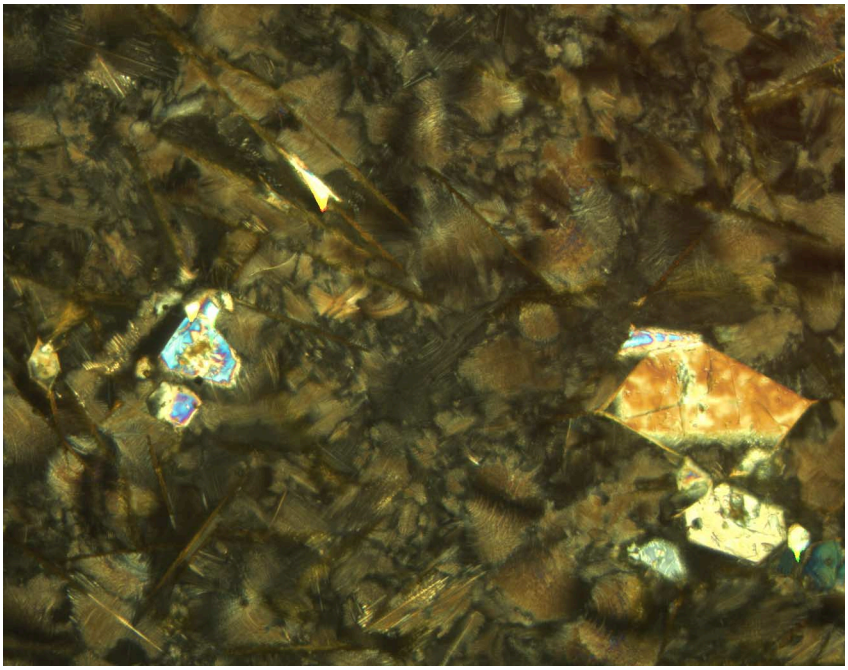

Figure F37. Unaltered olivine phenocrysts in an aphanitic groundmass and an altered spherulite with altered olivine phenocrysts at its center in Sample **192-1185A-10R-2 (Piece 1A, 3–6 cm),** Unit 5B (field of view = 2.8 mm; crossed polars; photomicrograph ID# 1185A_139).

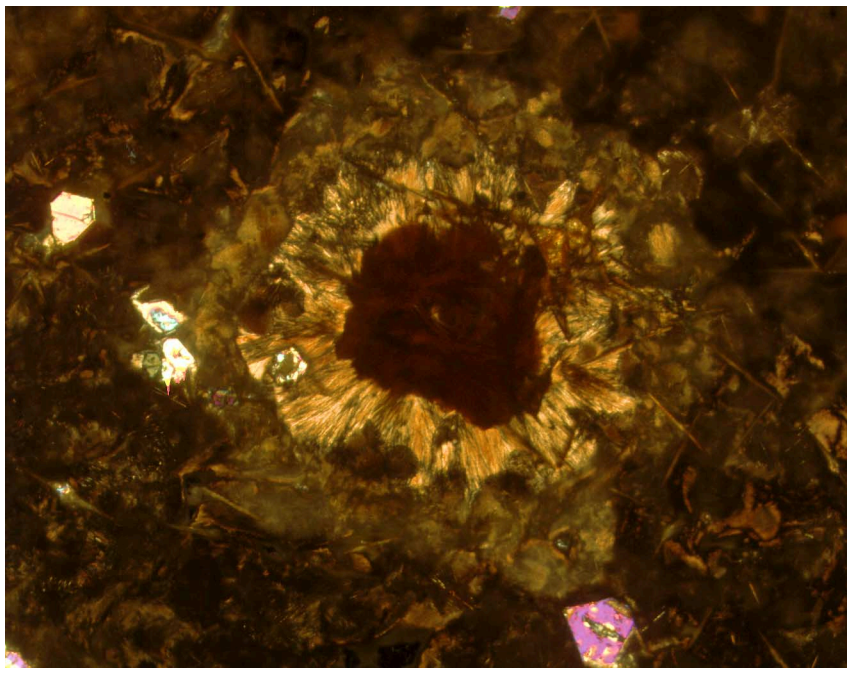

Figure F38. A completely altered area in Sample **192-1185A-10R-2 (Piece 1A, 3–6 cm),** Unit 5B. The alteration highlights the elongate and rarely dendritic groundmass olivine and its relationship with the olivine phenocrysts (middle left) (field of view = 2.8 mm; plane-polarized light; photomicrograph ID# 1185A_138).

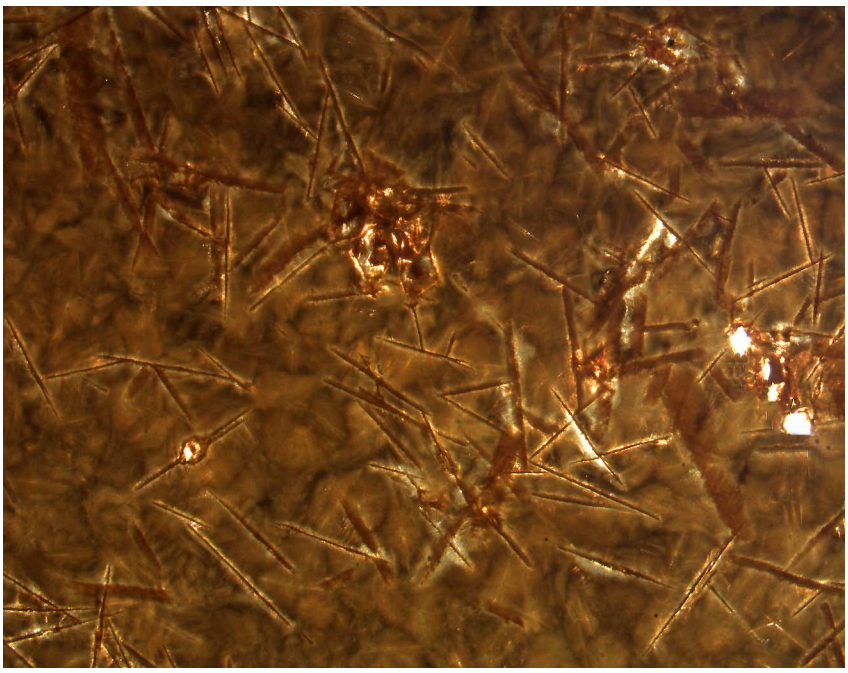

Figure F39. Discrete crystals of chrome spinel (outlined) and titanomagnetite (bright) in Sample 192-1185A-10R-3 (Piece 1B, 51–54 cm), Unit 5B (field of view = 0.28 mm; reflected light; photomicrograph ID# 1185A_130).

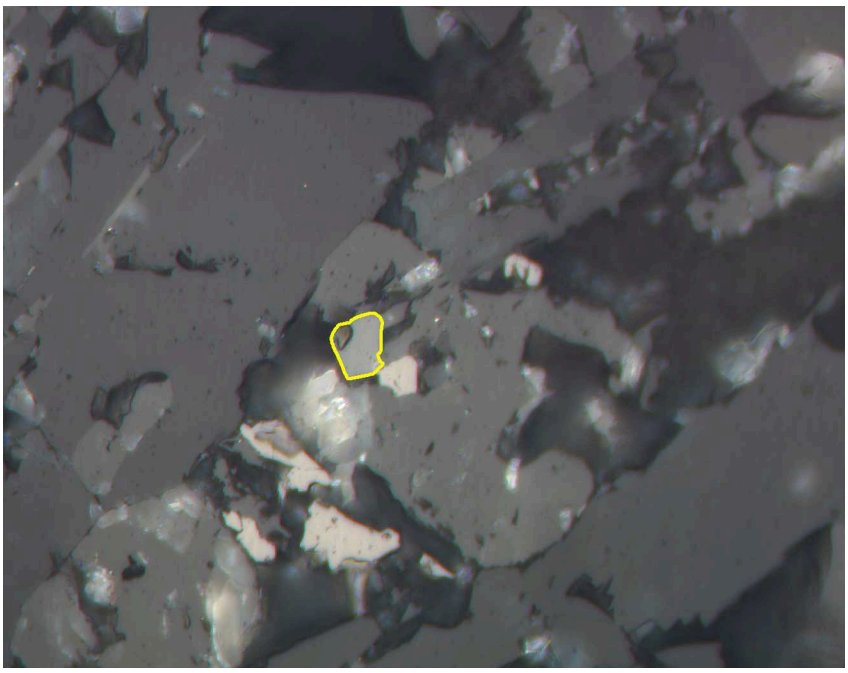

Figure F40. Chrome spinel mantled by titanomagnetite in an altered olivine phenocryst in Sample 192-1185B-4R-7 (Piece 1C, 44–46 cm), Unit 2 (field of view = 0.28 mm; reflected light; photomicrograph ID# 1185B_144).

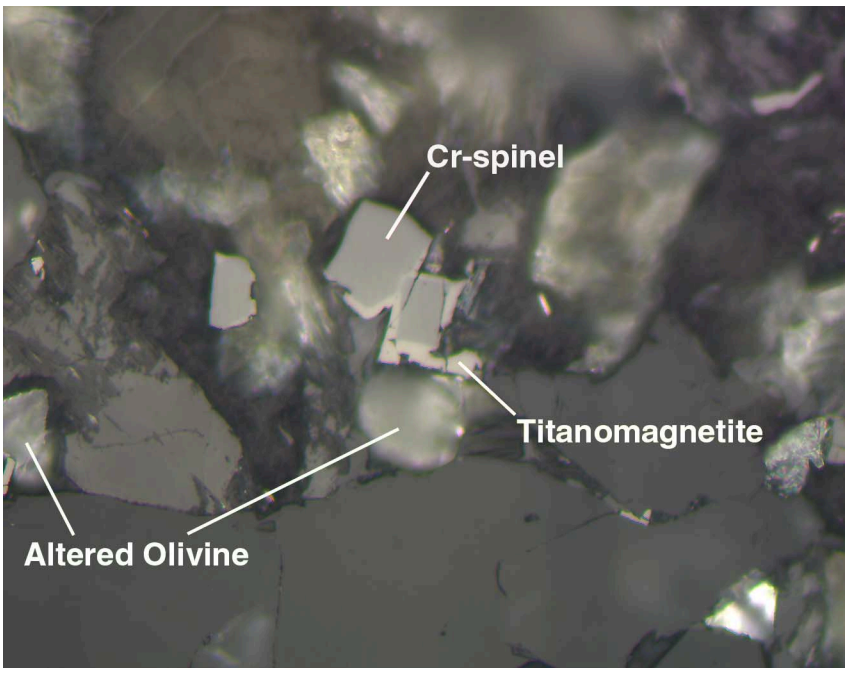

Figure F41. A more coarsely crystalline patch in a fine-grained groundmass in Sample **192-1185B-18R-2 (Piece 3, 17–20 cm),** Unit 10. The patch consists of plagioclase, clinopyroxene, and altered olivine crystals (field of view = 2.8 mm; crossed polars; photomicrograph ID# 1185B_179).

Figure F42. The sharp contact between aphanitic groundmass and a more coarsely crystalline patch in Sample **192-1185B-22R-6 (Piece 6A, 51–54 cm),** Unit 11. The patch consists of olivine, plagioclase, clinopyroxene, and titanomagnetite (field of view = 2.8 mm; plane-polarized light; photomicrograph ID# 1185B_164).

Figure F43. Total alkalies vs. silica diagram showing data for Leg 192 basalt and volcaniclastic rocks. Data for the basalts plot in the tholeiitic basalt field, below the dashed line that separates Hawaiian tholeiitic basalts from Hawaiian alkalic basalts (Macdonald and Katsura, 1964). Fields of different rock types are from Le Bas et al. (1986).

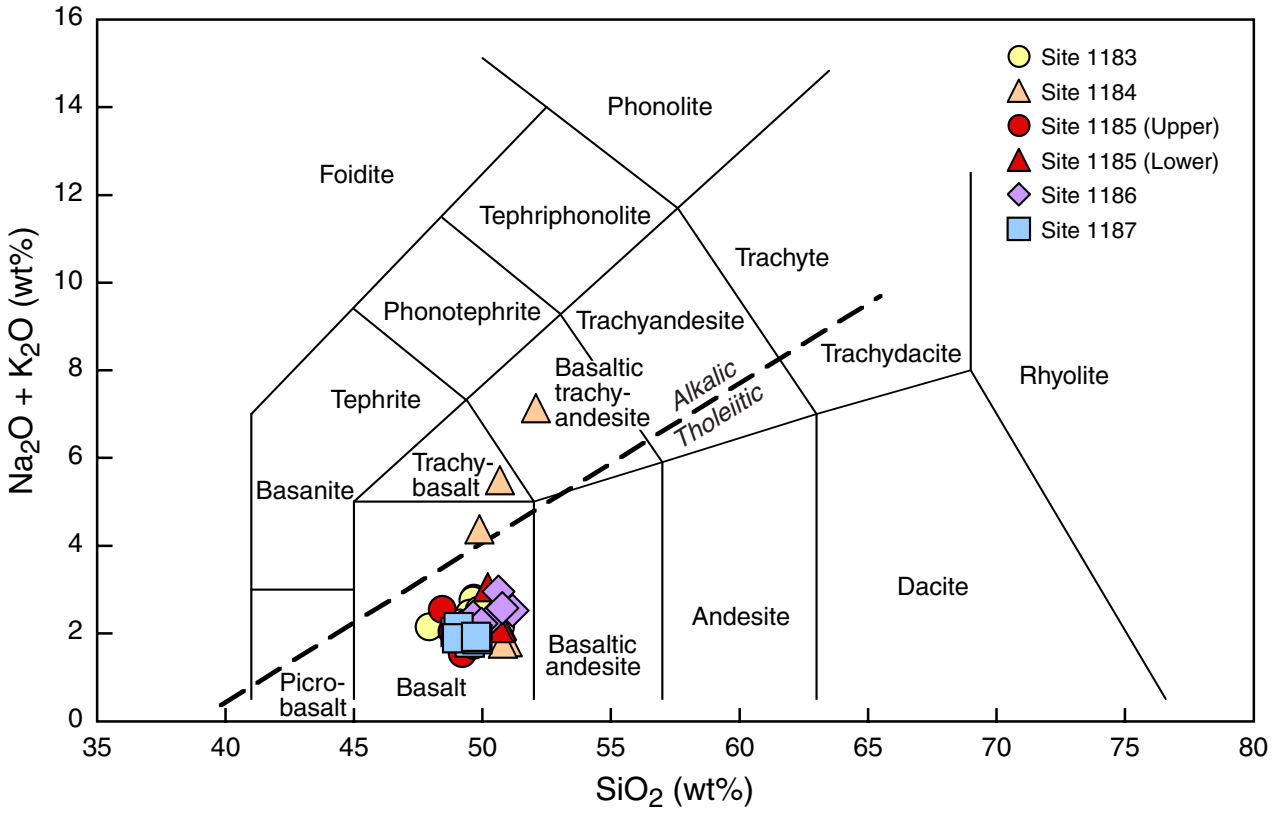

Figure F44. Zr vs. TiO_2 for Leg 192 basalt and volcaniclastic rocks. Note the clear separation of basalts from Hole 1185A and Units 1–9 of Hole 1185B (upper group) from Units 10–12 of Hole 1185B (lower group). Data for Units 10–12 plot in the field for the Kwaimbaita Formation of Malaita, as do data for Sites 1183, 1186, and 807 (Units C–G) and most of the Site 1184 volcaniclastic rocks. Fields for Malaita basalts are from Tejada et al. (in press); data for Sites 803 and 807 are from Mahoney et al. (1993).

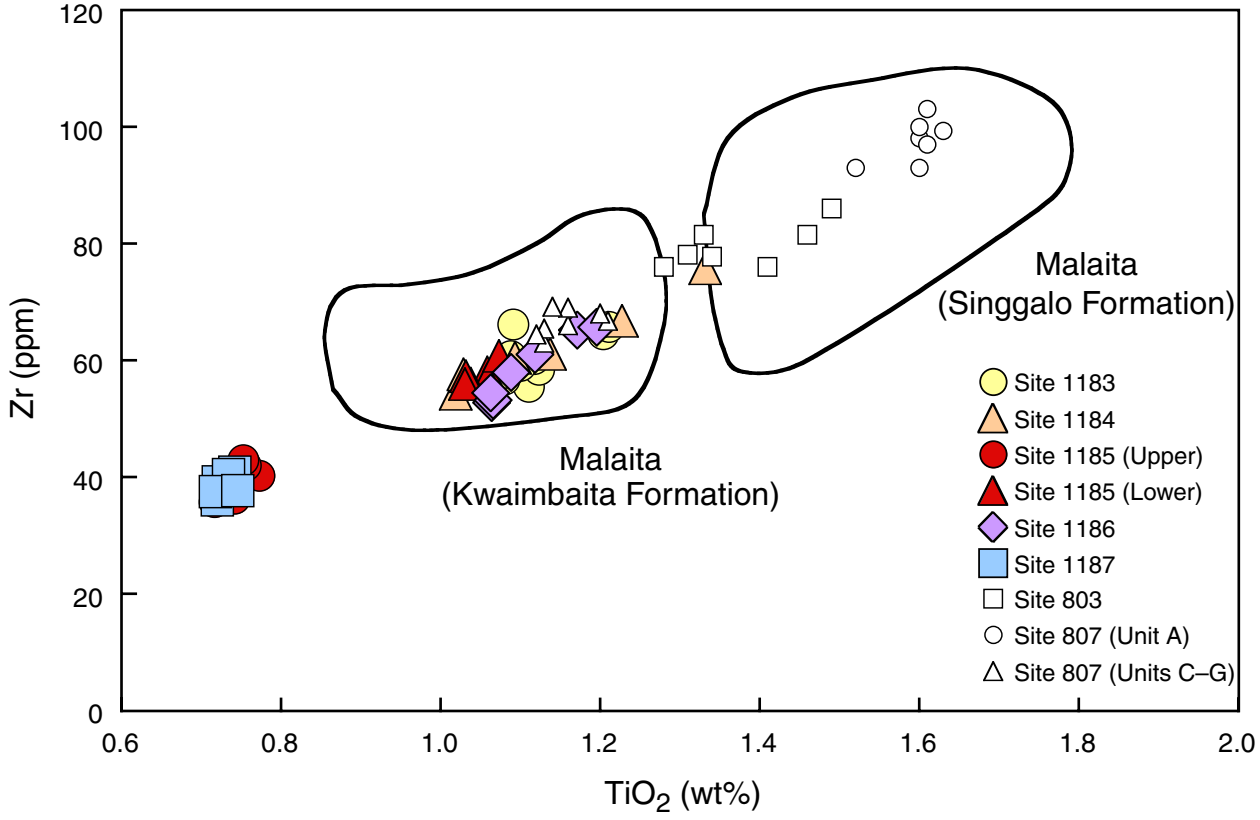

Figure F45. Cr vs. TiO_2 for Leg 192 basalt and volcaniclastic rocks. Basalt from Hole 1185A and Units 1–9 of Hole 1185B (upper group) is clearly separated from that of Units 10–12 of Hole 1185B (lower group). The high Cr contents of the upper group indicate a primitive magma composition; data for Units 10–12 of Hole 1185B plot with the field of the Kwaimbaita Formation (Tejada et al., in press), as do data for Sites 1183 and 1186 and some of the volcaniclastic rocks from Site 1184.

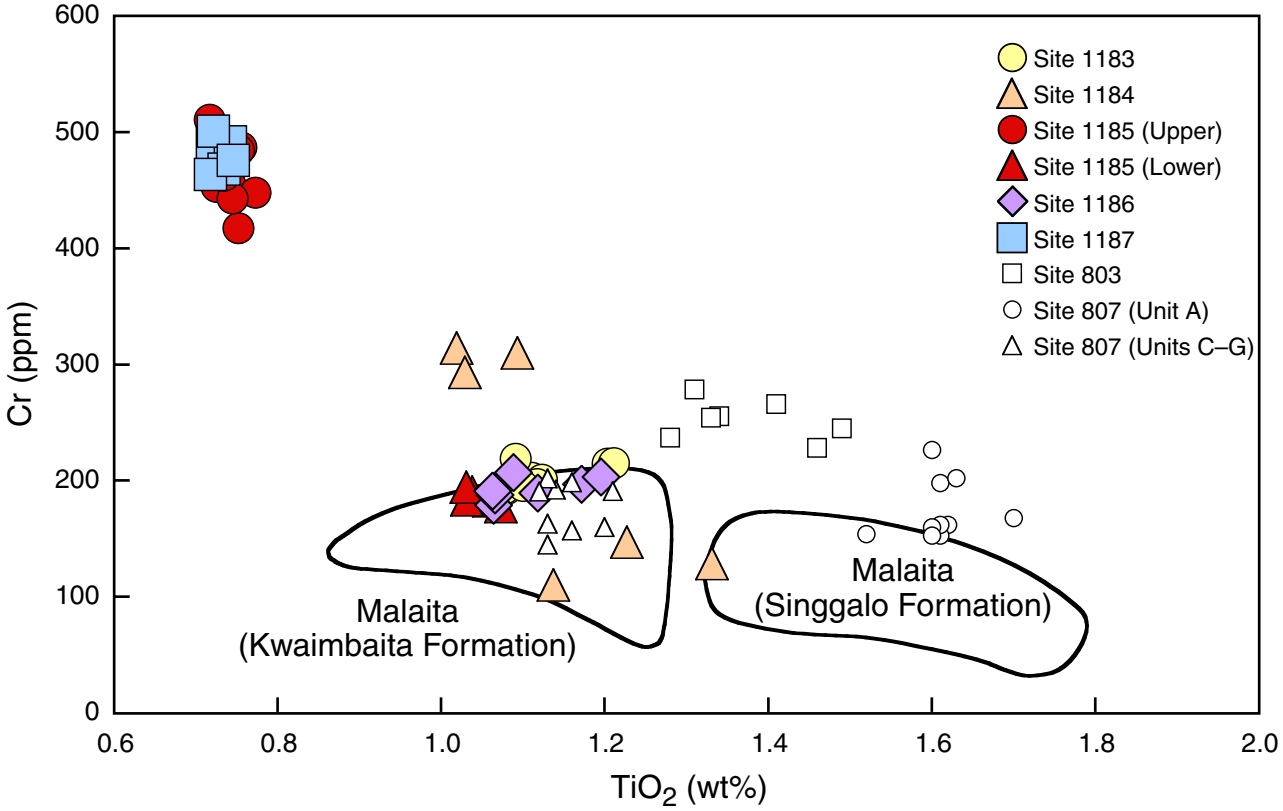

Figure F46. Mg# vs. TiO_2 for Leg 192 basalt and volcaniclastic rocks. The basalt group from Hole 1185A and Units 1–9 of Hole 1185B (upper group) has a rather similar range of Mg# to that of Units 10–12 in Hole 1185B (lower group). However, the lower Mg# of some of the lavas in the lower part of Hole 1185B could be a result of alteration. Mg# is calculated assuming that 12% of the iron is Fe^{3+}, which is equivalent to $Fe_2O_3/(Fe_2O_3 + FeO) = 0.13$, or $Fe_2O_3/FeO = 0.15$.

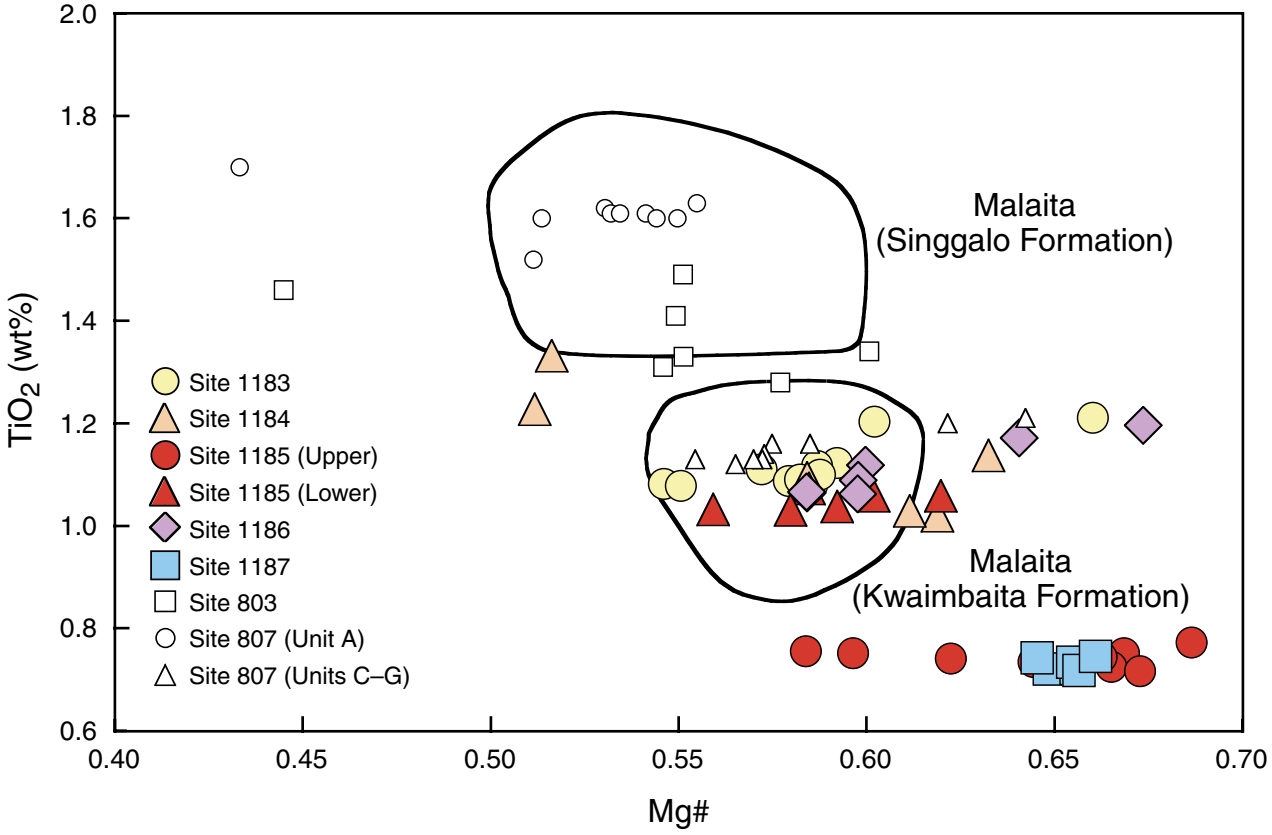

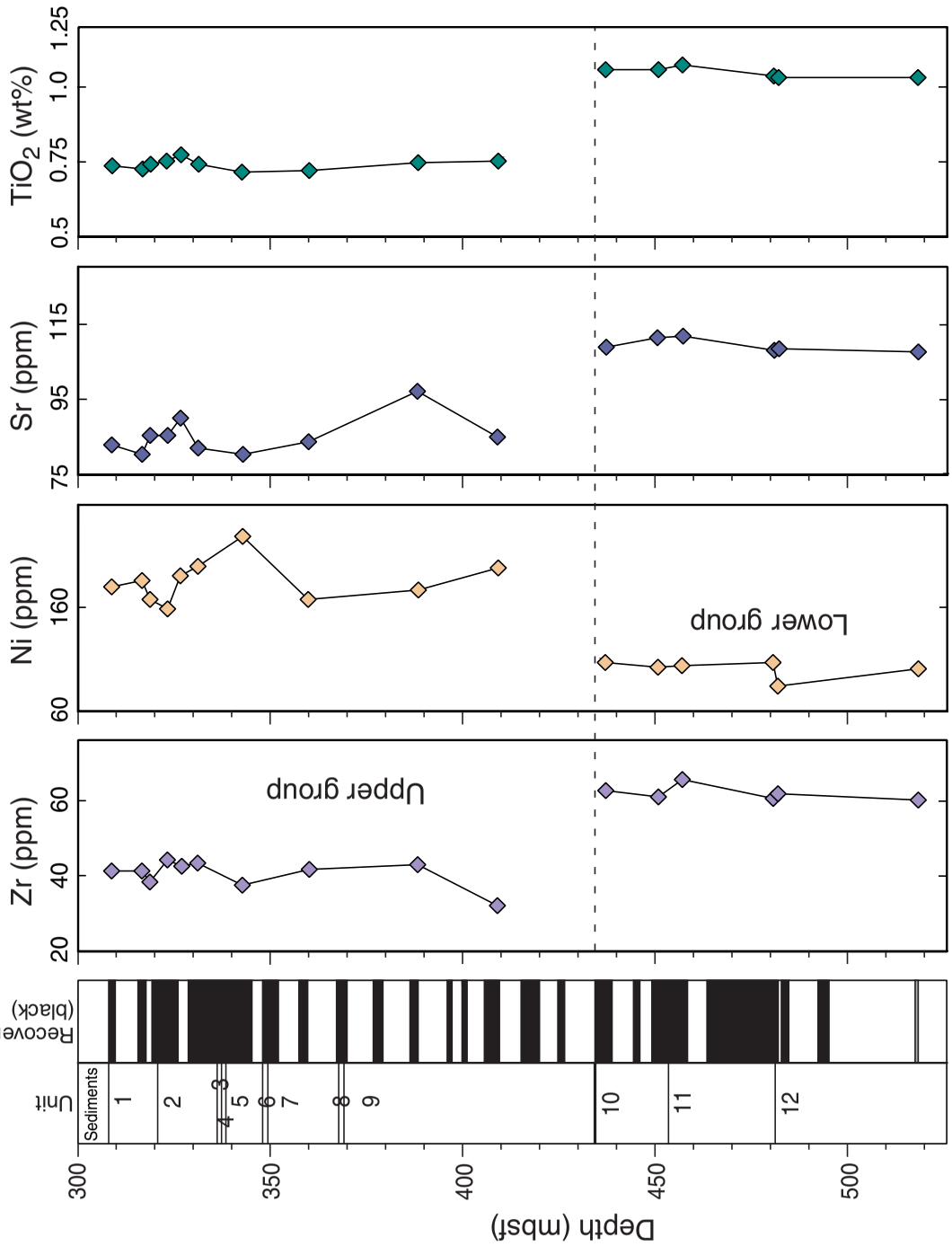

Figure F47. Downhole variation in Zr, Ni, Sr, and TiO_2 for all basalts analyzed from Site 1185. Basalts from Hole 1185A and Units 1–9 of Hole 1185B (upper group) have lower Zr, Sr, and TiO_2 but higher Ni contents than those from Units 10–12 of Hole 1185B (lower group).

Figure F48. Interval 192-1185B-7R-2, 109–130 cm, showing well-developed light and dark yellow-brown alteration in basalt near a pillow margin. A small amount of hyaloclastite (green altered glass fragments cemented by white calcite) is visible at 115 cm.

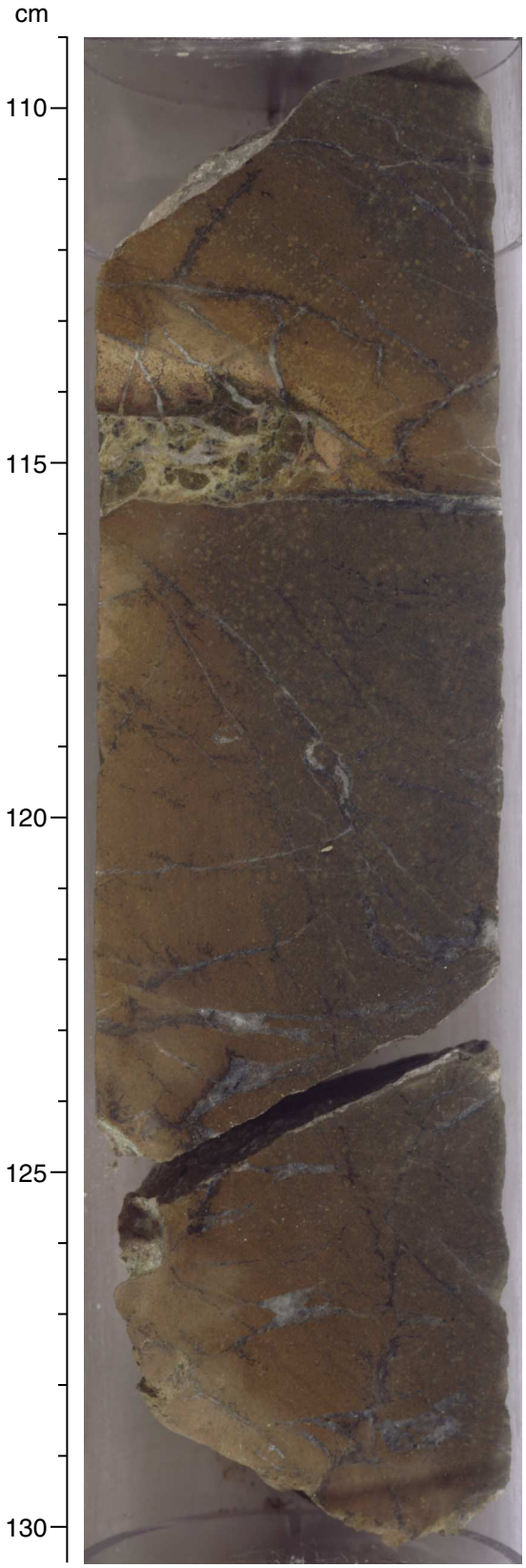

Figure F49. Interval 192-1185B-16R-1, 22–37 cm, showing pervasively altered basalt grading in color from dark yellow-brown (top) to dark brown toward a pillow interior. The sample contains several thin horizontal calcite veins connected by a larger vertical calcite vein. The abundance of crosscutting veins is higher in the more heavily altered dark yellow-brown portion.

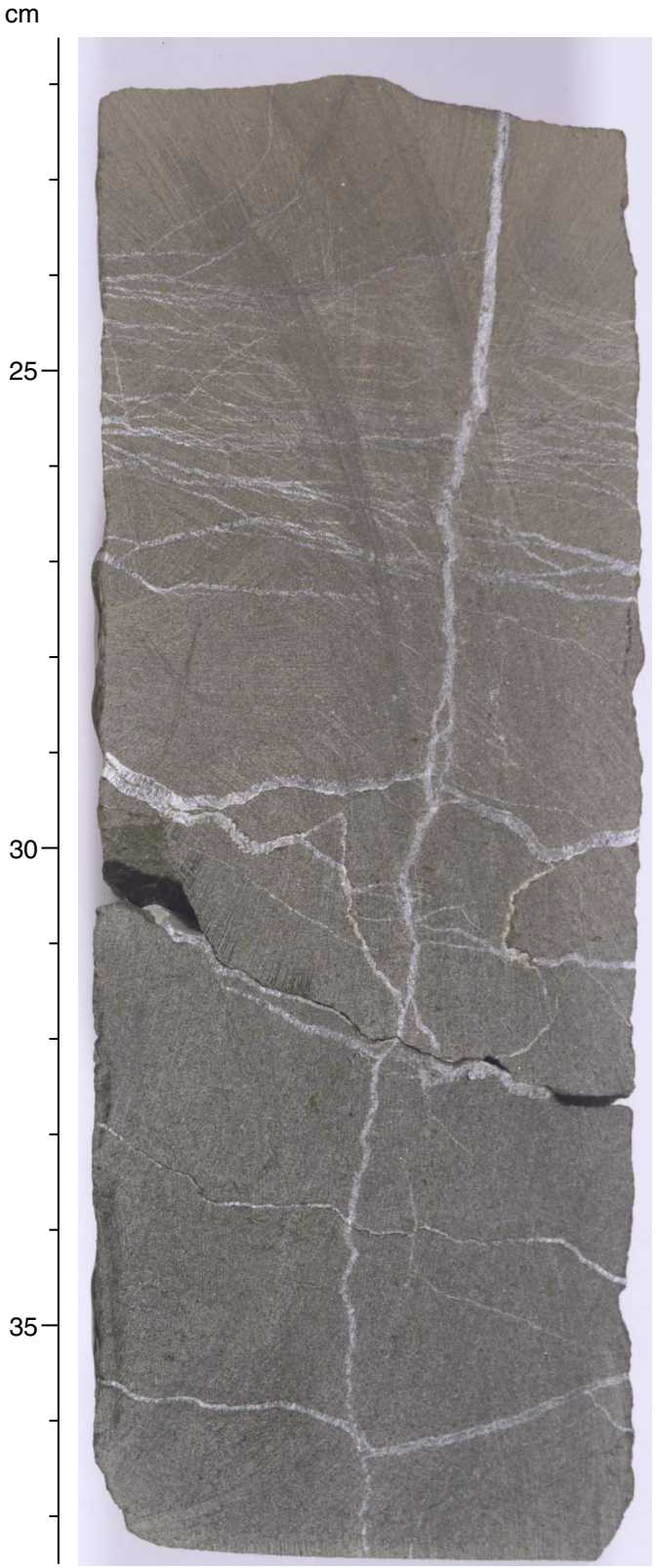

Figure F50. A spherulite in a yellow-brown halo in Sample **192-1185B-4R-1 (Piece 18, 142–144 cm).** The brown staining resulting from the olivine alteration enhances the fibroradial texture of the plagioclase and pyroxene. Elongate olivine crystals randomly scattered in the subvariolitic groundmass surrounding the spherulites are totally replaced by smectite and Fe oxyhydroxide. One skeletal olivine phenocryst replaced by the same secondary minerals can be observed (bottom center) (overall alteration = 3%–5%; field of view = 5.5 mm; plane-polarized light; photomicrograph ID# 1185B_218).

Figure F51. Interval 192-1185B-4R-1, 103–111 cm, showing totally altered hyaloclastite from the upper alteration zone, containing green to yellowish brown glass fragments completely replaced by smectite and cemented by white and pink carbonate.

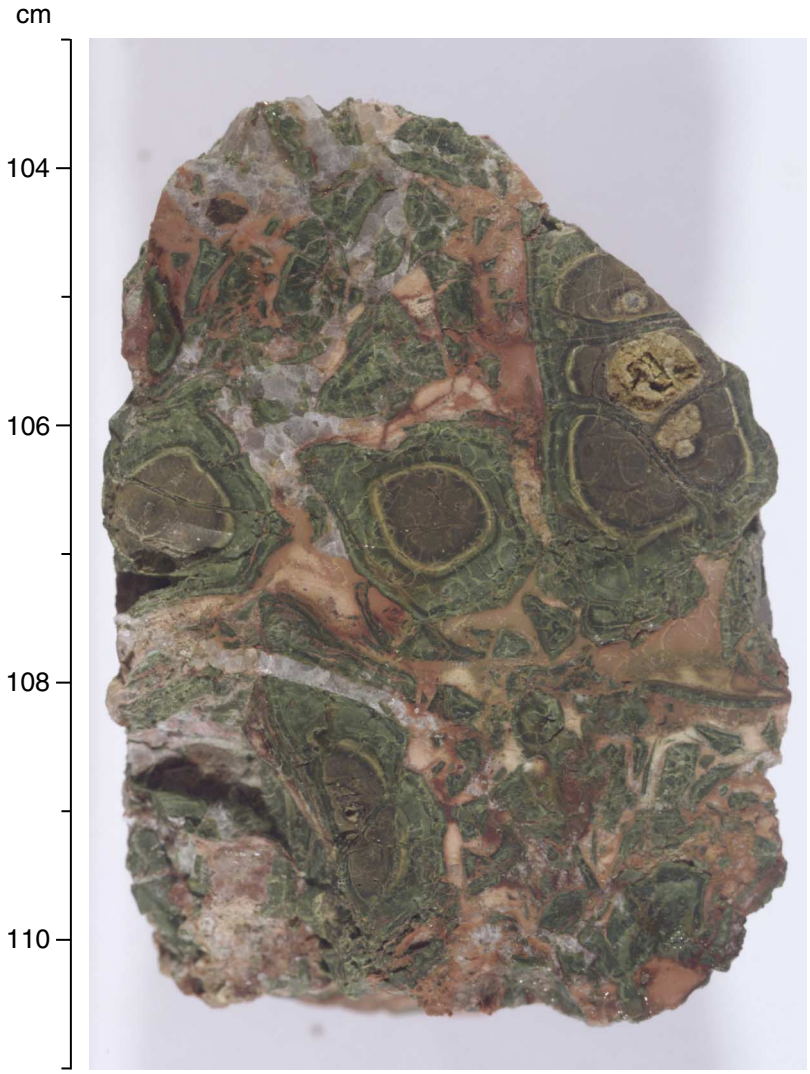

Figure F52. Basalt showing total replacement of olivine phenocrysts (upper left) and groundmass by smectite and Fe oxyhydroxide in Sample **192-1185B-12R-1 (Piece 6, 40–44 cm).** The photomicrograph is of a light yellow-brown halo along a sparry calcite and micritic sediment vein (partially visible, bottom right). Plagioclase is unaltered. Miarolitic voids are filled with zoned smectite (center left and below center right) (overall alteration = 15%; field of view = 5.5 mm; plane-polarized light; photomicrograph ID# 1185B_213).

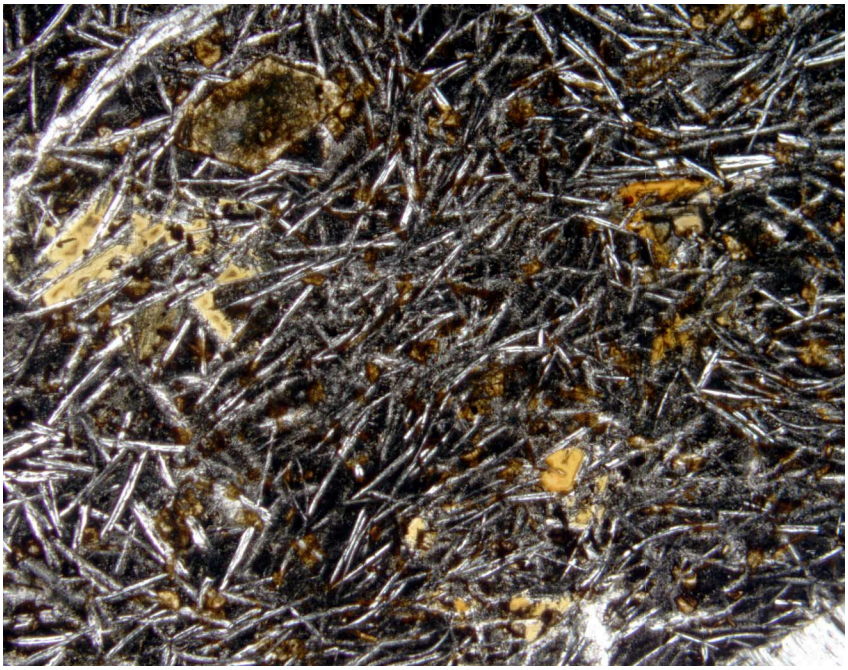

Figure F53. Basalt showing total replacement of small olivine phenocrysts, skeletal elongate olivine crystals, and glassy groundmass by smectite and Fe oxyhydroxide in Sample 192-1185B-5R-8 (Piece 3, 31–33 cm). The photomicrograph is of a light yellow-brown zone cut by parallel, subhorizontal veins of calcite (not visible). Plagioclase and clinopyroxene are unaltered (overall alteration = 25%–30%; field of view = 1.4 mm; plane-polarized light; photomicrograph ID# 1185B_194).

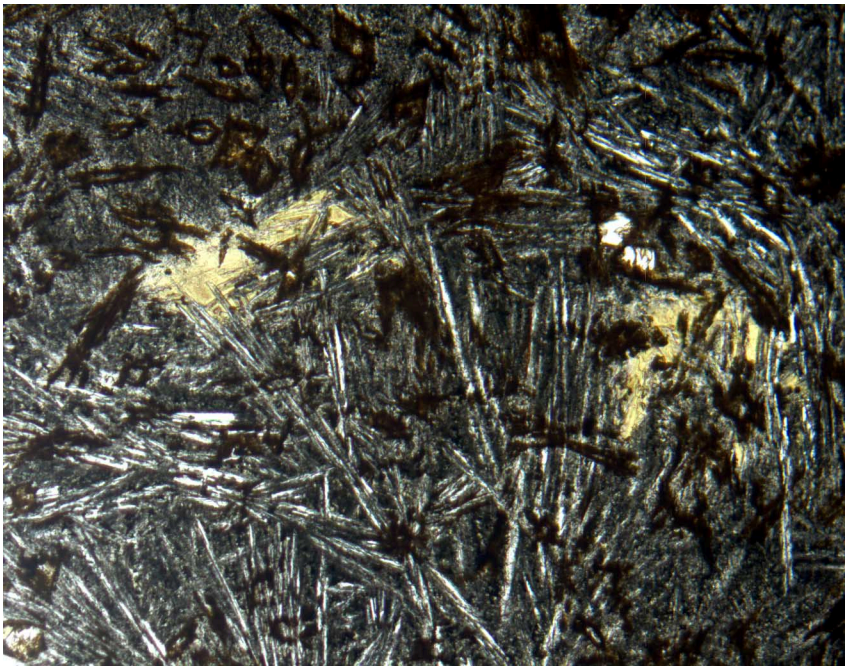

Figure F54. Basalt locally replaced by a prismatic zeolite (probably phillipsite) and smectite in the wall rock adjacent to a calcite + zeolite vein (outside field of view) in Sample 192-1185B-5R-8 (Piece 3, 31–33 cm). The subvariolitic texture of the basalt is preserved only in a few small areas (center left, lower center) (field of view = 5.5 mm; plane-polarized light; photomicrograph ID# 1185B_199).

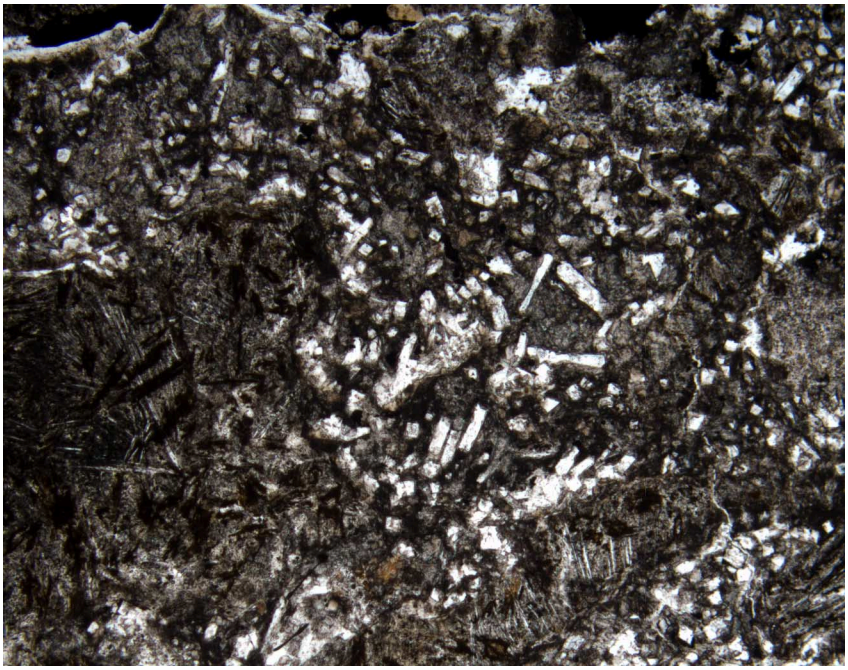

Figure F55. Interval 192-1185B-17R-1, 0–24 cm, showing pervasively altered angular basalt fragments in breccia cemented by fine-grained carbonate sediment at the top of Unit 10.

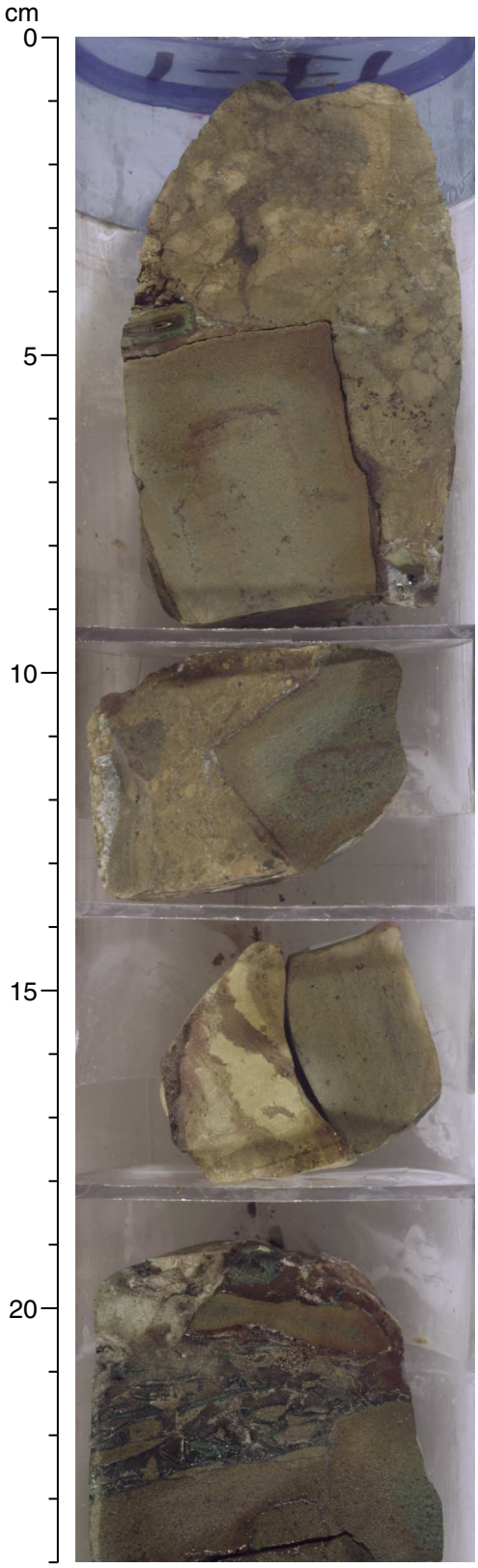

Figure F56. Dusky green basalt with olivine phenocrysts totally replaced by celadonite in Sample **192-1185B-22R-7 (Piece 2, 42–43 cm);** the groundmass glass is slightly replaced by the same secondary mineral. Plagioclase and clinopyroxene are unaltered (overall alteration = 3%–5%; field of view = 1.4 mm; plane-polarized light; photomicrograph ID# 1185B_212).

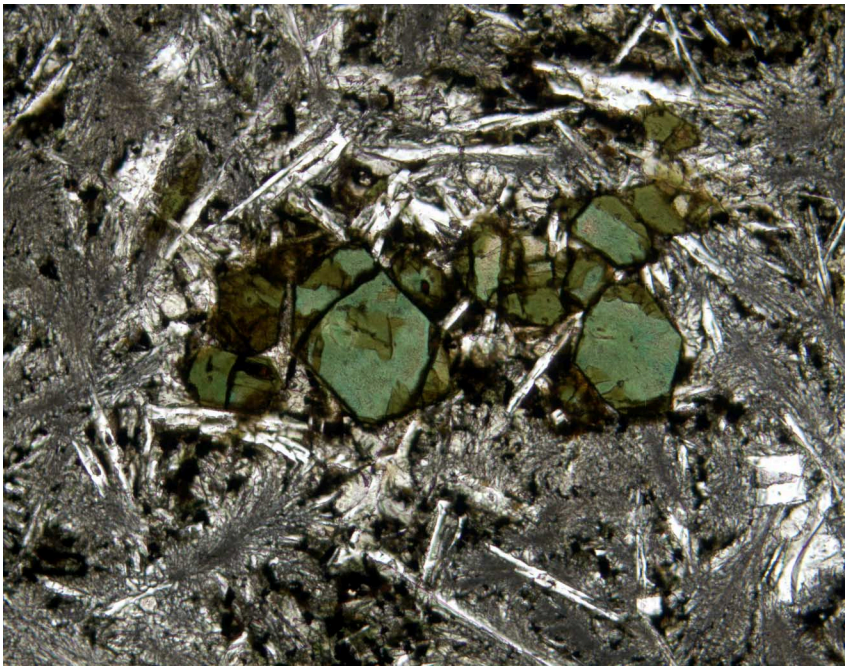

Figure F57. Interval 192-1185B-21R-1, 4–13 cm, showing olive halos and dusky green basalt near calcite-smectite veins in the lower alteration zone. This sample contains abundant celadonite in the groundmass and replacing olivine phenocrysts.

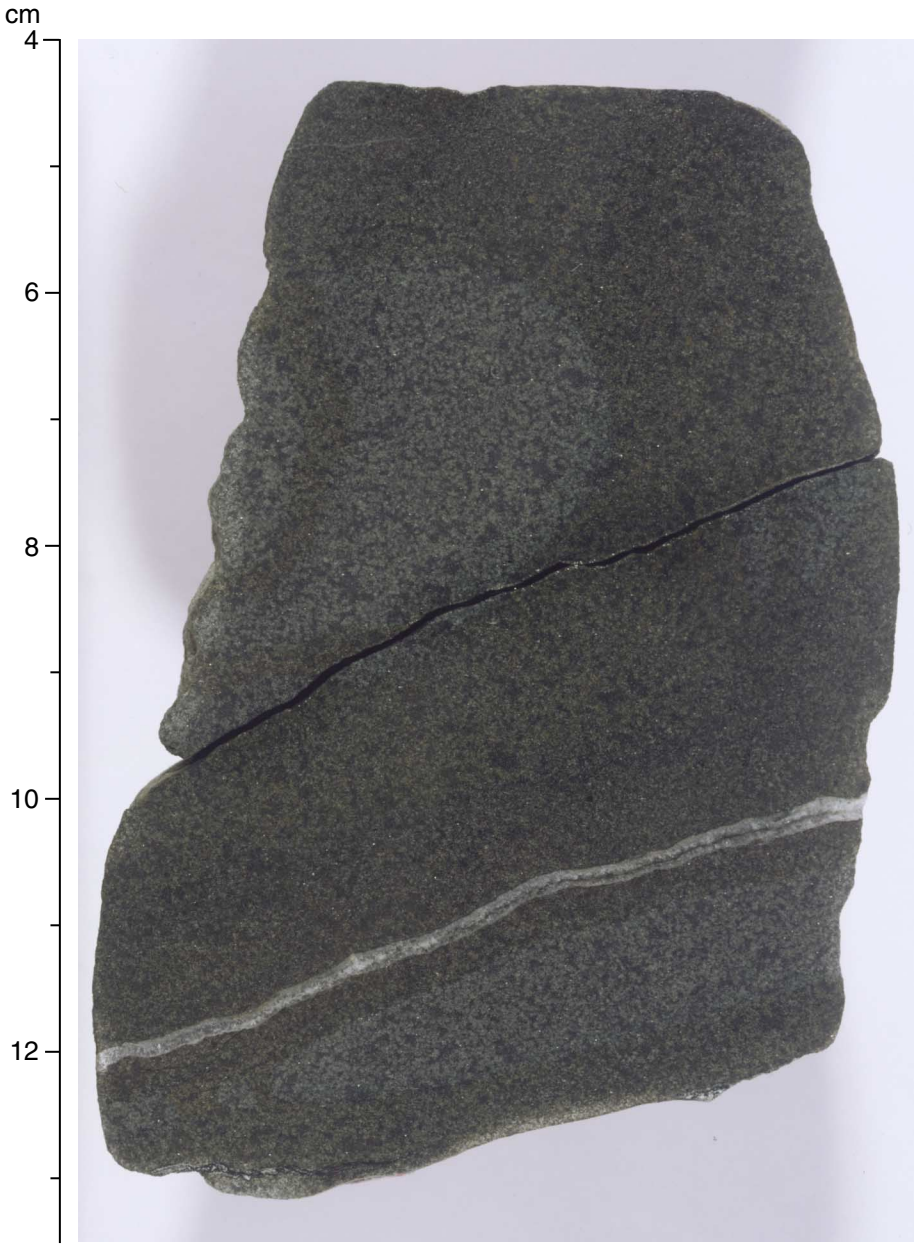

Figure F58. Typical gray, fine-grained basalt illustrating total replacement of the olivine phenocrysts and groundmass glass by smectite in Sample **192-1185B-17R-3 (Piece 1A, 1–3 cm).** Plagioclase and clinopyroxene are unaltered (overall alteration = 15%–20%; field of view = 5.5 mm; plane-polarized light; photomicrograph ID# 1185B_217).

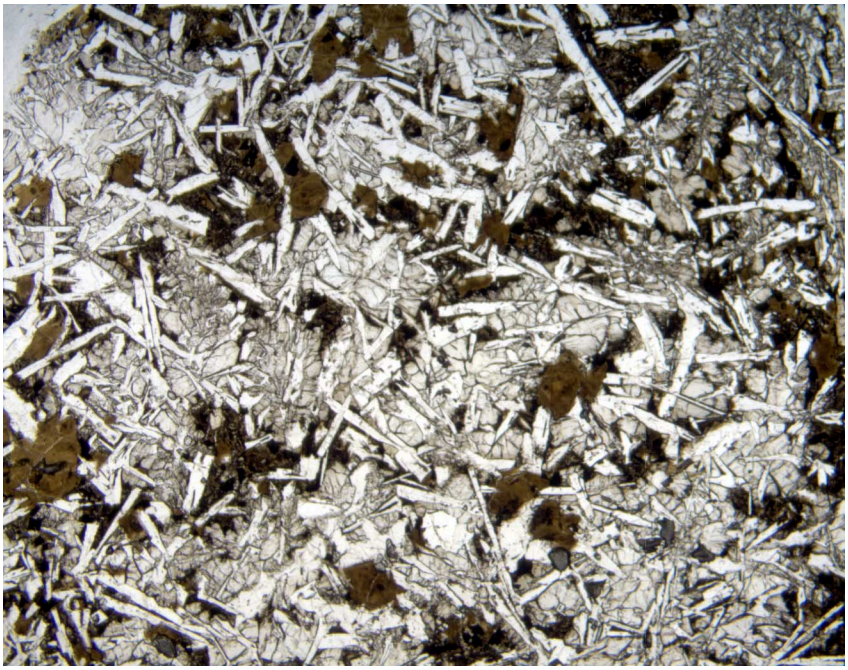

Figure F59. Miarolitic cavities, with alteration halos, are filled by the following succession of secondary minerals in Sample **192-1185B-20R-1 (Piece 4, 27–29 cm)** (from walls to center): calcite, yellow smectite grading through orange iddingsite into goethite, and celadonite (top center). Plagioclase is unaltered, and the host rock contains no olivine or secondary-mineral pseudomorphs after olivine (overall alteration = 20%; field of view = 5.5 mm; plane-polarized light; photomicrograph ID# 1185B_215).

Figure F60. Photomicrograph, at higher magnification, of Sample **192-1185B-20R-1 (Piece 4, 27–29 cm)** showing the large miarolitic cavity in Figure **F59,** p. 86 (top center) (field of view = 1.4 mm; plane-polarized light; photomicrograph ID# 1185B_216).

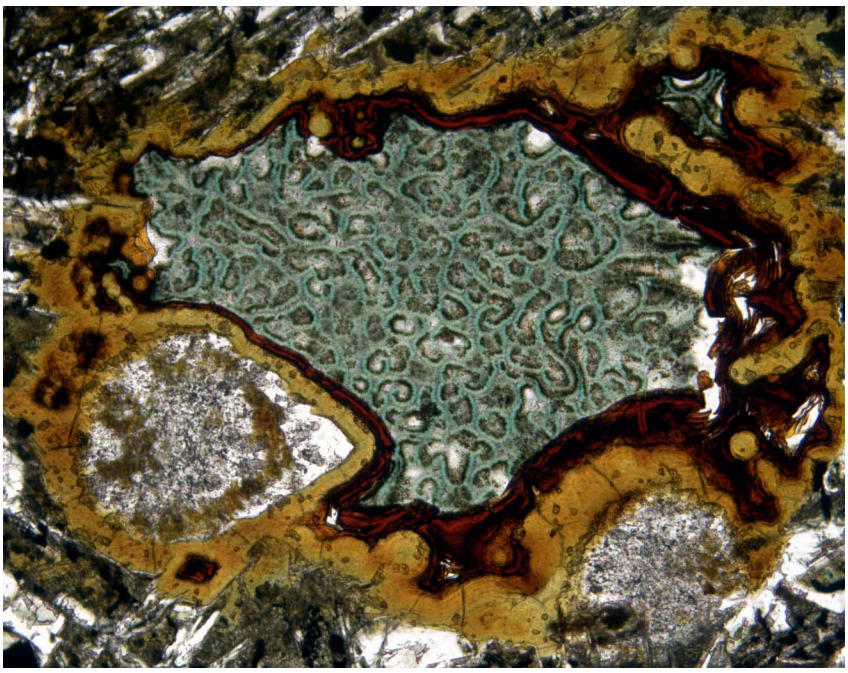

Figure F61. A dark yellow-brown halo around a gray inner zone (outside field of view), crossed by a vein of celadonite with minor green smectite (nontronite?) in Sample 192-1185B-20R-4 (Piece 1C, 16–19 cm). The host rock displays total replacement of the olivine phenocrysts and glassy groundmass by smectite. Plagioclase and clinopyroxene are unaltered (overall alteration = 40%; field of view = 5.5 mm; plane-polarized light; photomicrograph ID# 1185B_214).

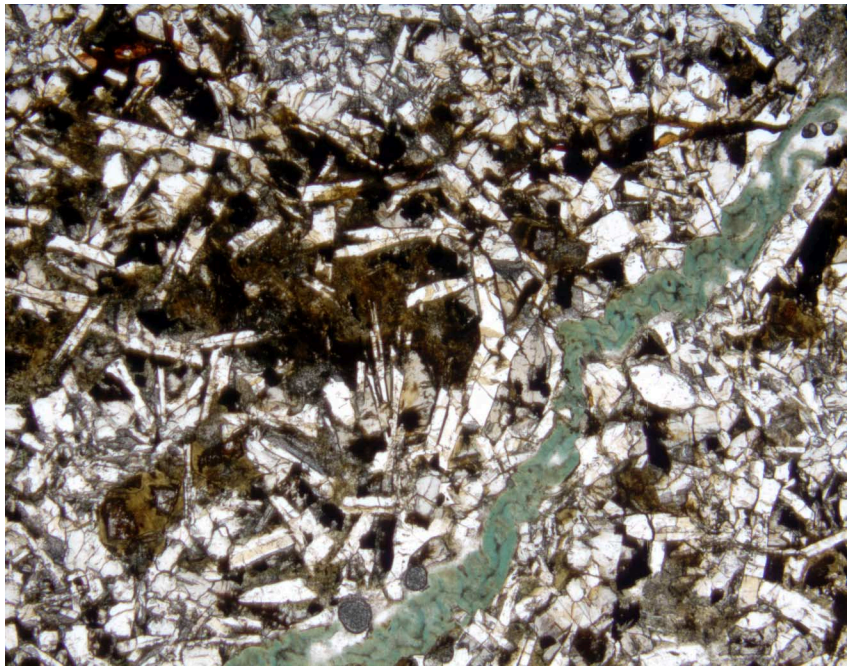

Figure F62. A 3- to 5-mm-thick vein made up of the following sequence of secondary minerals in Sample 192-1185B-5R-8 (Piece 3, 31–33 cm) (from vein walls to center): a thin (~50–100 µm thick) tan smectite edge, botryoidal concretions of an opaque mineral (probably a Mn oxyhydroxide), discontinuous "screens" consisting of tan zeolites with opaque linings, and sparry calcite. Calcite forms ~85% of the vein. The zeolite screens are fragments of the wall lining plucked away from the walls during reopening of the vein when calcite precipitated. Note a vesicle lined with zoned, yellowish tan smectite (bottom left) (field of view = 5.5 mm; plane-polarized light; photomicrograph ID# 1185B_202).

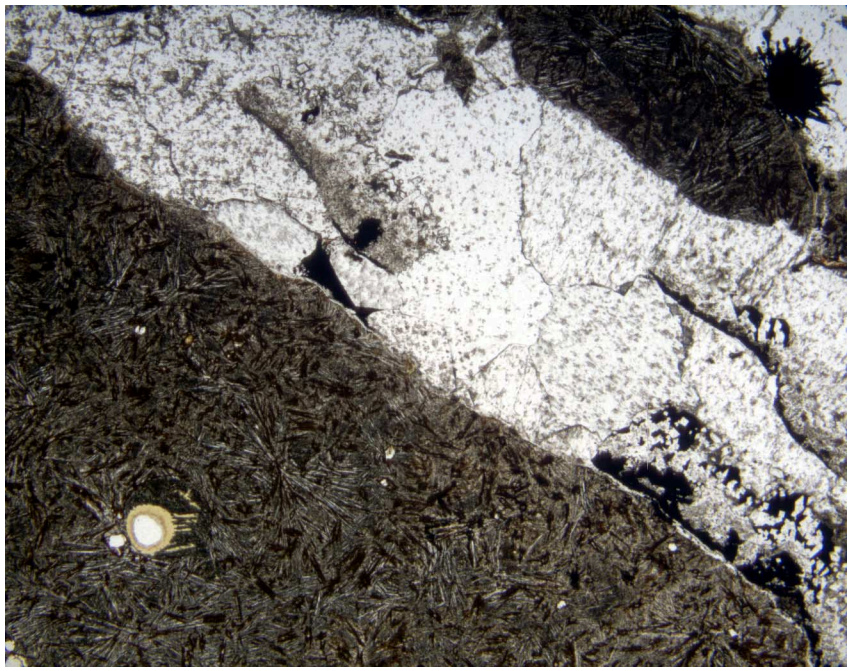

Figure F63. Photomicrograph, at higher magnification, of one of the zeolite "screens" visible in Figure F62, p. 89, showing the prismatic, longitudinal, and square cross sections characteristic of phillipsite. The zeolite screen is embedded in calcite in Sample 192-1185B-5R-8 (Piece 3, 31–33 cm) (field of view = 1.4 mm; plane-polarized light; photomicrograph ID# 1185B_201).

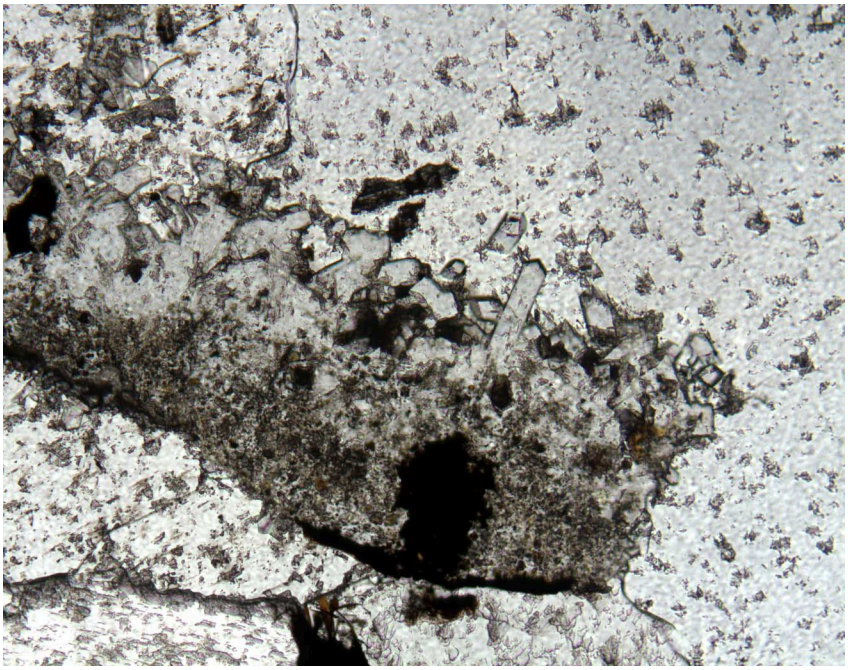

Figure F64. A euhedral crystal of zeolite (probably gmelinite or chabazite) in a secondary vein of opaque material (probably Mn oxyhydroxide) and calcite in Sample 192-1185B-5R-8 (Piece 3, 31–33 cm) (field of view = 5.5 mm; photomicrograph ID#s 1185B_203 and 1185B_204) **A.** Plane-polarized light. **B.** Crossed polars. Note the twinning in the zeolite.

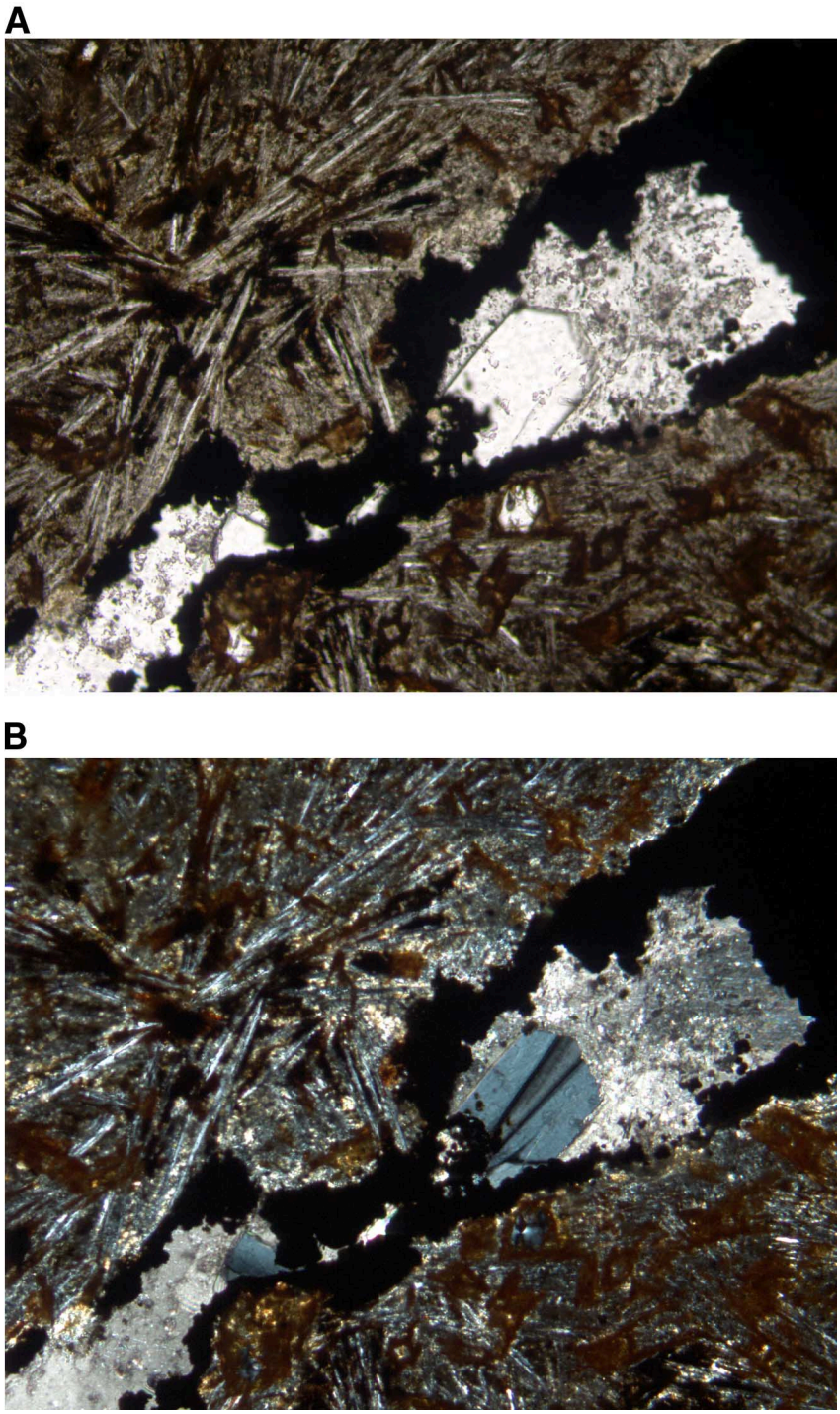

Figure F65. A botryoidal aggregate of opaque material (probably Mn oxyhydroxide) in a calcite vein with smectite locally lining the vein walls in Sample 192-1185B-5R-8 (Piece 3, 31–33 cm) (field of view = 2.8 mm; plane-polarized light; photomicrograph ID# 1185B_196).

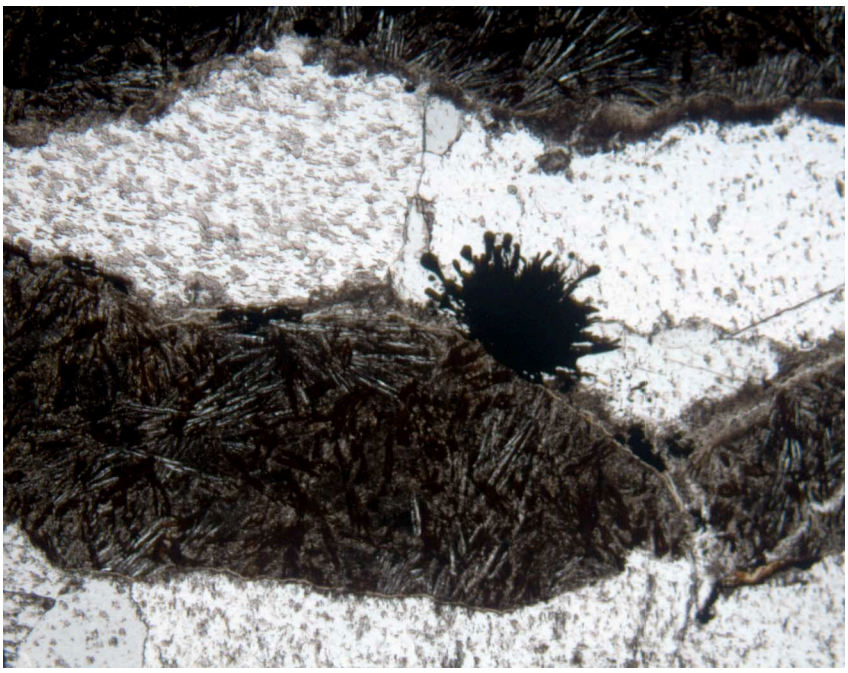

Figure F66. A 3- to 5-mm-thick micritic sediment and sparry calcite vein in Sample 192-1185B-5R-3 (Piece 1A, 32–34 cm). Approximately 95% of the wall rock on both sides of the vein is replaced by brownish tan smectite forming 2- to 4-mm-wide brown halos. Total replacement of the olivine phenocrysts and groundmass glass by smectite brings the overall alteration of the host rock to 15%–20%. Plagioclase and clinopyroxene are unaltered (field of view = 5.5 mm; plane-polarized light; photomicrograph ID# 1185B_192).

Figure F67. Interval 192-1185B-17R-1, 18–51 cm, showing complex halos developed near smectite (±calcite) veins in the lower alteration zone. Olive halos are developed near veins and in the hyaloclastite at the top of the piece. Broader dusky green halos extend several centimeters beyond the olive halos and display sharp boundaries with the gray basalt interiors. The dusky green halos and gray basalt interiors both contain celadonite in the groundmass and replacing olivine phenocrysts.

Figure F68. Basement recovery, fracture density, vein abundance, and true dip of basaltic basement recovered from Hole 1185A.

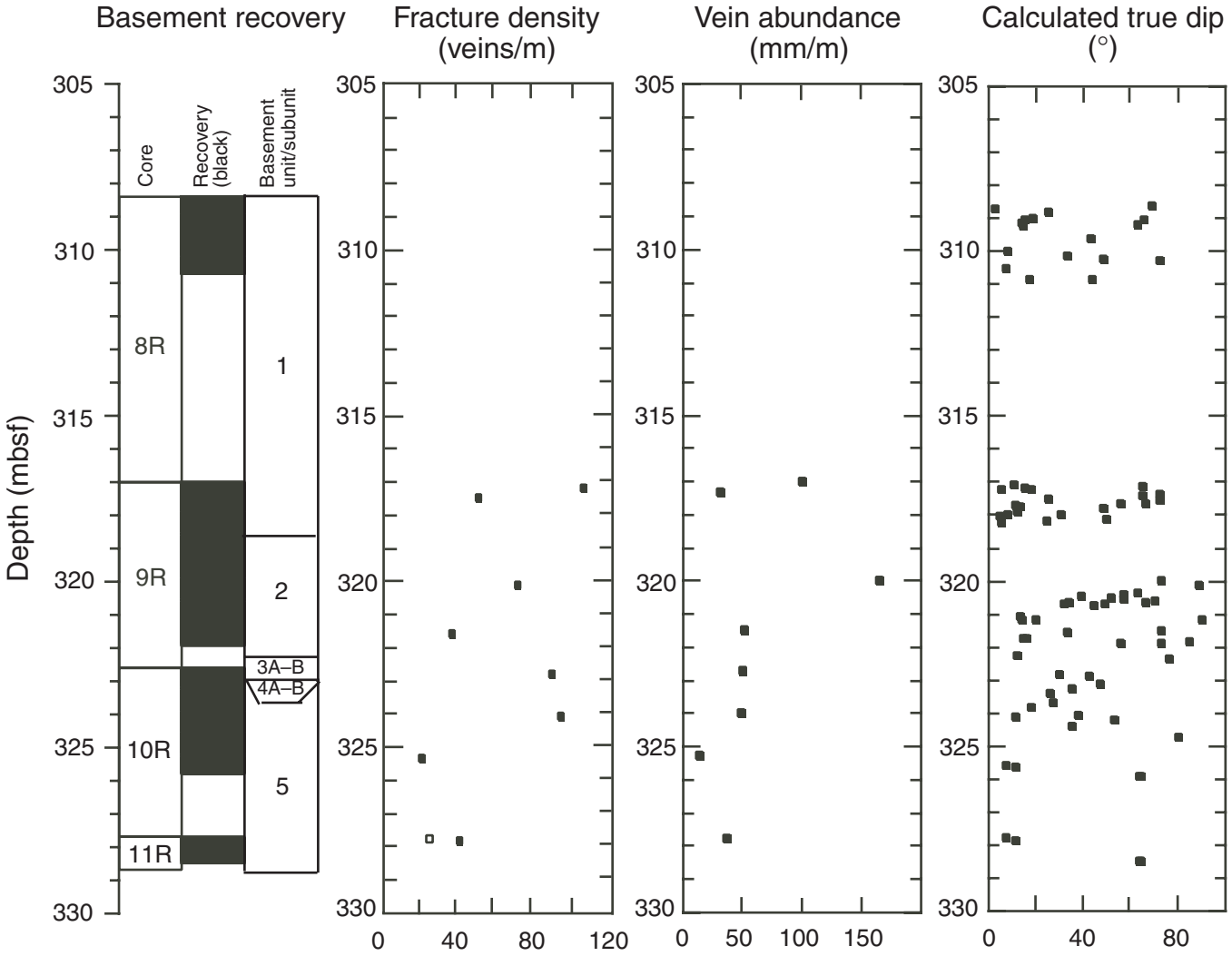

Figure F69. Basement recovery, fracture density, vein abundance, and true dip of basaltic basement recovered from Hole 1185B.

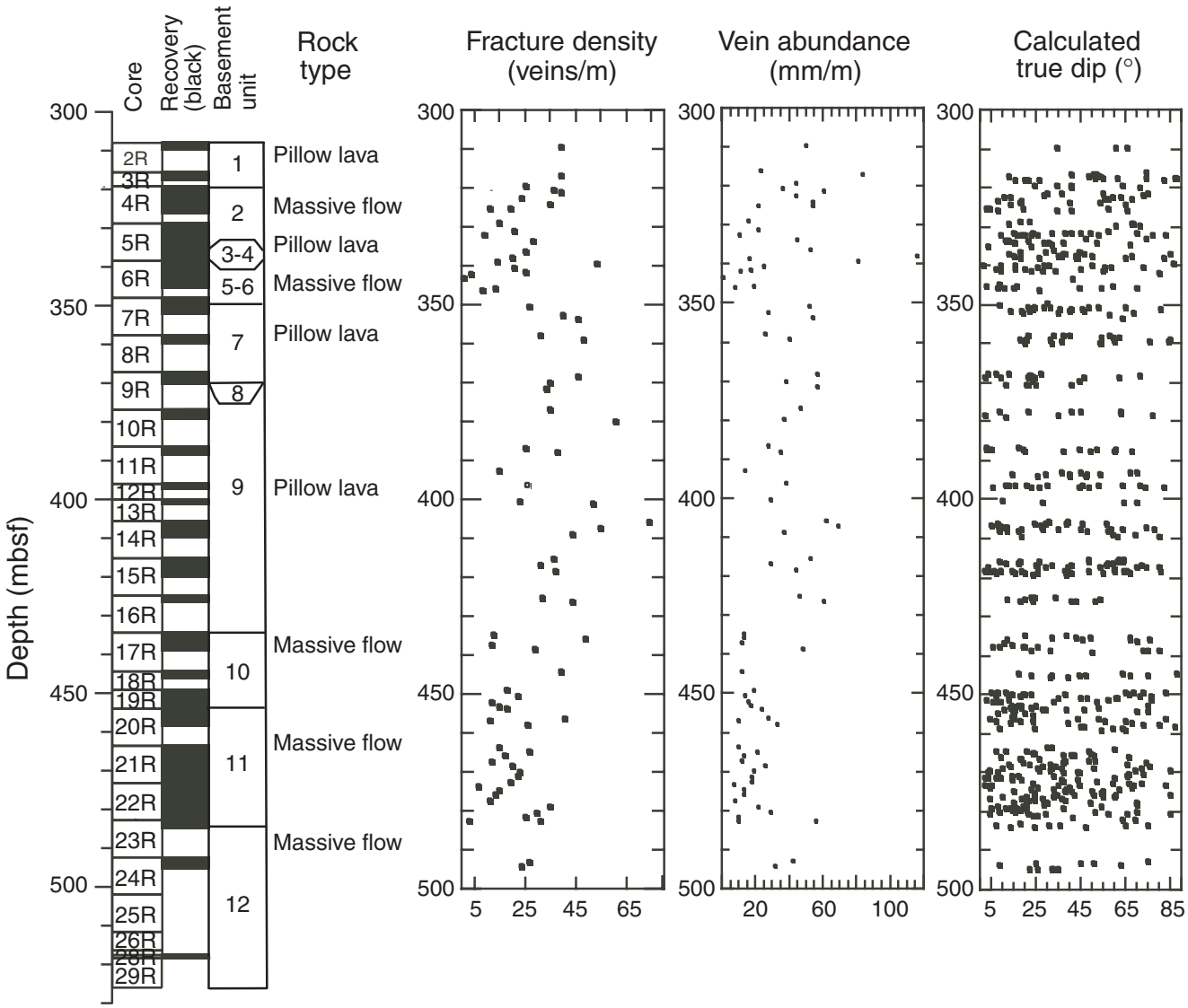

Figure F70. Examples of good-quality Zijderveld diagrams for archive-half core measurements of (**A**) a sediment sample from Section 192-1185B-2R-1, 65 cm, and (**B**) basalt Piece 1 from Section 192-1185B-21R-4.

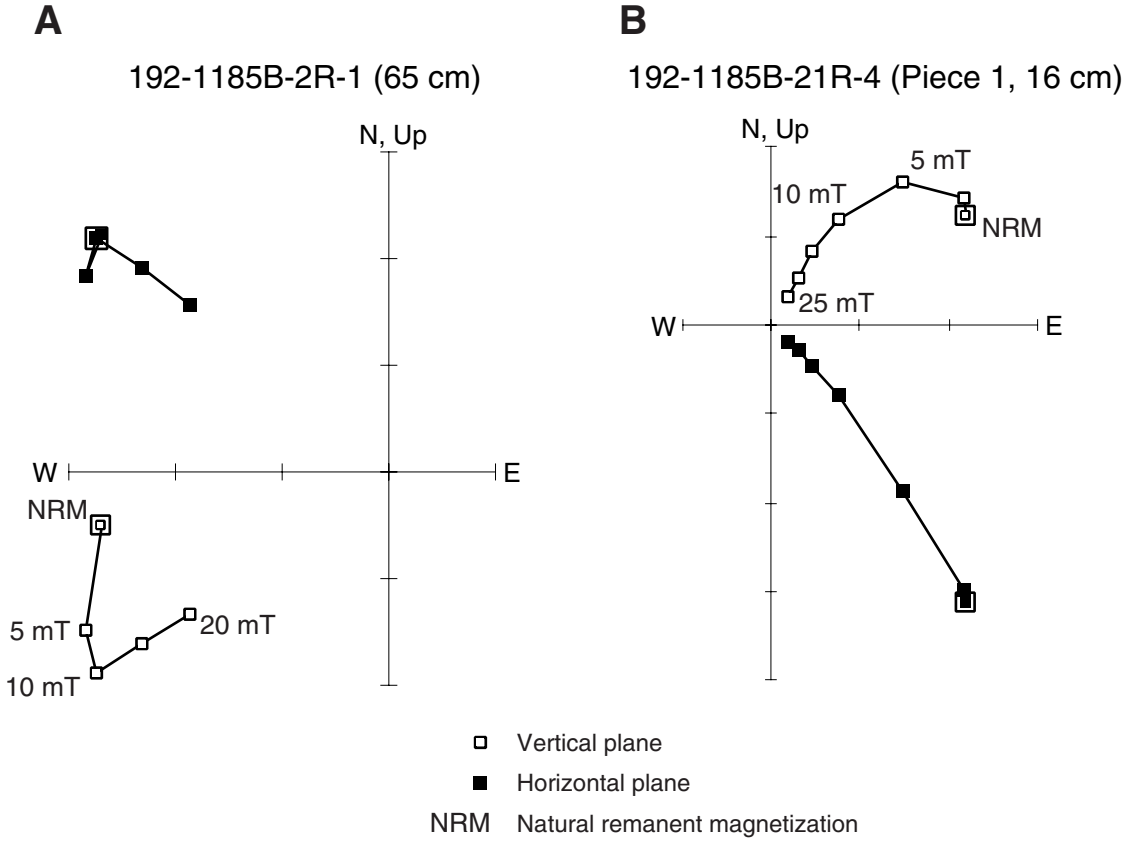

Figure F71. Biostratigraphic nannoplankton (NP) zonation, magnetic polarity data, and the suggested correlation with the geomagnetic polarity timescale (GPTS) at Site 1185.

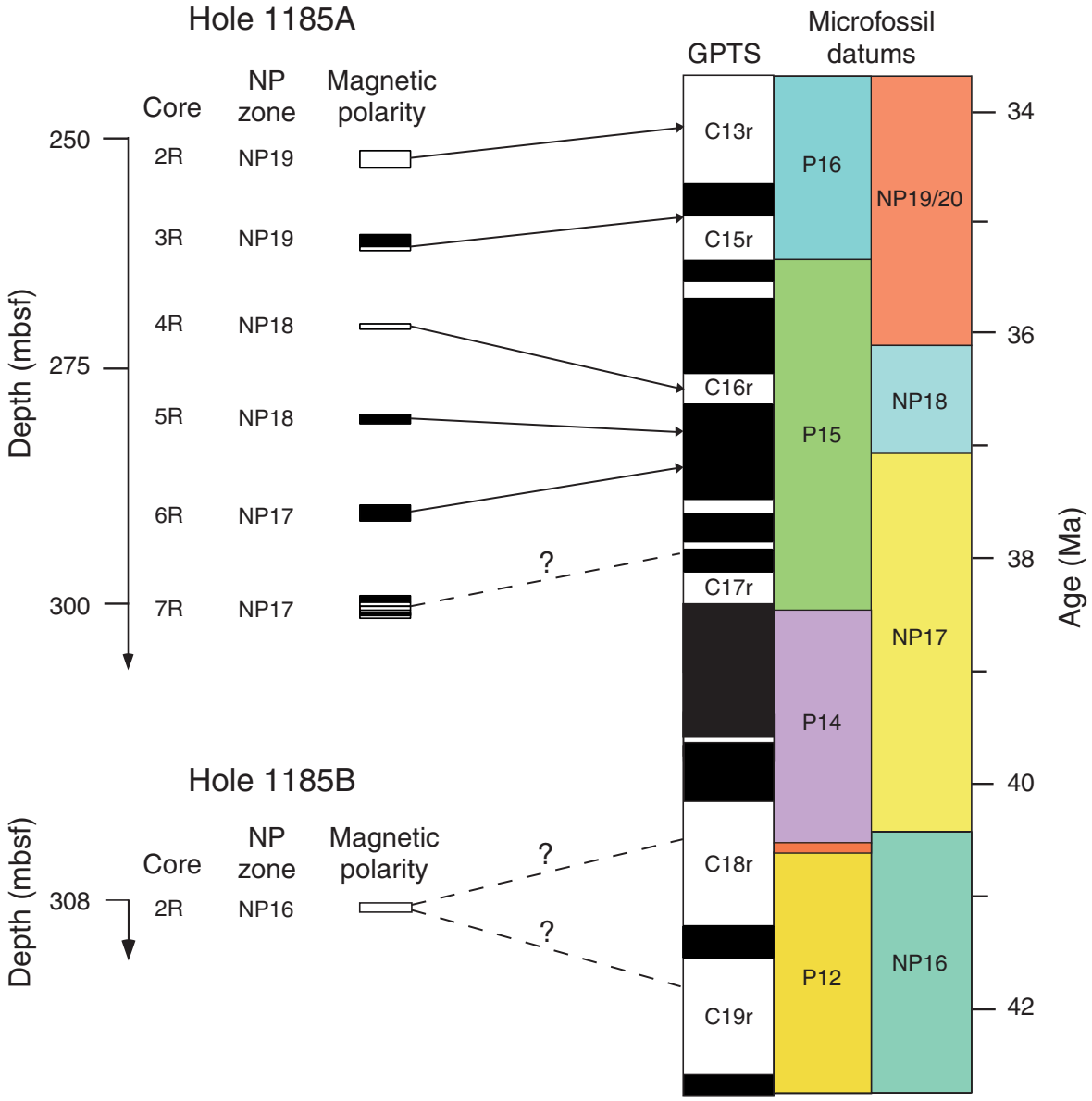

Figure F72. Downhole variations in natural remanent magnetization (NRM), magnetic susceptibility, Koenigsberger ratio (Q-ratio), and median destructive field (MDF) for basaltic units in Site 1185.

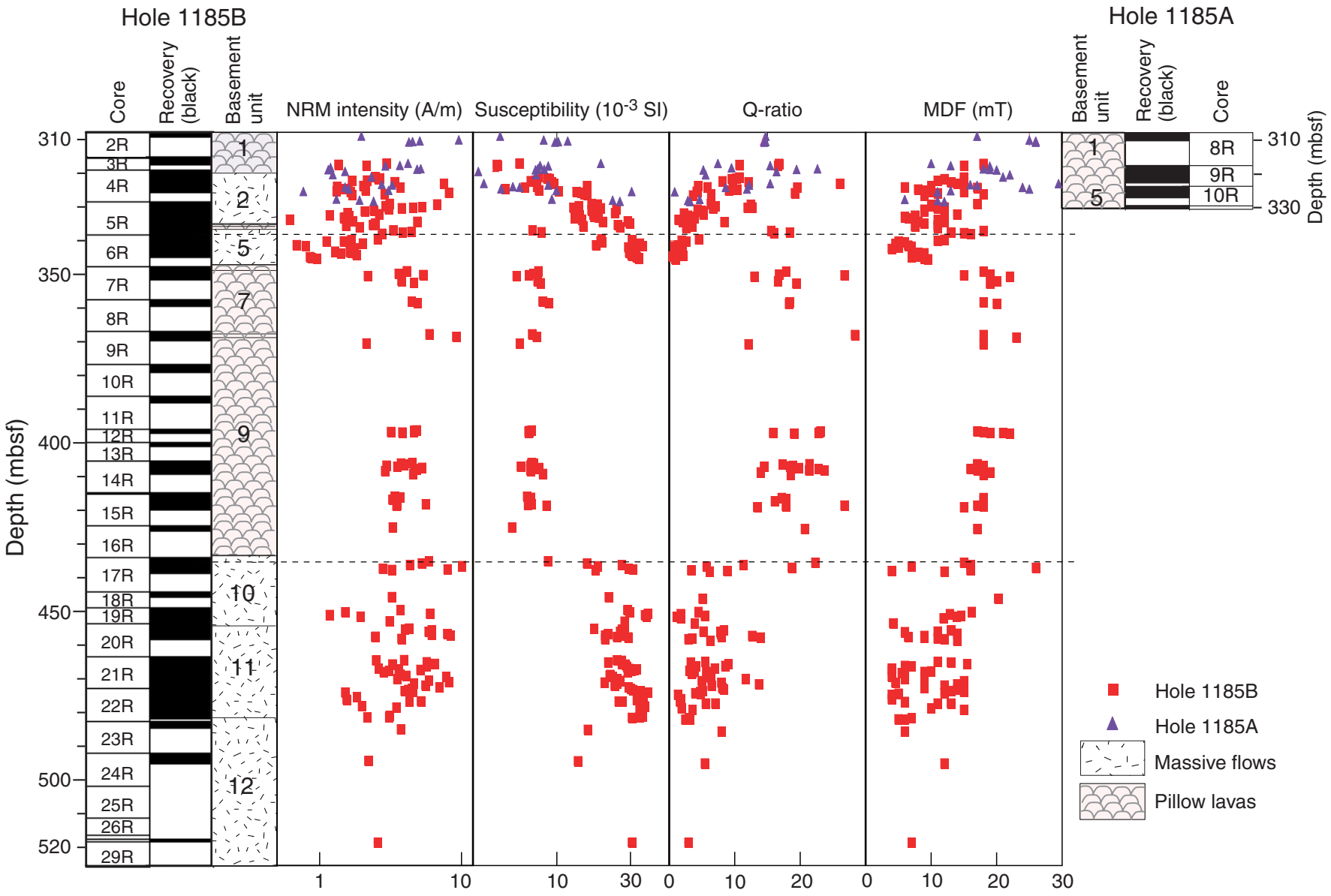

Figure F73. Downhole variation in mean characteristic remanent magnetization (ChRM) inclination for paleomagnetic units in Holes 1185A (A1–A4) and 1185B (B1–B18). Boxes = depth intervals and the mean inclinations (95% confidence angles) for each paleomagnetic unit; circles = paleomagnetic units with <3 ChRM determinations.

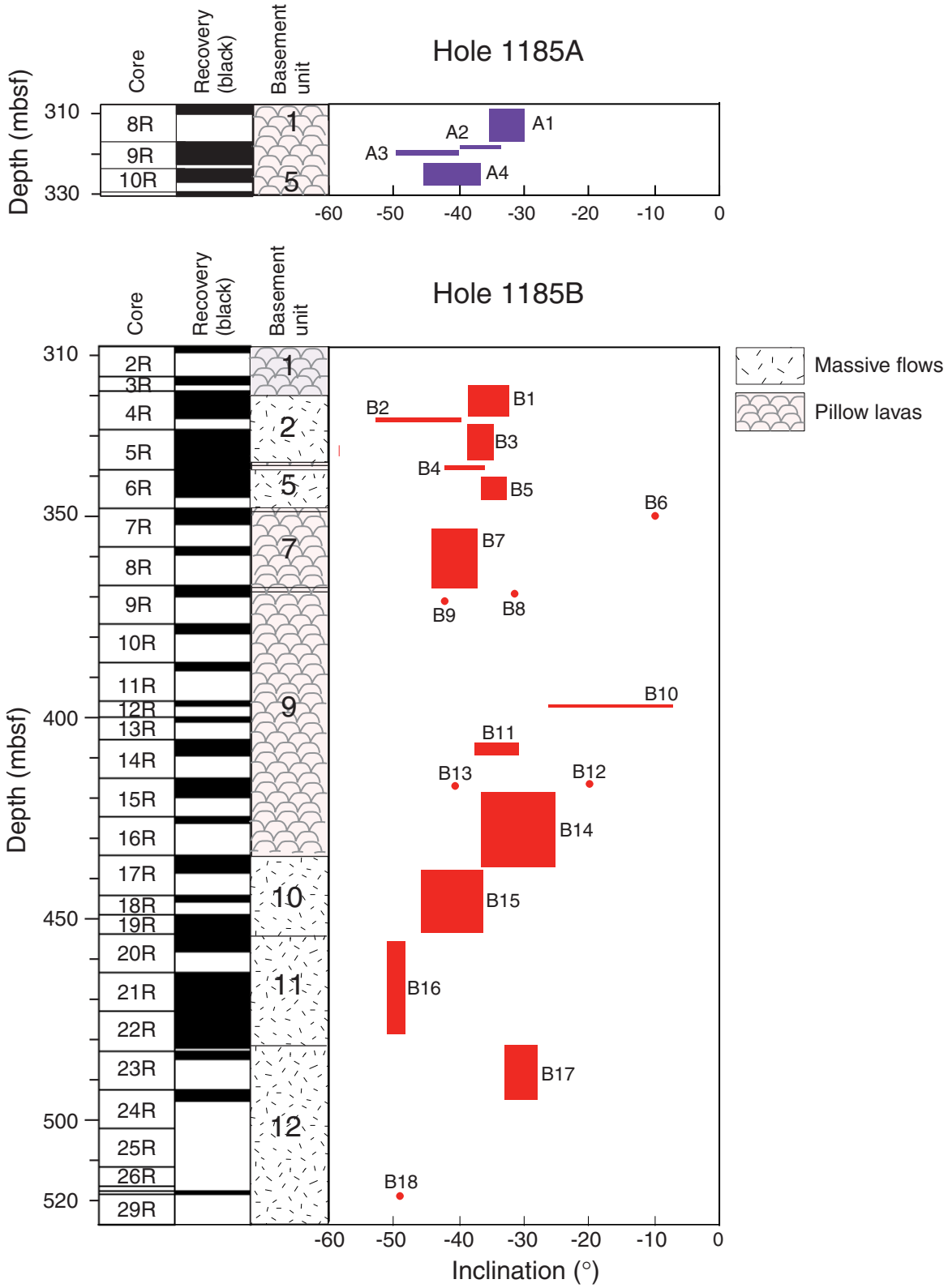

Figure F74. Index properties and thermal conductivity vs. depth for Hole 1185A. Discrete samples for index property measurements were not taken from basement Units 1–5 in Sections 192-1185A-8R and 9R and 192-1185A-10R-1 and 10R-2.

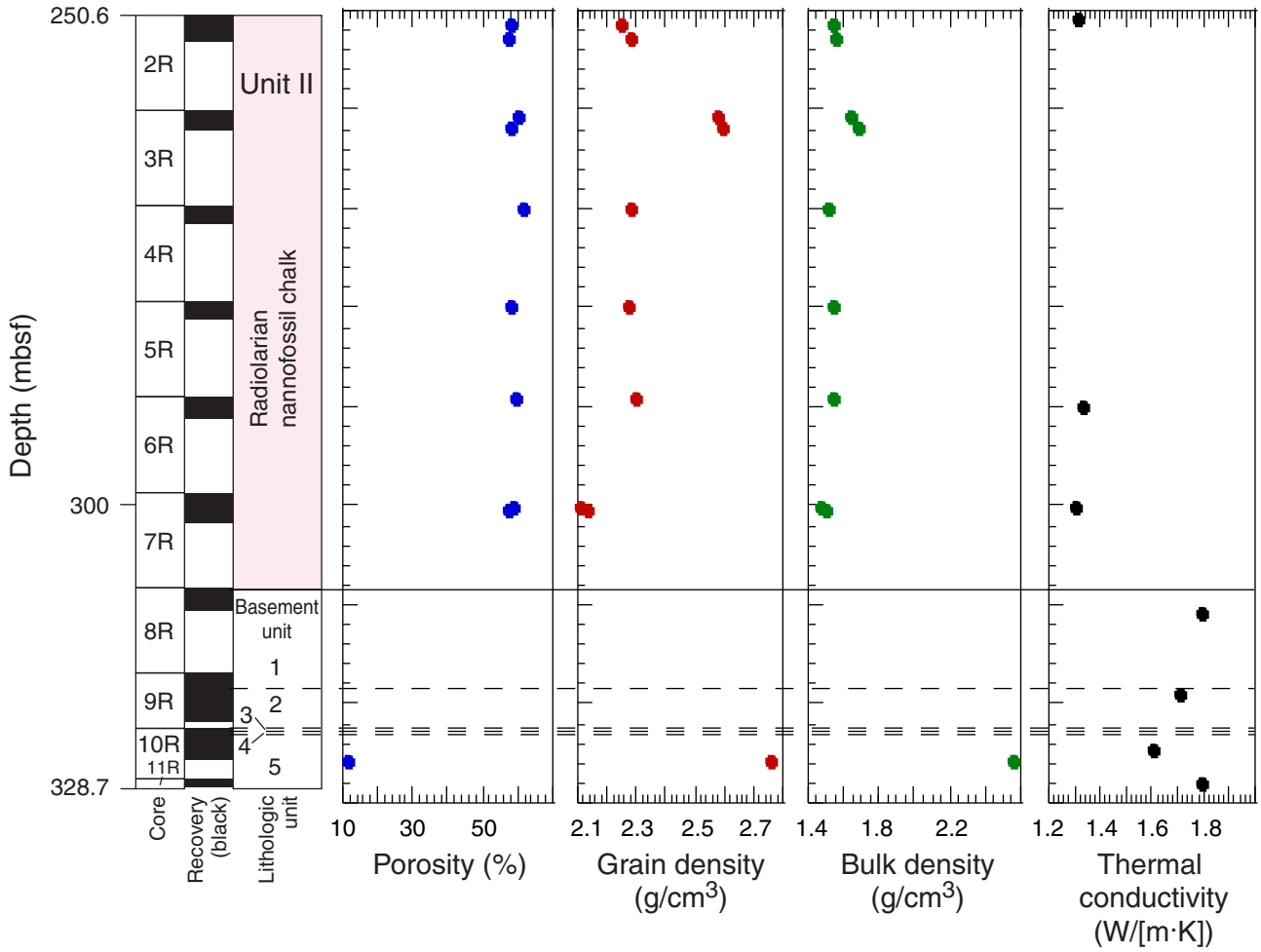

Figure F75. Index properties and thermal conductivity vs. depth for Hole 1185B. Sedimentary units are shaded in the "Lithologic unit" column; basement units are unshaded.

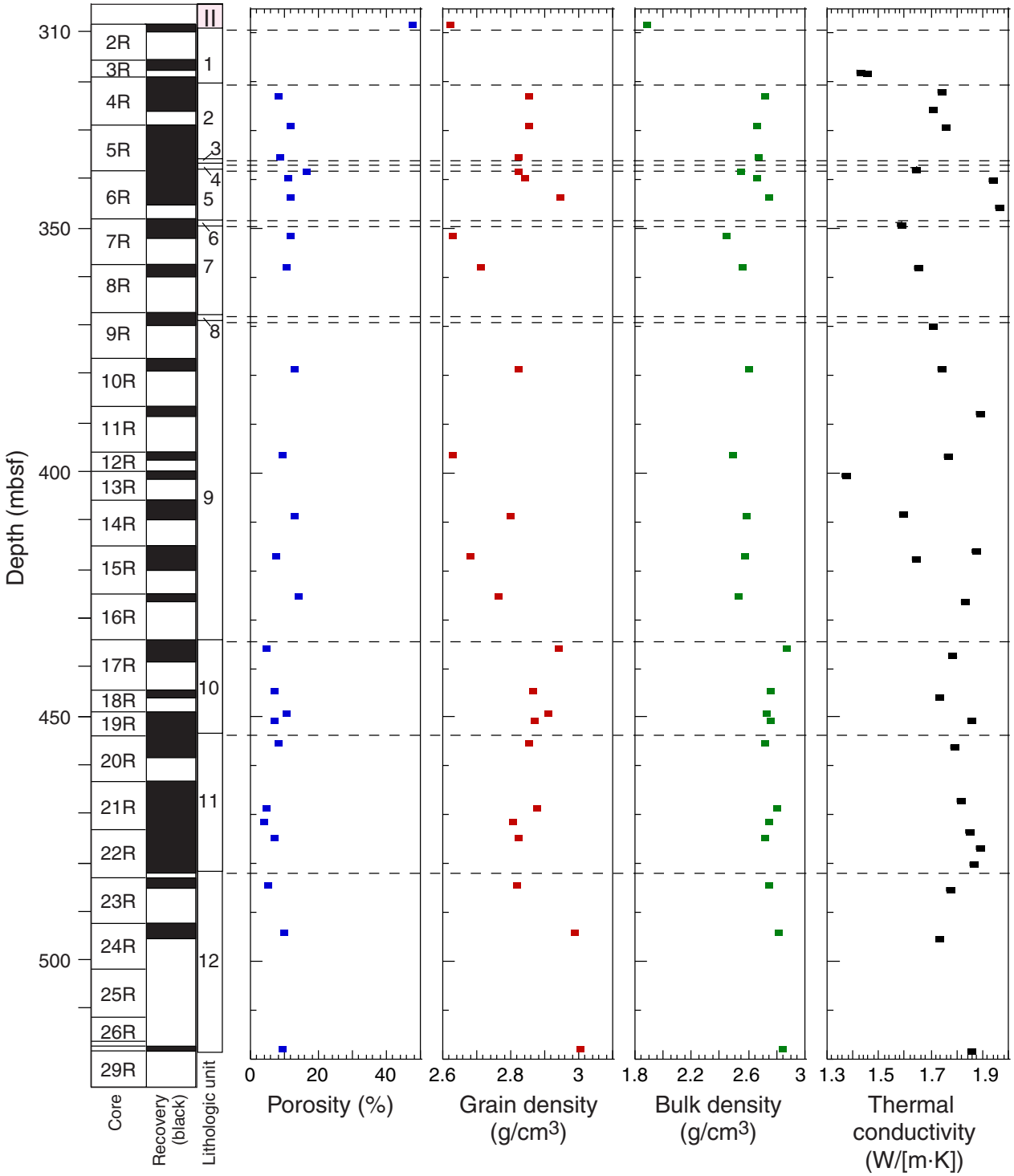

Figure F76. Velocity and whole-core measurements vs. depth for Hole 1185A. Sedimentary units are shaded in the "Lithologic unit" column; basement units are unshaded.

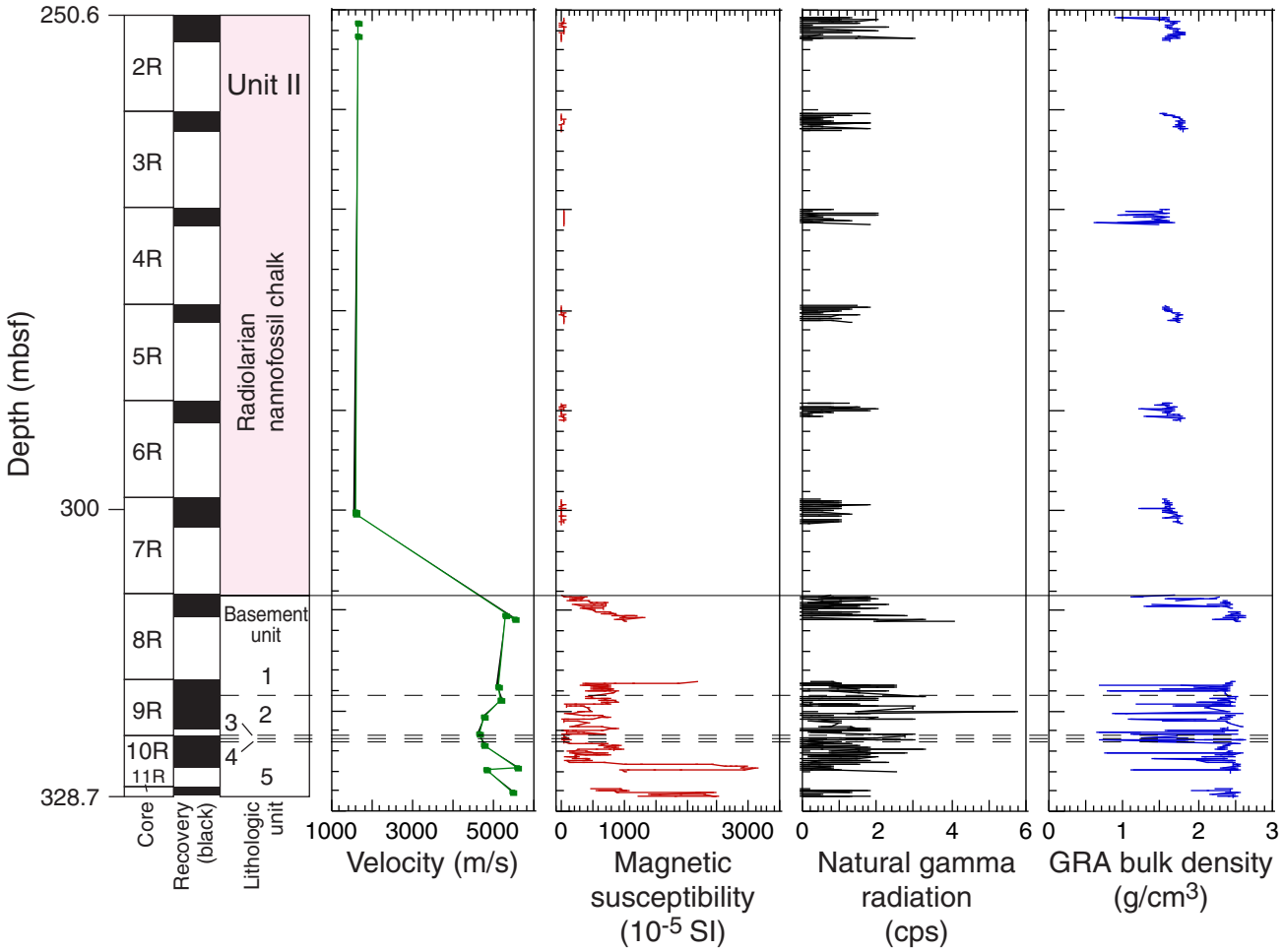

Figure F77. Velocity and whole-core measurements vs. depth for Hole 1185B. Sedimentary units are shaded in the "Lithologic unit" column; basement units are unshaded.

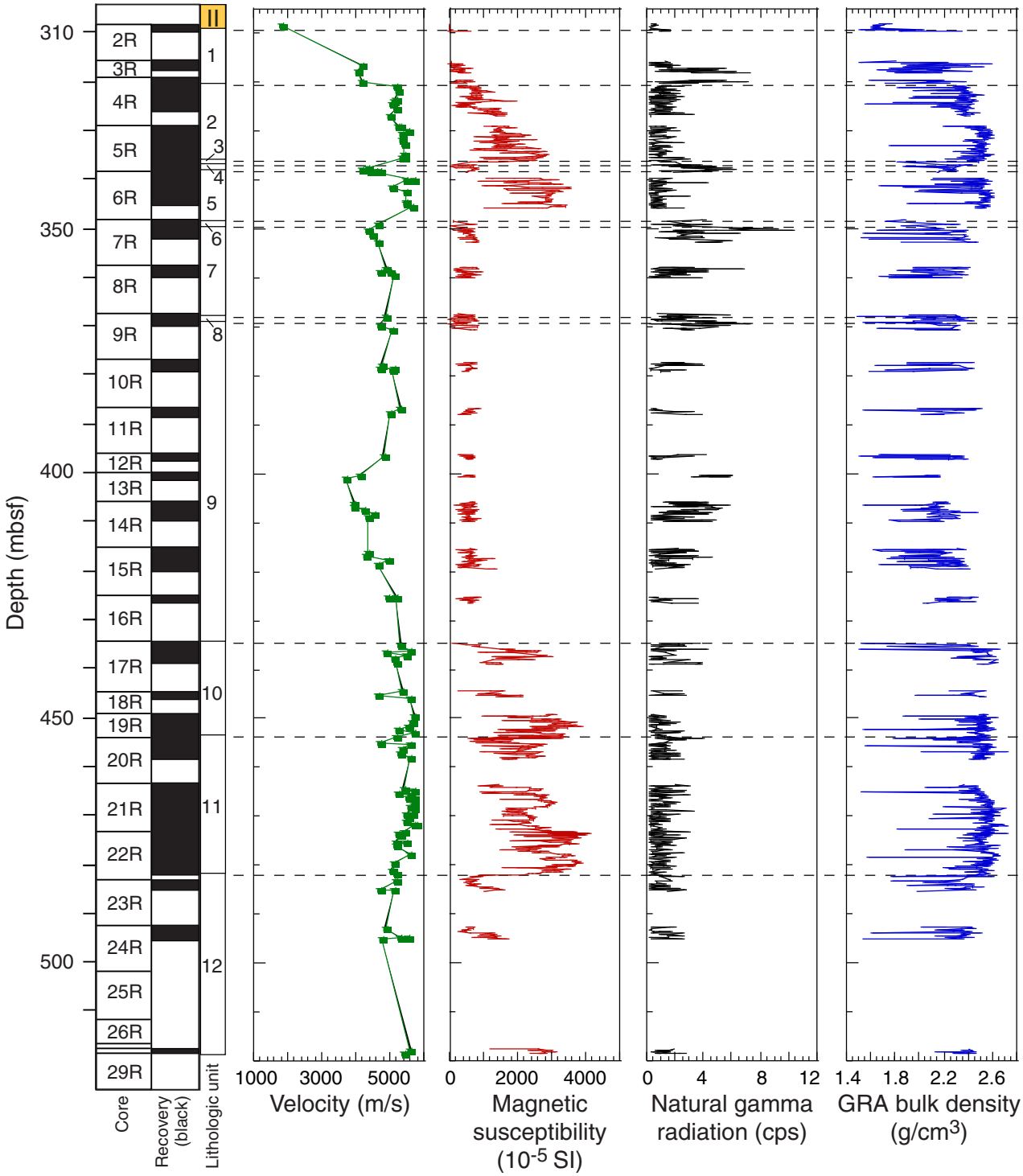

Table T1. Coring summary, Site 1185.

Core	Date (Oct 2000)	Time (local)	Depth (mbsf) Top	Depth (mbsf) Bottom	Length (m) Cored	Length (m) Recovered	Recovery (%)
192-1185A-							
1W	11	0745	0.0	250.6	0.0	NA	NA
2R	11	0845	250.6	260.2	9.6	2.67	27.8
3R	11	0955	260.2	269.8	9.6	2.06	21.5
4R	11	1055	269.8	279.5	9.7	1.86	19.2
5R	11	1150	279.5	289.1	9.6	1.83	19.1
6R	11	1245	289.1	298.8	9.7	2.22	22.9
7R	11	1345	298.8	308.4	9.6	3.04	31.7
8R	11	1715	308.4	317.0	8.6	2.36	27.4
9R	11	2210	317.0	322.6	5.6	4.95	88.4
10R	12	0210	322.6	327.7	5.1	3.20	62.7
11R	12	0425	327.7	328.7	1.0	0.80	80.0
				Cored:	78.1	24.99	32.0
				Drilled:	250.6		
				Total:	328.7		
192-1185B-							
1-0*	13	1205	0.0	30.5	0.0	NA	NA
1W	14	1905	30.5	308.0	0.0	NA	0.0
2R	14	2120	308.0	315.7	7.7	1.67	21.7
3R	14	2335	315.7	319.2	3.5	2.06	58.9
4R	15	0450	319.2	328.8	9.6	6.74	70.2
5R	15	1115	328.8	338.4	9.6	9.11	94.9
6R	15	1540	338.4	348.1	9.7	6.98	72.0
7R	15	1925	348.1	357.7	9.6	3.79	39.5
8R	16	0055	357.7	367.3	9.6	2.06	21.5
9R	16	0500	367.3	376.9	9.6	2.66	27.7
10R	16	1120	376.9	386.5	9.6	2.33	24.3
11R	16	1540	386.5	396.1	9.6	1.77	18.4
12R	16	2010	396.1	400.2	4.1	1.21	29.5
13R	16	2310	400.2	405.7	5.5	0.90	16.4
14R	17	0415	405.7	415.3	9.6	4.09	42.6
15R	17	0920	415.3	424.9	9.6	4.64	48.3
16R	17	1425	424.9	434.6	9.7	1.67	17.2
17R	19	0150	434.6	444.3	9.7	4.38	45.2
18R	19	0700	444.3	449.1	4.8	1.69	35.2
19R	19	1140	449.1	453.9	4.8	5.11	106.5
20R	19	1840	453.9	463.6	9.7	4.43	45.7
21R	20	530	463.6	473.2	9.6	10.16	105.8
22R	20	1105	473.2	482.8	9.6	8.98	93.5
23R	20	1555	482.8	492.5	9.7	2.13	22.0
24R	20	2145	492.5	502.1	9.6	2.63	27.4
25R	21	0520	502.1	511.8	9.7	0.00	0.0
26R	21	0805	511.8	516.6	4.8	0.00	0.0
27R	21	1150	516.6	517.6	1.0	0.00	0.0
28R	21	1450	517.6	518.6	1.0	0.98	98.0
29R	21	1805	518.6	526.1	7.5	0.00	0.0
				Cored:	218.1	92.17	42.3
				Drilled:	308.0		
				Total:	526.1		

Notes: NA = not applicable. * = Core 1-0 in Hole 1185B is the interval for jet in of 16-in casing. This table is also available in **ASCII format.**

Table T2. Expanded coring summary, Site 1185. (**See table notes.** Continued on next three pages.)

Core number	Date (Oct 2000)	Ship local time	Core depth (mbsf) Top	Core depth (mbsf) Bottom	Length (m) Cored	Length (m) Recovered	Recovery (%)	Section	Length (m) Liner	Length (m) Curated	Section depth (mbsf) Top	Section depth (mbsf) Bottom	Catwalk samples
192-1185A-													
1W	11	0745	0.0	250.6	0.0	NA	NA						
2R	11	0845	250.6	260.2	9.6	2.67	27.8						
								1	1.50	1.50	250.60	252.10	
								2	0.94	0.94	252.10	253.04	HS
								CC(w/2)	0.23	0.23	253.04	253.27	PAL
								Totals:	2.67	2.67			
3R	11	0955	260.2	269.8	9.6	2.06	21.5						
								1	1.50	1.50	260.20	261.70	
								2	0.38	0.38	261.70	262.08	HS
								CC(w/2)	0.18	0.18	262.08	262.26	PAL
								Totals:	2.06	2.06			
4R	11	1055	269.8	279.5	9.7	1.86	19.2						
								1	1.00	1.00	269.80	270.80	
								2	0.64	0.64	270.80	271.44	HS
								CC(w/2)	0.22	0.22	271.44	271.66	PAL
								Totals:	1.86	1.86			
5R	11	1150	279.5	289.1	9.6	1.83	19.1						
								1	1.10	1.10	279.50	280.60	
								2	0.59	0.59	280.60	281.19	HS
								CC(w/2)	0.14	0.14	281.19	281.33	PAL
								Totals:	1.83	1.83			
6R	11	1245	289.1	298.8	9.7	2.22	22.9						
								1	1.50	1.50	289.10	290.60	
								2	0.46	0.46	290.60	291.06	
								CC(w/2)	0.26	0.26	291.06	291.32	PAL
								Totals:	2.22	2.22			
7R	11	1345	298.8	308.4	9.6	3.04	31.7						
								1	1.50	1.50	298.80	300.30	
								2	1.04	1.04	300.30	301.34	HS
								CC(w/CC)	0.50	0.50	301.34	301.84	PAL
								Totals:	3.04	3.04			
8R	11	1715	308.4	317.0	8.6	2.36	27.4						
								1	0.44	1.50	308.40	309.90	PAL
								2	1.52	1.16	309.90	311.06	
								3	0.40	0.00			
								Totals:	2.36	2.66			
9R	11	2210	317.0	322.6	5.6	4.95	88.4						
								1	0.75	1.50	317.00	318.50	
								2	1.43	1.48	318.50	319.98	
								3	1.31	1.50	319.98	321.48	
								4	1.46	1.03	321.48	322.51	
								Totals:	4.95	5.51			
10R	12	0210	322.6	327.7	5.1	3.20	62.7						
								1	0.66	1.38	322.60	323.98	
								2	1.38	1.29	323.98	325.27	
								3	1.16	0.77	325.27	326.04	
								Totals:	3.20	3.44			
11R	12	0425	327.7	328.7	1.0	0.80	80.0						
								1	0.80	0.92	327.70	328.62	
								Totals:	0.80	0.92			
				Coring totals:	78.1	24.99	32.0						
192-1185B-													
1-0*	13	1205	0.0	30.5	0.0	0.00	NA						
1W	14	1905	30.5	308.0	0.0	0.00	0.0						
2R	14	2120	308.0	315.7	7.7	1.67	21.7						
								1	1.51	1.51	308.00	309.51	PAL
								2	0.16	0.19	309.51	309.70	
								CC(w/CC)	0.00	0.00			
								Totals:	1.67	1.7			
3R	14	2335	315.7	319.2	3.5	2.06	58.9						
								1	0.77	1.40	315.70	317.10	

Table T2 (continued).

Core number	Date (Oct 2000)	Ship local time	Core depth (mbsf) Top	Core depth (mbsf) Bottom	Length (m) Cored	Length (m) Recovered	Recovery (%)	Section	Length (m) Liner	Length (m) Curated	Section depth (mbsf) Top	Section depth (mbsf) Bottom	Catwalk samples
								2	1.29	1.06	317.10	318.16	
								Totals:	2.06	2.46			
4R	15	450	319.2	328.8	9.6	6.74	70.2						
								1	0.70	1.50	319.20	320.70	
								2	1.50	0.47	320.70	321.17	
								3	1.28	1.36	321.17	322.53	
								4	1.35	1.47	322.53	324.00	
								5	1.18	1.21	324.00	325.21	
								6	0.73	1.12	325.21	326.33	
								7	0.00	0.49	326.33	326.82	
								Totals:	6.74	7.62			
5R	15	1115	328.8	338.4	9.6	9.11	94.9						
								1	1.07	1.07	328.80	329.87	
								2	1.00	1.41	329.87	331.28	
								3	1.38	1.08	331.28	332.36	
								4	1.27	1.27	332.36	333.63	
								5	1.47	1.50	333.63	335.13	
								6	1.12	1.45	335.13	336.58	
								7	1.46	1.46	336.58	338.04	
								8	0.34	0.36	338.04	338.40	
								Totals:	9.11	9.60			
6R	15	1540	338.4	348.1	9.7	6.98	72.0						
								1	1.01	1.07	338.40	339.47	
								2	1.24	1.06	339.47	340.53	
								3	1.48	1.39	340.53	341.92	
								4	0.88	1.43	341.92	343.35	
								5	1.08	1.45	343.35	344.80	
								6	1.09	0.98	344.80	345.78	
								7	0.20	0.00			
								Totals:	6.98	7.38			
7R	15	1925	348.1	357.7	9.6	3.79	39.5						
								1	0.90	1.50	348.10	349.60	
								2	1.50	1.50	349.60	351.10	
								3	1.39	1.39	351.10	352.49	
								4	0.00	0.27	352.49	352.76	
								Totals:	3.79	4.66			
8R	16	55	357.7	367.3	9.6	2.06	21.5						
								1	1.46	1.50	357.70	359.20	
								2	0.60	0.94	359.20	360.14	
								Totals:	2.06	2.44			
9R	16	500	367.3	376.9	9.6	2.66	27.7						
								1	0.89	1.37	367.30	368.67	
								2	1.50	1.49	368.67	370.16	
								3	0.27	0.53	370.16	370.69	
								Totals:	2.66	3.39			
10R	16	1120	376.9	386.5	9.6	2.33	24.3						
								1	1.00	1.46	376.90	378.36	
								2	1.33	0.87	378.36	379.23	
								Totals:	2.33	2.33			
11R	16	1540	386.5	396.1	9.6	1.77	18.4						
								1	1.21	1.50	386.50	388.00	
								2	0.56	0.33	388.00	388.33	
								Totals:	1.77	1.83			
12R	16	2010	396.1	400.2	4.1	1.21	29.5						
								1	1.21	1.30	396.10	397.40	
								Totals:	1.21	1.30			
13R	16	2310	400.2	405.7	5.5	0.90	16.4						
								1	0.90	1.10	400.20	401.30	
								Totals:	0.90	1.10			
14R	17	415	405.7	415.3	9.6	4.09	42.6						
								1	0.35	1.50	405.70	407.20	
								2	1.34	1.50	407.20	408.70	
								3	1.20	1.27	408.70	409.97	
								4	1.20	0.00			
								Totals:	4.09	4.27			
15R	17	920	415.3	424.9	9.6	4.64	48.3						
								1	1.22	1.50	415.30	416.80	
								2	1.26	1.41	416.80	418.21	

Table T2 (continued).

Core number	Date (Oct 2000)	Ship local time	Core depth (mbsf) Top	Core depth (mbsf) Bottom	Length (m) Cored	Length (m) Recovered	Recovery (%)	Section	Length (m) Liner	Length (m) Curated	Section depth (mbsf) Top	Section depth (mbsf) Bottom	Catwalk samples
								3	1.00	1.40	418.21	419.61	
								4	1.16	0.00			
								Totals:	4.64	4.31			
16R	17	1425	424.9	434.6	9.7	1.67	17.2						
								1	0.61	1.42	424.90	426.32	
								2	1.06	0.17	426.32	426.49	
								Totals:	1.67	1.59			
17R	19	150	434.6	444.3	9.7	4.38	45.2						
								1	0.63	1.10	434.60	435.70	
								2	1.25	1.41	435.70	437.11	
								3	1.34	1.43	437.11	438.54	
								4	1.16	0.63	438.54	439.17	
								Totals:	4.38	4.57			
18R	19	700	444.3	449.1	4.8	1.69	35.2						
								1	0.58	1.50	444.30	445.80	
								2	1.11	0.32	445.80	446.12	
								Totals:	1.69	1.82			
19R	19	1140	449.1	453.9	4.8	5.11	106.5						
								1	1.46	1.45	449.10	450.55	
								2	1.01	1.45	450.55	452.00	
								3	1.40	1.04	452.00	453.04	
								4	1.24	1.09	453.04	454.13	
								Totals:	5.11	5.03			
20R	19	1840	453.9	463.6	9.7	4.43	45.7						
								1	0.57	1.25	453.90	455.15	
								2	1.44	1.28	455.15	456.43	
								3	1.23	0.86	456.43	457.29	
								4	1.19	1.25	457.29	458.54	
								Totals:	4.43	4.64			
21R	20	530	463.6	473.2	9.6	10.16	105.8						
								1	1.41	1.19	463.60	464.79	
								2	1.34	1.06	464.79	465.85	
								3	1.10	1.32	465.85	467.17	
								4	1.41	1.26	467.17	468.43	
								5	1.46	1.34	468.43	469.77	
								6	1.27	1.45	469.77	471.22	
								7	1.45	1.42	471.22	472.64	
								8	0.72	1.45	472.64	474.09	
								Totals:	10.16	10.49			
22R	20	1105	473.2	482.8	9.6	8.98	93.5						
								1	1.24	1.36	473.20	474.56	
								2	1.45	1.40	474.56	475.96	
								3	1.50	1.37	475.96	477.33	
								4	1.44	1.50	477.33	478.83	
								5	1.45	1.47	478.83	480.30	
								6	1.43	1.34	480.30	481.64	
								7	0.47	1.02	481.64	482.66	
								Totals:	8.98	9.46			
23R	20	1555	482.8	492.5	9.7	2.13	22.0						
								1	0.43	1.50	482.80	484.30	
								2	1.48	1.26	484.30	485.56	
								3	0.22	0.00			
								Totals:	2.13	2.76			
24R	20	2145	492.5	502.1	9.6	2.63	27.4						
								1	0.78	1.49	492.50	493.99	
								2	1.25	1.28	493.99	495.27	
								3	0.60	0.00			
								Totals:	2.63	2.77			
25R	21	520	502.1	511.8	9.7	0.00	0.0						
26R	21	805	511.8	516.6	4.8	0.00	0.0						
27R	21	1150	516.6	517.6	1.0	0.00	0.0						
28R	21	1450	517.6	518.6	1.0	0.98	98.0						
								1	0.98	1.04	517.60	518.64	
								Totals:	0.98	1.04			

Table T2 (continued).

Core number	Date (Oct 2000)	Ship local time	Core depth (mbsf) Top	Core depth (mbsf) Bottom	Length (m) Cored	Length (m) Recovered	Recovery (%)	Section	Length (m) Liner	Length (m) Curated	Section depth (mbsf) Top	Section depth (mbsf) Bottom	Catwalk samples
29R	21	1805	518.6	526.1	7.5	0.00	0.0						
				Coring totals:	218.1	92.17	42.3						

Notes: CC = core catcher, HS = headspace sample, PAL = paleontology. * = Core 1-0 in Hole 1185B is the interval for jet in of 16-in casing. This table is also available in **ASCII format.**

Table T3. Lithologic units with depth interval, distinguishing characteristics, and main sediment facies, Site 1185.

Core, section, interval (cm)	Depth interval (mbsf)	Unit	Distinguishing characteristic	Age	Main sediment facies	Other characteristics
192-1185A- 2R-1, 0, to 8R-1, 14	250.60-308.54	II	Chalk	upper Eocene	Nannofossil chalk with radiolarians to radiolarian nannofossil chalk	Planktonic foraminifers are very rare.
192-1185B- 2R-1, 0, to 2R-1, 151	308.00-309.51	II	Chalk	upper Eocene	Nannofossil chalk with radiolarians to radiolarian nannofossil chalk	Planktonic foraminifers are very rare.
192-1185A- 8R-1, 14, to 11R-1, 92	308.54-328.70	Basement	Basalt flows	Cretaceous	Basalt	Rare interlava limestone contains very poorly preserved foraminifers and nannofossils.
192-1185B- 2R-2, 0, to 28R-1, 104	309.51-526.10	Basement	Basalt flows	Cretaceous	Basalt	Rare interlava limestone contains very poorly preserved foraminifers and nannofossils.

Notes: Depth intervals are based on curated depths. Based on changes in drilling conditions, the top of basement in Hole 1185A was 312.0 mbsf (see "Operations," p. 2).

Table T4. Inorganic carbon, $CaCO_3$ contents, and mineral components in sediments in Unit II, Hole 1185A.

Core, section, interval (cm)	Depth (mbsf)	Lithology	Inorganic carbon (wt%)	$CaCO_3$ (wt%)	Mineral component (by XRD)
192-1185A-					
2R-2, 59-61	252.69	Radiolarian nannofossil chalk	10.85	90.42	Calcite
3R-1, 31-32	260.51	Radiolarian nannofossil chalk	10.35	86.18	Calcite
4R-1, 24-26	270.04	Radiolarian nannofossil chalk	10.25	85.42	Calcite
5R-1, 26-27	279.76	Radiolarian nannofossil chalk	10.49	87.39	Calcite
6R-1, 8-9	289.18	Radiolarian nannofossil chalk	10.51	87.53	Calcite
7R-1, 93-94	299.73	Radiolarian nannofossil chalk	10.16	84.61	Calcite

Note: XRD = X-ray diffraction.

Table T5. List of planktonic foraminifer and calcareous nannofossil highest and lowest occurrences in Unit I.

Core, section, interval (cm)	Event	Species	Zone/ Subzone	Depth (mbsf)	Age (Ma)	Stage/ Epoch
192-1185A-						
2R-1, 1		Highest sample		250.60		
2R-1, 1	HO	*C. consuetus*	NP19	250.60		
2R-CC	HO	*G. cerroazulensis*	P17	253.22	33.8	
3R-1, 30	HO	*S. radians*	NP19	260.50		
3R-CC	HO	*C. reticulatus*	NP19	262.21	35.0	upper Eocene
3R-CC	LO	*G. ampliapertura*	P16	262.21		
3R-CC	LO	*G. euapertura*	P16	262.21		
4R-1, 25	HO	*S. intercalaris*	NP18	270.05		
5R-1, 26	HO	*H. lophota*	NP18	279.76		
5R-CC	LO	*T. increbescens*	P16	281.28		
5R-CC	LO	*G. angiporoides*	P16	281.28		
6R-1, 108	HO	*C. grandis*	NP17	290.18	37.1	
6R-2, 6	LO	*S. intercalaris*	NP17	290.66		
6R-CC	HO	*G. senni*		291.27		
7R-1, 91	HO	*S. obtusus*		299.71		
7R-CC	HO	*H.* cf. *bolivariana*		301.82		middle Eocene
7R-CC	LO	*D. bisectus*	NP17	301.82	38.0	
8R-1, 3	LO	*G. index*	P12	308.43	42.9	
8R-1, 8	HO	*C. solitus*	NP16	308.48	40.4	
8R-1, 10	LO	*C. reticulatus*	NP16	308.50	42.0	
8R-1, 10		Lowest sample above basement		308.50		
9R-4, 97	HO	*R. asper*		322.45	93.2	Albian-Cenomanian
10R-1, 49	HO	*M. chiastius*		323.09	93.5	
10R-1, 49	LO	*T. exiguus*		323.09	early Albian	
192-1185B-						
2R-1, 40		Highest sample		308.40		
2R-1, 40	HO	*C. solitus*	NP16	308.40	40.4	middle Eocene
2R-1, 146	HO	*G. micra*		309.46		
2R-1, 149	LO	*C. reticulatus*	NP16	309.49	42.0	
2R-1, 149		Lowest sample above basement		309.49		
4R-2, 42	HO	*R. asper*		321.12	93.2	Albian-Cenomanian
4R-2, 42	HO	*M. chiastius*		321.12	93.5	
4R-3, 58	LO	*P. columnata*		322.78	112.3	Aptian

Notes: shaded = planktonic foraminifer, unshaded = calcareous nannofossil. HO = highest occurrence, LO = lowest occurrence. Ages are from Berggren et al. (1995). This table is also available in **ASCII format.**

Table T6. Range chart showing middle to upper Eocene turnover in abyssal benthic foraminifer assemblages.

Core, section, interval (cm)	Depth (mbsf)	*Aragonia aragonensis*	*Quadrimorphina profunda*	*Nuttallides truempyi*	*Abyssamina quadrata*	*Vulvulina spinosa*	*Cibicidoides micrus*	*Alabamina dissonata*	*Abyssamina poagi*	*Clinapertina complanata*	*Gaudryina pyramidata*	*Cibicidoides* sp. 13	*Stilostomella aculeata*	*Cibicidoides eocaenus*	*Oridorsalis umbonatus*	*Cibicidoides grimsdalei*	*Globocassidulina subglobosa*	*Gyroidinoides altiformis*	*Cibicidoides praemundulus*	*Gyroidinoides soldanii*	*Cibicidoides mexicanus*	Comments	
192-1185A-																							
2R-CC, 18	253.22			F									T		R	C	R		R	T	T		
3R-CC, 13	262.21			F		R							F		F	C	T	R	F	T		late Eocene fauna	
4R-CC, 17	271.61			F				C					R		R	F	R	R	F				
5R-CC, 9	281.28			F	R		R	A					T	T		F	R	R	R	T		Transition zone	
6R-1, 51	289.61			C				F				R				F	T	T	R				late Eocene
6R-1, 106	290.16			A				T		T		R	R			T	R	T					middle Eocene
6R-2, 4	290.64			A				F		R			T			R	R	R				*N. truempyi* fauna	
6R-CC, 21	291.27			A	T	R	R	F		F	T		F	T	C	A	F	T	R				
7R-CC, 48	301.82			A	R	T	F	C	T	R			R		C	A	R	R					
8R-1, 1	308.41	T	T	R				R									R						

Notes: A = abundant, C = common, F = few, T = trace, R = rare. Dark shading = species of the *Nuttalides truempyi* fauna; light shading = species of the late Eocene fauna defined by Tjalsma and Lohmann (1983). This table is also available in **ASCII format.**

Table T7. Unit thicknesses and general characteristics and criteria for defining unit boundaries, Site 1185.

Unit/ Subunit	Thickness (m)	Characteristics	Unit top defined by
192-1185A:			
1	9.91	Massive with pillowed top and base	Not recovered
2	3.97	Pillowed	Recrystallized limestone containing altered glass clasts (6-cm piece)
3A, 3B	0.19 + 0.16	Pillowed	Limestone containing fresh glass (9-cm piece: Subunit 3A)
4A, 4B	0.04 + 0.15	Pillowed	Limestone next to altered glass (4-cm piece: Subunit 4A)
5A, 5B	0.18 + >5.50	Pillowed	Limestone and glass (18-cm interval: Subunit 5A)
192-1185B:			
1	11.19	Pillowed	Not recovered
2	15.56	Massive with a minor pillowed top; carbonate-filled fractures present	Interval dominated by hyaloclastite (47 cm)
3	1.00	Pillowed	Downward change from massive unit to pillows with hyaloclastite
4	1.23	Pillowed	Hyaloclastite (9-cm piece)
5	9.61	Massive with pillowed top	Interval dominated by basaltic breccia with glass clasts in a pink clay and white carbonate matrix (70 cm)
6	1.20	Pillowed	Interval dominated by hyaloclastite (65 cm)
7	19.00	Pillowed; glassy rims and minor carbonate sediment present	Interval of carbonate-cemented breccia with glass clasts (20 cm)
8	1.14	Pillowed	Interval of carbonate-cemented basaltic breccia and hyaloclastite (15 cm)
9	65.16	Pillowed	Interval of carbonate-cemented hyaloclastite (15 cm)
10	19.30	Massive; carbonate-filled fractures	Altered, coarse-grained yellow-brown basaltic breccia (22 cm)
11	28.10	Massive	Presence of vesicles and greenish alteration combined with an abrupt increase in drilling rate for 4 m with no recovery
12	>36.64*	Massive	Chilled upper contact

Note: * = final core was not recovered because bottom-hole assembly broke (see "Operations," p. 2).

Table T8. Shipboard ICP-AES analyses and normative compositions of basalt samples, Site 1185.

	192-1185A-			192-1185B-												
Core, section:	8R-1	9R-2	10R-3	3R-1	4R-7	5R-2	6R-4	8R-2	11R-2	14R-3	17R-3	18R-2	20R-3	22R-6	22R-7	28R-1
Piece:	2	1	1B	16	1C	1D	2	8	5	6	1A	3	3B	6A	2	3B
Interval (cm):	15-18	14-15	51-54	94-97	44-46	135-137	74-76	73-76	28-32	38-41	1-3	17-20	66-68	51-54	42-43	80-82
Unit/Subunit:	1	2	5B	1	2	3	5	7	9	9	10	10	11	11	12	12
Depth (mbsf):	308.55	318.64	325.78	316.64	326.77	331.22	342.66	359.93	388.28	409.07	437.12	445.97	457.09	480.81	482.06	518.40
Major element (wt%):																
SiO_2	49.25	48.80	49.09	49.19	49.75	49.34	49.64	49.18	48.42	48.59	50.74	49.35	50.51	50.73	50.20	50.63
TiO_2	0.73	0.74	0.75	0.72	0.77	0.74	0.72	0.73	0.76	0.75	1.06	1.07	1.07	1.04	1.03	1.03
Al_2O_3	15.39	15.42	15.78	15.20	15.93	15.21	15.34	15.53	16.03	156.04	14.18	14.41	14.16	14.13	14.11	14.16
Fe_2O_3T	10.98	10.99	10.01	10.91	9.26	10.61	10.44	10.73	11.32	10.80	11.50	12.40	11.87	12.39	11.97	12.40
MnO	0.18	0.18	0.18	0.18	0.16	0.17	0.18	0.19	0.20	0.22	0.21	0.22	0.19	0.20	0.20	0.22
MgO	9.30	8.04	8.97	9.63	9.00	9.25	9.53	8.45	6.99	7.43	8.33	8.33	7.42	8.00	6.74	7.61
CaO	12.39	12.60	12.53	12.21	12.72	12.40	11.92	12.55	13.67	13.15	11.81	12.19	11.89	11.50	11.39	11.89
Na_2O	1.51	1.78	1.75	1.43	1.85	1.71	1.69	1.86	1.85	1.87	2.09	2.06	2.11	2.08	2.05	2.04
K_2O	0.18	0.28	0.08	0.12	0.09	0.07	0.03	0.23	0.71	0.16	0.08	0.07	0.06	0.07	1.00	0.08
P_2O_5	0.08	0.08	0.08	0.08	0.08	0.08	0.08	0.05	0.06	0.06	0.11	0.11	0.11	0.11	0.09	0.09
Total:	100.00	98.91	99.23	99.68	99.61	99.58	99.57	99.51	100.01	100.14	100.12	100.21	99.40	100.24	98.78	100.14
Mg#	0.66	0.62	0.67	0.67	0.69	0.66	0.67	0.64	0.58	0.61	0.62	0.60	0.58	0.59	0.56	0.58
LOI	–0.19	0.79	0.59	–0.28	1.22	0.69	1.31	2.54	2.46	2.26	0.59	0.48	0.19	0.79	0.59	0.48
CIPW norms:																
Q	0.0	0.0	0.0	0.0	0.0	0.0	0.0	0.0	0.0	0.0	0.6	0.0	1.4	1.0	0.0	1.1
Or	1.1	1.7	0.5	0.7	0.5	0.4	0.2	1.4	4.2	0.9	0.5	0.4	0.4	0.4	6.0	0.5
Ab	12.9	15.4	15.1	12.3	15.8	14.6	14.5	16.0	15.8	16.0	17.8	17.6	18.2	17.8	17.8	17.4
An	35.0	34.0	35.5	35.1	35.3	34.1	34.6	33.8	33.7	35.2	29.3	30.1	29.4	29.2	26.9	29.5
Di	21.6	23.9	22.0	20.8	22.6	22.5	20.1	23.6	28.2	24.7	23.7	24.7	24.4	22.6	24.9	24.1
Hy	22.7	17.2	19.6	25.4	19.4	21.5	25.4	16.4	3.8	17.3	23.6	17.8	21.6	24.5	19.5	22.8
Ol	3.1	4.2	3.8	2.0	2.9	3.3	1.7	5.3	10.6	2.3	0.0	4.8	0.0	0.0	0.4	0.0
Il	1.4	1.4	1.5	1.4	1.5	1.4	1.4	1.4	1.5	1.4	2.0	2.0	2.1	2.0	2.0	2.0
Mt	1.9	2.0	1.8	1.9	1.6	1.9	1.8	1.9	2.0	1.9	2.0	2.2	2.1	2.2	2.1	2.2
Ap	0.2	0.2	0.2	0.2	0.2	0.2	0.2	0.1	0.1	0.1	0.2	0.2	0.0	0.0	0.0	0.0
Trace element (ppm):																
Ni	181	168	160	186	192	200	230	168	176	198	108	102	104	107	84	102
Cr	457	456	418	453	448	443	511	463	487	485	190	182	177	190	183	194
V	251	242	250	238	264	242	244	254	265	258	330	318	310	311	306	312
Zr	39	36	42	39	40	41	36	41	42	43	58	57	61	56	57	56
Sc	44	43	43	43	47	43	42	43	45	44	48	49	48	48	47	48
Y	17	17	18	18	16	17	16	18	17	17	23	25	23	22	20	22
Sr	82	85	84	80	89	81	80	83	95	84	106	108	109	105	105	105
Ba	14	8	10	13	10	7	8	5	17	4	15	10	16	15	15	15

Notes: Fe_2O_3T = total Fe expressed as Fe_2O_3. Mg# and CIPW norms were calculated assuming $Fe_2O_3/(Fe_2O_3+FeO) = 0.13$, or $Fe_2O_3/FeO = 0.15$. LOI = weight loss on ignition at 1100°C; all analyses were conducted on ignited samples. This table is also available in **ASCII format.**

Table T9. Characteristic remanent magnetization direction, natural remanent magnetization intensity, median destructive field, magnetic susceptibility, and Koenigsberger ratio for selected basalt pieces, Site 1185. (See table notes. Continued on next two pages.)

Core, section, piece	Depth (mbsf)	Basement unit/subunit	Paleomagnetic unit	Dec (°)	Inc (°)	NRM (A/m)	MDF (mT)	κ (10^{-3} SI)	Q-ratio
192-1185A-									
8R-1(Piece 7)	309.06	1	A1	63.0	–28.2	1.97	17	4.46	14.7
8R-2 (Piece 3)	310.24	1	A1	213.4	–31.5	9.55	25	8.30	38.4
8R-2 (Piece 4)	310.52	1	A1	352.6	–34.3	5.07	26	11.71	14.4
8R-2 (Piece 4)	310.79	1	A1	357.7	–36.5	4.50	26	10.18	14.7
8R-2 (Piece 4)	310.93	1	A1	357.3	–34.5	4.26	26	9.78	14.5
9R-1 (Piece 1)	317.15	1	A1	345.2	–33.1	4.19	10	18.85	7.4
9R-1 (Piece 6)	317.89	1	A1	354.2	–29.1	3.66	13	7.90	15.4
9R-1 (Piece 7)	318.03	1	A1	189.3	–35.7	2.90	19	8.84	10.9
9R-2 (Piece 1)	318.56	2	A2	245.1	–39.4	1.19	35	4.15	9.6
9R-2 (Piece 2)	318.77	2	A2	253.5	–35.9	5.17	18	7.61	22.7
9R-2 (Piece 3)	319.03	2	A2	49.3	–34.1	4.88	19	8.35	19.5
9R-2 (Piece 3)	319.23	2	A2	48.6	–37.2	1.15	20	7.37	5.2
9R-2 (Piece 6)	319.59	2	A3	252.4	–44.5	1.51	35	3.08	16.4
9R-3 (Piece 5)	320.58	2	A3	113.5	–47.6	1.24	22	7.44	5.6
9R-3 (Piece 8)	321.25	2	A3	188.0	–41.9	2.32	21		
10R-1 (Piece 8)	323.20	5B	A4	5.5	–33.9	1.62	30	3.50	15.4
10R-1 (Piece 9)	323.42	5B	A4	74.5	–43.1	2.73	16	9.13	10.0
10R-1 (Piece 9)	323.65	5B	A4	70.4	–44.0	3.24	17	8.85	12.2
10R-2 (Piece1)	324.09	5B	A4	218.0	–44.6	1.63	24	5.31	10.2
10R-2 (Piece 2)	324.32	5B	A4	175.5	–44.8	1.51	24	5.86	8.6
11R-1 (Piece 4)	328.22	5B	A4	161.6	–38.7	1.91	11	22.34	2.9
11R-1 (Piece 4)	328.46	5B	A4	158.7	–37.6	2.40	12	24.77	3.2
192-1185B-									
3R-2 (Piece 1)	317.22	1	B1	308.4	–27.7	2.94	18	5.80	16.8
3R-2 (Piece 5)	317.50	1	B1	153.5	–37.5	1.35	18	4.20	10.7
3R-2 (Piece 7)	317.82	1	B1	349.2	–29.4	2.14	15	4.30	16.6
4R-3 (Piece 1)	321.26	2	B1	264.6	–32.7	2.46	15	7.70	10.7
4R-3 (Piece 1)	321.48	2	B1	264.4	–36.4	2.66	15	8.70	10.2
4R-3 (Piece 1)	321.81	2	B1	267.3	–36.6	2.58	12	9.00	9.5
4R-3 (Piece 1)	322.14	2	B1	335.9	–40.0	2.15	11	7.40	9.7
4R-3 (Piece 2)	322.42	2	B1	209.8	–38.4	1.68	15	6.90	8.2
4R-4 (Piece 1)	322.73	2	B1	66.4	–46.1	3.37	13	9.30	12.1
4R-4 (Piece 2)	323.21	2	B1	15.1	–36.2	7.49	14	9.60	26.1
4R-4 (Piece 2)	323.81	2	B1	176.5	–36.1	2.03	10	15.30	4.4
4R-5 (Piece 1)	324.13	2	B1	337.1	–31.7	1.32	6	7.50	5.8
4R-5 (Piece 2)	324.34	2	B1	114.2	–32.1	3.70	17	6.30	19.5
4R-5 (Piece 9)	325.14	2	B1	96.1	–35.8	2.10	9	7.70	9.1
4R-6 (Piece 1)	325.35	2	B2	136.1	–50.4	1.31	10	10.30	4.3
4R-6 (Piece 1)	325.66	2	B2	143.3	–44.5	1.65	15	13.20	4.2
4R-6 (Piece 1)	325.95	2	B2	154.3	–43.3	8.13	11	14.10	19.2
4R-6 (Piece 1)	326.19	2	B3	147.4	–44.5	2.86	18	14.90	6.4
4R-7 (Piece 1)	326.48	2	B3	220.1	–34.1	1.70	9	15.60	3.6
5R-1 (Piece 2)	329.06	2	B3	153.1	–30.3	3.11	17	16.40	6.3
5R-1 (Piece 2)	329.30	2	B3	147.7	–35.1	6.72	10	18.00	12.4
5R-1 (Piece 2)	329.72	2	B3	134.2	–35.5	2.90	10	13.70	7.1
5R-2 (Piece 1)	330.04	2	B3	137.6	–36.6	5.26	12	13.80	12.7
5R-2 (Piece 1)	330.21	2	B3	138.4	–36.8	4.54	12	12.70	11.9
5R-2 (Piece 1)	330.47	2	B3	132.9	–42.2	3.79	11	18.90	6.7
5R-2 (Piece 1)	330.80	2	B3	132.6	–38.2	3.06	9	23.50	4.3
5R-2 (Piece 1)	331.05	2	B3	124.8	–37.0	2.41	9	16.50	4.9
5R-3 (Piece 1)	331.42	2	B3	131.4	–35.6	2.07	9	13.50	5.1
5R-3 (Piece 1)	331.82	2	B3	140.5	–33.0	1.57	12	23.00	2.3
5R-3 (Piece 2)	332.13	2	B3	233.3	–36.1	2.63	14	16.90	5.2
5R-4 (Piece 1)	332.55	2	B3	242.7	–39.7	1.18	8	13.90	2.8
5R-4 (Piece 1)	332.79	2	B3	245.7	–37.5	1.60	6	17.10	3.1
5R-4 (Piece 1)	333.13	2	B3	239.8	–43.7	1.50	6	18.30	2.7
5R-4 (Piece 1)	333.25	2	B3	242.1	–42.8	1.48	7	12.90	3.8
5R-5 (Piece 1)	333.84	2	B3	237.1	–34.5	0.62	11	14.40	1.4
5R-5 (Piece 2)	334.31	2	B3	202.7	–35.3	1.71	8	27.70	2.1
5R-5 (Piece 2)	334.52	2	B3	197.0	–31.2	4.87	12	19.30	8.4
5R-5 (Piece 2)	334.88	2	B3	195.1	–32.5	2.45	9	28.50	2.9
5R-6 (Piece 1)	335.45	2	B3	155.0	–37.4	2.37	11	24.00	3.3
5R-6 (Piece 1)	335.77	2	B3	162.3	–37.8	1.53	8	14.70	3.5
5R-6 (Piece 1)	336.09	2	B3	160.6	–32.0	1.91	11	24.80	2.6

Table T9 (continued).

Core, section, piece	Depth (mbsf)	Basement unit/subunit	Paleomagnetic unit	Dec (°)	Inc (°)	NRM (A/m)	MDF (mT)	κ (10^{-3} SI)	Q-ratio
5R-7 (Piece 4)	337.09	3	B4	286.1	–39.4	3.29	18	7.00	15.6
5R-7 (Piece 7)	337.46	4	B4	272.6	–38.4	4.43	13	8.00	18.4
5R-7 (Piece 8)	337.65	4	B4	58.3	–41.8	3.85	15	8.00	16.0
5R-7 (Piece 11)	337.98	4	B4	41.4	–36.6	2.74	16		
6R-2 (Piece 1)	339.64	5	B5	98.7	–37.7	2.57	12	19.00	4.5
6R-2 (Piece 1)	339.95	5	B5	105.1	–32.5	1.67	11	29.30	1.9
6R-3 (Piece 4)	341.67	5	B5	228.4	–32.3	0.80	7	34.30	0.8
6R-4 (Piece 1)	342.05	5	B5	224.1	–35.6	1.67	5	27.90	2.0
6R-5 (Piece 1)	343.51	5	B5	175.6	–33.6	1.63	8	28.50	1.9
6R-5 (Piece 1)	343.71	5	B5	173.1	–34.4	1.67	9	28.20	2.0
6R-5 (Piece 1)	343.95	5	B5	174.6	–37.5	1.41	9	29.30	1.6
6R-5 (Piece 1)	344.19	5	B5	172.6	–39.6	1.82	9	29.10	2.1
6R-5 (Piece 2)	344.60	5	B5	158.4	–36.3	0.44	8	29.50	0.5
6R-6 (Piece 2)	344.98	5	B5	306.9	–32.0	0.85	7	31.30	0.9
6R-6 (Piece 2)	345.21	5	B5	303.4	–32.9	0.88	9	32.40	0.9
6R-6 (Piece 2)	345.45	5	B5	303.6	–30.5	0.95	10	32.40	1.0
7R-2 (Piece 6)	349.95	7	B6	130.5	–10.0	3.59	19	7.10	16.8
7R-4 (Piece 1)	352.65	7	B7	310.8	–37.1	4.61	19	7.90	19.4
8R-1 (Piece 3)	358.06	7	B7	247.7	–42.6	4.47	18	8.10	18.3
8R-1 (Piece 13)	358.65	7	B7	132.6	–42.2	4.89	20	8.90	18.3
9R-1 (Piece 6)	367.69	7	B7	184.6	–40.4	5.94	18	7.00	28.3
9R-1 (Piece 15)	368.60	8	B8	36.9	–31.4	9.12	23	7.50	40.6
9R-3 (Piece 8)	370.48	9	B9	329.7	–42.1	2.13	18	5.90	12.1
12R-1 (Piece 4)	396.36	9	B10	6.9	–14.2	4.84	17	7.00	23.1
12R-1 (Piece 6)	396.53	9	B10	65.8	–13.1	4.63	18	6.70	23.0
12R-1 (Piece 9)	396.94	9	B10	226.1	–23.1	3.82	22	6.70	19.0
14R-1 (Piece 2)	405.87	9	B11	156.3	–41.0	4.48	17	7.00	21.4
14R-1 (Piece 3)	406.13	9	B11	30.4	–39.2	3.74	17	7.20	17.3
14R-1 (Piece 3)	406.37	9	B11	37.7	–36.0	3.92	18	6.90	18.9
14R-1 (Piece 4)	406.63	9	B11	303.3	–28.8	3.93	18	7.10	18.4
14R-1 (Piece 4)	406.77	9	B11	298.5	–33.5	2.96	18	6.80	14.5
14R-1 (Piece 6)	407.01	9	B11	7.7	–36.9	3.53	17	6.00	19.7
14R-2 (Piece 2)	407.44	9	B11	0.1	–30.8	5.29	16	7.80	22.8
14R-2 (Piece 3)	407.62	9	B11	32.4	–34.9	4.66	17	7.30	21.3
14R-2 (Piece 4)	407.84	9	B11	349.6	–29.3	4.84	18	6.80	23.7
14R-3 (Piece 6)	409.12	9	B11	166.7	–29.4	4.54	18	8.20	18.5
15R-1 (Piece 3)	415.95	9	B12	21.9	–20.3	3.35	18	6.50	17.2
15R-1 (Piece 4)	416.28	9	B12	86.6	–19.9	3.70	18	6.90	17.8
15R-2 (Piece 2)	416.97	9	B13	43.8	–40.7	3.25	18	6.70	16.1
15R-2 (Piece 12)	418.10	9	B14	88.6	–28.7	5.60	17	7.00	26.7
15R-3 (Piece 1)	418.33	9	B14	76.9	–22.7	3.52	18	6.60	17.8
15R-3 (Piece 6)	418.71	9	B14	28.3	–36.3	3.47	15	8.60	13.4
16R-1 (Piece 7)	425.16	9	B14	8.7	–23.9	3.27	17	5.30	20.7
17R-1 (Piece 4)	435.13	10	B14	217.0	–36.9	5.88	15	8.80	22.3
17R-2 (Piece 1)	435.77	10	B14	212.9	–33.7	5.23	16	15.40	11.3
17R-2 (Piece 4)	436.56	10	B14	17.3	–32.9	10.10	26	18.00	18.7
17R-3 (Piece 1)	437.24	10	B15	326.8	–40.6	2.79	16	28.10	3.3
18R-1 (Piece 13)	445.62	10	B15	89.0	–39.6	3.21	20	21.10	5.1
19R-1 (Piece 1)	449.48	10	B15	221.9	–41.7	3.70	16	27.60	4.5
19R-1 (Piece 4)	450.16	10	B15	332.6	–41.0	1.51	13	28.50	1.8
19R-2 (Piece 1)	450.68	10	B15	191.0	–47.7	5.99	15	36.80	5.4
19R-2 (Piece 2)	450.95	10	B15	85.7	–47.9	1.18	14	35.40	1.1
19R-2 (Piece 2)	451.44	10	B15	87.0	–36.4	1.94	12	36.30	1.8
19R-3 (Piece 8)	452.95	10	B15	322.1	–32.6	3.11	4	26.50	3.9
20R-1 (Piece 12)	454.99	11	B16	14.9	–49.8	4.26	13	17.10	8.3
20R-2 (Piece 1)	455.35	11	B16	118.6	–50.1	3.98	11	25.40	5.2
20R-2 (Piece 1)	455.53	11	B16	109.5	–53.7	6.18	6	26.50	7.8
20R-3 (Piece 1)	456.64	11	B16	292.8	–41.6	7.91	9	20.80	12.7
20R-3 (Piece 3)	456.92	11	B16	182.2	–53.3	6.15	7	25.50	8.0
20R-4 (Piece 1)	457.44	11	B16	287.6	–43.6	2.47	11	23.80	3.5
20R-4 (Piece 1)	457.67	11	B16	292.4	–48.5	2.46	12	27.90	2.9
20R-4 (Piece 2)	458.14	11	B16	59.1	–44.5	3.75	14	20.00	6.3
21R-1 (Piece 11)	464.34	11	B16	101.3	–52.6	3.92	11	23.80	5.5
21R-1 (Piece 11)	464.63	11	B16	111.3	–53.0	2.49	13	25.40	3.3
21R-2 (Piece 1)	465.02	11	B16	245.6	–51.9	5.66	16	20.90	9.0
21R-2 (Piece 4)	465.49	11	B16	61.7	–46.3	6.50	6	25.40	8.5
21R-2 (Piece 5)	465.68	11	B16	157.0	–54.4	3.25	7	26.80	4.0
21R-3 (Piece 1)	466.28	11	B16	118.8	–52.8	5.67	4	27.30	6.9
21R-3 (Piece 2)	466.98	11	B16	166.9	–53.1	2.61	4	28.50	3.1

Table T9 (continued).

Core, section, piece	Depth (mbsf)	Basement unit/subunit	Paleomagnetic unit	Dec (°)	Inc (°)	NRM (A/m)	MDF (mT)	κ (10^{-3} SI)	Q-ratio
21R-3 (Piece 2)	467.11	11	B16	162.6	–45.7	3.61	10	31.30	3.8
21R-4 (Piece 1)	467.33	11	B16	133.8	–52.4	5.13	9	30.40	5.6
21R-4 (Piece 1)	467.62	11	B16	123.8	–51.2	3.09	6	29.20	3.5
21R-4 (Piece 1)	468.01	11	B16	111.6	–53.7	2.82	6	27.70	3.4
21R-5 (Piece 1)	468.71	11	B16	118.0	–55.0	3.69	4	21.50	5.7
21R-5 (Piece 1)	469.02	11	B16	140.5	–52.6	4.03	9	21.30	6.3
21R-5 (Piece 2)	469.41	11	B16	353.6	–47.6	7.78	6	22.30	11.7
21R-6 (Piece 1)	470.08	11	B16	349.8	–51.5	3.53	15	23.80	5.0
21R-6 (Piece 1)	470.52	11	B16	9.3	–50.4	5.90	5	24.80	7.9
21R-6 (Piece 2)	471.06	11	B16	333.1	–46.7	8.15	14	19.80	13.7
21R-7 (Piece 1)	471.32	11	B16	330.4	–47.9	4.63	12	23.70	6.5
21R-7 (Piece 2)	471.91	11	B16	337.7	–50.1	5.54	9	23.00	8.0
21R-7 (Piece 2)	472.39	11	B16	339.0	–48.8	6.96	14	28.10	8.3
21R-8 (Piece 1)	472.93	11	B16	334.8	–49.3	4.45	13	29.00	5.1
21R-8 (Piece 1)	473.28	11	B16	334.0	–44.6	4.20	15	29.70	4.7
21R-8 (Piece 2)	473.61	11	B16	337.5	–49.4	3.96	12	33.30	4.0
21R-8 (Piece 2)	473.79	11	B16	329.6	–49.4	4.56	5	32.00	4.7
22R-1 (Piece 2)	474.09	11	B16	229.7	–47.2	1.51	4	37.20	1.4
22R-2 (Piece 3)	475.35	11	B16	132.0	–45.2	1.83	4	34.80	1.8
22R-3 (Piece 2)	476.21	11	B16	320.1	–52.1	1.55	6	31.50	1.6
22R-3 (Piece 3)	476.53	11	B16	313.9	–50.9	4.28	11	25.70	5.6
22R-3 (Piece 3)	476.66	11	B16	314.1	–48.0	5.16	13	24.30	7.1
22R-4 (Piece 3)	478.16	11	B16	118.1	–43.2	1.98	10	35.50	1.9
22R-4 (Piece 3)	478.47	11	B16	129.4	–43.0	3.45	15	32.70	3.5
22R-6 (Piece 6)	480.98	11	B17	71.4	–28.3	3.10	7	34.30	3.0
22R-6 (Piece 7)	481.29	11	B17	327.4	–28.5	3.09	5	32.70	3.1
22R-6 (Piece 7)	481.47	11	B17	328.9	–32.1	2.16	6	29.30	2.5
23R-2 (Piece 4)	485.00	12	B17	264.9	–30.3	3.74	6	15.60	8.0
24R-2 (Piece 4)	494.33	12	B17	332.5	–33.4	2.19	12	13.50	5.4
28R-1 (Piece 3)	518.24	12	B18	109.3	–49.1	2.56	7	29.30	2.9

Notes: Dec = declination, Inc = inclination, NRM = natural remanent magnetization, MDF = median destructive field, κ = magnetic susceptibility, Q-ratio = Koenigsberger ratio. The basalt pieces are grouped into paleomagnetic units as described in "Paleomagnetism," p. 18. A present-day field of 30 A/m was used for Koenigsberger-ratio calculations. This table is also available in ASCII format.

Table T10. Paleomagnetic units A1–A4 and B1–B18.

Paleomagnetic unit	Depth (mbsf) Top	Depth (mbsf) Base	*N*	Inc (°)	k	α_{95}
192-1183A:						
A1	309.06	318.03	8	–32.9	404.6	2.8
A2	318.56	319.23	4	–36.7	888.8	3.1
A3	319.59	321.25	3	–44.7	607.5	5.0
A4	323.20	328.46	7	–41.1	204.8	4.2
192-1183B:						
B1	317.22	325.14	14	–35.6	168.0	3.1
B2	325.35	326.19	3	–46.1	352.8	6.6
B3	326.48	336.09	24	–36.7	240.3	1.9
B4	337.09	337.98	4	–39.1	938.0	3.0
B5	339.64	345.45	12	–34.6	471.7	2.0
B6	349.95	349.95	1	–10.0		
B7	352.65	367.69	4	–40.6	679.3	3.5
B8	368.60	368.60	1	–31.4		
B9	370.48	370.48	1	–42.1		
B10	396.36	396.94	3	–16.8	165.9	9.6
B11	405.87	409.12	10	–34.1	194.9	3.5
B12	415.95	416.28	2	–20.1		
B13	416.97	416.97	1	–40.7		
B14	418.10	436.56	7	–30.9	113.2	5.7
B15	437.24	452.95	8	–41.1	139.8	4.7
B16	454.99	478.47	39	–49.5	255.5	1.4
B17	480.98	494.33	5	–30.5	829.7	2.7
B18	518.24	518.24	1	–49.1		

Notes: Top = depth of the uppermost, Base = lowermost basalt piece within each unit. *N* = number of ChRM determinations in a given paleomagnetic unit. Inc = mean inclination calculated using Kono's (1980b) statistics. k = precision parameter. α_{95} = 95% confidence angle. For paleomagnetic units with <3 ChRM determinations, performing Kono statistics is impossible; therefore, only the mean inclination is listed for these units. This table is also available in **ASCII format.**

Table T11. Mean inclination and corresponding 95% confidence angle, precision parameter, angular standard deviation, and paleolatitude (with 95% confidence interval) for different groupings of paleomagnetic units.

Paleomagnetic units	*N*	Inc (°)	α_{95} (°)	k	ASD (°)	Paleolatitude (°)
All	22	–36.5	5.7	31.0	14.5	20.3 ± 3.2
A1-A4 and B1-B14	18	–34.9	6.2	32.6	14.2	19.2 ± 4.1
B15-B18	4	–43.2	13.0	50.7	11.4	25.2 ± 10.3

Notes: *N* = number of paleomagnetic units, Inc = mean inclination, α_{95} = 95% confidence angle, k = precision parameter, ASD = angular standard deviation. See **"Results from Basaltic Units,"** p. 20, for discussion.

Table T12. Index properties data, Site 1185.

Core, section, interval (cm)	Depth (mbsf)	Water content (%)		Density (g/cm^3)			Porosity (%)	Void ratio
		Bulk	Dry	Bulk	Dry	Grain		
192-1185A-								
2R-1, 77-79	251.38	38.772	63.324	1.537	0.941	2.250	58.183	1.391
2R-2, 59-61	252.70	37.845	60.889	1.557	0.968	2.279	57.538	1.355
3R-1, 62-64	260.83	37.279	59.437	1.647	1.033	2.580	59.960	1.498
3R-2, 19-21	261.90	35.079	54.034	1.688	1.096	2.598	57.827	1.371
4R-1, 25-27	270.06	41.741	71.647	1.509	0.879	2.284	61.507	1.598
5R-1, 24-26	279.75	38.413	62.373	1.548	0.953	2.274	58.076	1.385
6R-1, 8-10	289.19	39.355	64.894	1.543	0.936	2.298	59.293	1.457
7R-1, 132-134	300.13	41.099	69.777	1.469	0.865	2.108	58.953	1.436
7R-2, 2-4	300.33	39.360	64.908	1.497	0.908	2.137	57.532	1.355
10R-3, 39-41	325.67	4.714	4.947	2.557	2.437	2.762	11.772	0.133
192-1185B-								
2R-1, 43-45	308.43	25.846	34.854	1.867	1.384	2.618	47.118	0.891
4R-4, 111-113	323.64	2.869	2.954	2.708	2.630	2.846	7.586	0.082
5R-1, 26-28	329.06	4.229	4.416	2.649	2.537	2.849	10.941	0.123
5R-6, 24-26	335.37	3.212	3.318	2.666	2.581	2.816	8.363	0.091
5R-8, 3-5	338.07	6.351	6.782	2.536	2.375	2.818	15.727	0.187
6R-2, 43-45	339.90	4.095	4.270	2.644	2.536	2.836	10.574	0.118
6R-5, 133-135	344.68	4.216	4.402	2.729	2.614	2.944	11.236	0.127
7R-3, 16-18	351.26	4.816	5.060	2.438	2.320	2.621	11.466	0.130
8R-1, 96-98	358.66	3.931	4.092	2.543	2.443	2.708	9.764	0.108
10R-2, 27-29	378.63	4.847	5.094	2.595	2.469	2.815	12.281	0.140
12R-1, 66-68	396.76	3.562	3.694	2.484	2.395	2.622	8.640	0.095
14R-3, 54-56	409.24	4.866	5.114	2.576	2.450	2.792	12.239	0.139
15R-2, 62-63	417.42	2.858	2.942	2.561	2.488	2.679	7.149	0.077
16R-1, 40-42	425.30	5.575	5.904	2.519	2.379	2.757	13.715	0.159
17R-2, 84-86	436.54	1.510	1.533	2.854	2.811	2.935	4.210	0.044
18R-1, 12-14	444.42	2.336	2.392	2.747	2.682	2.862	6.266	0.067
19R-1, 37-39	449.47	3.666	3.805	2.725	2.625	2.908	9.753	0.108
19R-2, 112-114	451.67	2.406	2.466	2.748	2.682	2.867	6.457	0.069
20R-2, 23-25	455.38	2.960	3.050	2.707	2.627	2.849	7.823	0.085
21R-5, 109-111	469.52	1.617	1.644	2.789	2.744	2.870	4.404	0.046
21R-7, 36-38	471.58	1.377	1.396	2.736	2.698	2.801	3.679	0.038
22R-2, 83-85	475.39	2.474	2.536	2.698	2.631	2.815	6.518	0.070
23R-2, 89-91	485.19	1.722	1.752	2.729	2.682	2.811	4.589	0.048
24R-2, 79-81	494.78	3.387	3.506	2.803	2.708	2.985	9.272	0.102
28R-1, 18-20	517.78	3.126	3.227	2.830	2.742	3.001	8.641	0.095

Note: This table is also available in **ASCII format.**

Table T13. *P*-wave velocity measured using the contact probe system, Site 1185. (**See table notes**. Continued on next page.)

Core, section, interval (cm)	Depth (mbsf)	Direction	Velocity (m/s)	Anisotropy
192-1185A-				
2R-1, 77-79	251.38	Cx	1662.3	0.037
2R-1, 77-79	251.38	Cz	1601.0	
2R-1, 77-79	251.38	Cy	1647.0	
2R-2, 59-61	252.70	Cx	1641.4	0.037
2R-2, 59-61	252.70	Cz	1581.6	
2R-2, 59-61	252.70	Cy	1615.3	
7R-1, 131-133	300.12	Cx	1604.5	0.015
7R-1, 131-133	300.12	Cy	1588.2	
7R-1, 131-133	300.12	Cz	1580.4	
7R-2, 1-3	300.32	Cx	1609.1	0.018
7R-2, 1-3	300.32	Cy	1611.9	
7R-2, 1-3	300.32	Cz	1583.5	
8R-2, 89-91	310.80	_x	5506.2	
8R-2, 55-57	310.46	_x	5312.1	
9R-1, 54-56	317.55	_x	5140.8	
9R-2, 49-51	319.00	_x	5202.0	
9R-3, 69-71	320.68	_x	4796.4	
9R-4, 79-81	322.28	_x	4641.4	
10R-1, 85-87	323.46	_x	4750.1	
10R-3, 38-40	325.66	Mx	5612.1	
10R-3, 59-61	325.87	_x	4802.0	
11R-1, 44-46	328.15	_x	5455.8	
192-1185B-				
2R-1, 43-45	308.44	Cx	1841.4	0.070
2R-1, 43-45	308.44	Cz	1717.0	
2R-1, 43-45	308.44	Cy	1807.9	
3R-1, 79-81	316.50	_x	4189.1	
3R-2, 69-71	317.80	_x	4038.0	
4R-1, 79-81	320.00	_x	4208.4	
4R-2, 22-24	320.93	_x	5155.5	
4R-3, 49-51	321.67	_x	5263.5	
4R-4, 109-111	323.63	Mx	5193.2	
4R-4, 139-141	323.93	_x	5142.3	
4R-5, 49-51	324.50	_x	5059.6	
4R-6, 29-31	325.51	_x	5169.9	
4R-7, 39-41	326.73	_x	5008.0	
5R-1, 25-27	329.06	Mx	5230.6	
5R-1, 34-36	329.15	_x	5306.5	
5R-1, 99-101	329.80	_x	5513.6	
5R-2, 59-61	330.47	_x	5382.8	
5R-3, 49-51	331.78	_x	5378.6	
5R-4, 21-23	332.58	_x	5410.8	
5R-4, 39-41	332.76	_x	5426.3	
5R-5, 109-111	334.73	_x	5407.8	
5R-6, 23-25	335.37	Mx	5334.8	
5R-6, 39-41	335.53	_x	5429.4	
5R-7, 105-107	337.64	_x	4369.3	
5R-7, 120-122	337.79	_x	4178.7	
5R-7, 139-141	337.98	_x	4594.8	
5R-8, 2-4	338.07	Mx	4713.4	
5R-8, 7-9	338.12	_x	4419.7	
6R-2, 42-44	339.90	Mx	5691.0	
6R-2, 59-61	340.07	_x	5496.8	
6R-3, 89-91	341.43	_x	5065.3	
6R-4, 29-31	342.22	_x	5485.2	
6R-5, 107-109	344.43	_x	5476.6	
6R-5, 132-134	344.68	Mx	5477.3	
6R-6, 72-74	345.53	_x	5647.3	
7R-1, 94-96	349.05	_x	4663.5	
7R-2, 79-81	350.40	_x	4327.9	
7R-3, 16-18	351.27	Mx	4485.9	
7R-3, 17-19	351.28	_x	4498.8	
7R-4, 4-6	352.54	_x	4658.4	
8R-1, 35-37	358.06	_x	4859.1	
8R-1, 94-96	358.65	_x	4703.1	
8R-1, 96-98	358.67	Mx	4999.3	
8R-2, 4-6	359.25	_x	5126.4	
9R-1, 42-44	367.73	_x	4856.7	
9R-2, 114-116	369.82	_x	4735.5	
9R-3, 34-36	370.51	_x	5066.7	
10R-1, 87-89	377.78	_x	4788.9	
10R-2, 26-28	378.63	Cx	4720.8	
10R-2, 26-28	378.63	Cz	5110.6	
10R-2, 54-56	378.91	_x	5050.2	
11R-1, 14-16	386.65	_x	5309.5	
11R-1, 114-116	387.65	_x	4996.0	
12R-1, 39-41	396.50	_x	4815.6	
13R-1, 19-21	400.40	_x	4132.5	
13R-1, 79-81	401.00	_x	3718.8	
14R-1, 29-31	406.00	_x	3966.9	
14R-1, 109-111	406.80	_x	3949.6	
14R-2, 23-25	407.44	_x	4241.4	
14R-2, 109-111	408.30	_x	4555.2	
14R-3, 24-26	408.95	_x	4340.3	
15R-1, 77-79	416.08	_x	4336.9	
15R-2, 4-6	416.85	_x	4318.2	
15R-2, 90-92	417.71	_x	4958.7	
15R-3, 49-51	418.71	_x	4675.2	
16R-1, 34-36	425.25	_x	5175.9	
16R-1, 39-41	425.30	Mx	4968.7	
16R-1, 45-47	425.36	_x	5184.2	
17R-1, 47-49	435.08	_x	5322.2	
17R-2, 39-41	436.10	_x	5583.6	
17R-2, 84-86	436.55	Mx	4879.4	
17R-3, 9-11	437.21	_x	5465.2	
17R-3, 69-71	437.81	_x	5122.6	
17R-4, 13-15	438.68	_x	5190.6	
18R-1, 17-19	444.48	_x	5364.6	
18R-1, 97-99	445.28	_x	4636.5	
18R-2, 23-25	446.04	_x	5598.6	
19R-1, 32-34	449.43	_x	5689.5	
19R-2, 34-36	450.90	_x	5667.0	
19R-2, 111-113	451.67	Mx	5541.3	
19R-3, 29-31	452.30	_x	5243.5	
19R-1, 366-368	452.77	Mx	5699.9	
19R-4, 74-76	453.79	_x	5198.0	
20R-1, 109-111	455.00	_x	4693.4	
20R-2, 22-24	455.38	Mx	5601.8	
20R-2, 119-121	456.35	_x	5332.7	
20R-3, 63-65	457.07	_x	5295.9	
20R-4, 81-83	458.11	_x	5570.5	
21R-1, 79-81	464.40	_x	5425.0	
21R-1, 109-111	464.70	_x	5685.7	
21R-2, 59-61	465.39	_x	5253.1	
21R-2, 99-101	465.79	_x	5607.7	
21R-3, 37-39	466.23	_x	5712.1	
21R-3, 38-40	466.24	_x	5541.8	
21R-3, 99-101	466.85	_x	5725.6	
21R-4, 56-58	467.74	_x	5680.8	
21R-4, 89-91	468.07	_x	5619.6	
21R-5, 9-11	468.53	_x	5716.9	
21R-5, 108-110	469.52	Mx	5449.4	
21R-5, 109-111	469.53	_x	5661.7	
21R-6, 39-41	470.17	_x	5542.4	
21R-6, 139-141	471.17	_x	5487.9	
21R-7, 35-37	471.58	Mx	5790.1	
21R-7, 36-38	471.59	_x	5681.6	
22R-1, 19-21	473.40	_x	5416.0	
21R-8, 89-91	473.54	_x	5259.3	
21R-8, 119-121	473.84	_x	5307.9	
22R-2, 79-81	475.36	_x	5162.1	
22R-2, 82-84	475.39	Mx	5472.8	
22R-3, 14-16	476.11	_x	5174.9	
22R-4, 49-51	477.83	_x	5610.2	

Table T13 (continued).

Core, section, interval (cm)	Depth (mbsf)	Direction	Velocity (m/s)	Anisotropy
22R-5, 91-93	479.75	_x	5141.5	
22R-6, 88-90	481.19	_x	5071.9	
22R-7, 3-5	481.68	_x	5177.8	
23R-1, 59-61	483.40	_x	5151.0	
23R-2, 81-83	485.12	_x	4681.7	
23R-2, 89-91	485.20	Mx	5102.6	
24R-1, 33-35	492.84	_x	4873.3	
24R-2, 78-80	494.78	Cx	5314.5	
24R-2, 78-80	494.78	Cy	5527.9	
24R-2, 78-80	494.78	Cz	5271.6	
24R-2, 109-111	495.09	_x	4767.5	
28R-1, 17-19	517.78	Mx	5598.7	
28R-1, 77-79	518.38	_x	5420.1	

Notes: C = cut sample, _ = uncut split core, M = minicore, x = into the core, z = along the core, y = across the core face. This table is also available in **ASCII format.**

Table T14. Thermal conductivity values, Site 1185.

Core, section, interval (cm)	Depth (mbsf)	Thermal conductivity (W/[m·K])
192-1185A-		
2R-1, 30-32	250.90	1.314
6R-1, 90-92	290.00	1.332
7R-1, 140-142	300.20	1.302
7R-1, 141-143	300.21	1.308
8R-2, 90-92	310.80	1.797
9R-2, 50-52	319.00	1.711
10R-2, 75-77	324.73	1.604
11R-1, 45-47	328.15	1.790
192-1185B-		
3R-2, 69-71	317.80	1.424
3R-2, 99-101	318.10	1.452
4R-3, 49-51	321.67	1.736
4R-6, 29-31	325.51	1.708
5R-1, 26-28	329.07	1.750
5R-7, 137-139	337.96	1.638
6R-2, 34-36	339.82	1.936
6R-6, 74-76	345.55	1.959
7R-1, 89-91	349.00	1.580
8R-1, 29-31	358.00	1.644
9R-2, 114-116	369.82	1.708
10R-2, 7-9	378.44	1.735
11R-1, 102-104	387.53	1.883
12R-1, 39-41	396.50	1.760
13R-1, 19-21	400.40	1.369
14R-2, 109-111	408.30	1.592
15R-1, 64-66	415.95	1.871
15R-2, 64-66	417.45	1.641
16R-1, 114-116	426.05	1.824
17R-3, 9-11	437.23	1.778
17R-3, 39-41	437.51	1.785
18R-1, 129-131	445.60	1.728
19R-1, 139-141	450.51	1.849
20R-2, 70-72	455.86	1.790
21R-3, 99-101	466.85	1.807
21R-8, 66-68	473.31	1.841
22R-3, 59-61	476.56	1.883
22R-5, 94-96	479.78	1.860
23R-2, 89-91	485.20	1.770
24R-2, 110-112	495.10	1.725
28R-1, 29-31	517.91	1.841
28R-1, 52-54	518.13	1.856

Note: This table is also available in **ASCII format.**